N-body simulations of star forming regions

Rebecca Arnold

Submitted by Rebecca Arnold to the University of Sheffield as a thesis for the degree of Doctor of Philosophy in Physics, September, 2019.

This thesis is available for library use on the understanding that it is copyright material and that no quotation from the thesis may be published without proper acknowledgement.

I certify that all material in this thesis which is not my own work has been identified and that no material has previously been submitted and approved for the award of a degree by this or any other University.

Signed: .....

Rebecca Arnold

Date: .....

Abstract

This thesis contains a body of work using *N*-body simulations and numerical methods to study star forming regions.

It begins by introducing relevant topics, such as the basic picture of star formation, the environment(s) that stars form in, stellar dynamics, and statistical methods of analysing star forming regions. In the following chapter information is provided surrounding the computational methods used by the field to simulate star forming regions. *N*-body simulations are described in particular detail.

This alternative format thesis then includes the paper 'How do binary clusters form?' (Arnold et al. 2017) which details a study into the origins of binary clusters. Using *N*-body simulations it concludes that binary clusters may originate from single star forming regions which divide in two.

The next paper presented in this alternative format thesis is 'A method to analyse velocity structure' (Arnold & Goodwin 2019), which presents a statistical method for analysing the velocity structure of star forming regions (although the method also has wider capabilities).

The third paper presented is 'The velocity structure of Cygnus OB2' (Arnold et al. 2019; submitted) which applies the method presented in Arnold & Goodwin (2019) to observations of the Cygnus OB2 association. The results are used to investigate and interpret the region's dynamical history.

The fourth paper presented is 'Dynamical evolution of star-forming regions: III. Unbound stars and predictions for Gaia' (Schoettler et al. 2019), a study conducted in conjunction with C. Schoettler and a number of others. My contribution to this project is clearly outlined at the start of this chapter.

Contents

Declaration

I declare that, unless otherwise stated, the work presented in this thesis is my own. No part of this thesis has been accepted or is currently being submitted for any other qualification at the University of Sheffield or elsewhere.

Acknowledgements

Ok. This is the first bit of my thesis I'm writing because it's the easy bit, so I'm making the assumption future me succeeded in writing the rest. In a way that's optimistic because doing a PhD feels at times to be only slightly easier than beating Rafael Nadal at tennis with only a stick of celery to use for a racket. On the other hand it's a pretty sure bet I make it, because how could I fail with all the wonderful support from fantastic people that I've had so far and will doubtless sustain me the rest of the way. So, working from that assumption...

First and foremost I want to thank my supervisor, Simon Goodwin. Simon has, from day one, been helpful, welcoming, listened to me, and valued my input. Perhaps most importantly he made sure I knew that it was ok for me to ask 'dumb' questions and to make mistakes. I have no words for how much that safety net has helped me, both in terms of allowing me advance scientifically and in terms of my peace of mind. Simon, I never could have done this without you.

I want to thank all the PhDs, postdocs and academics that came and went during the course of my PhD, in particular Martin, Katie, Heloise, Richard, Emma and Christina. They, and everyone in the astrogroup really, are what's made this place a fun and uplifting environment to work in.

I also wouldn't have made it here without the unwavering support of my family, not just in the past few years but throughout my life.

Finally, most importantly of all, I want to thank Bibtex. Because if I had to format all these references by hand. I just. I just couldn't.

Chapter 1

Introduction

1.1 Motivation

Stars are one of the fundamental building blocks of the observable universe. They generate the bulk of the universe's light, synthesise its metals, and provide the necessary conditions for planet formation; planets are born in the dusty disks around forming/newly formed stars. As such, theories of planet formation depend strongly on the process of star formation. They are also impacted by the evolution of the regions stars form in, for example disks are photoevaporated by time spent in close proximity to massive stars, and also may be destroyed by supernovae. For these reasons, and many others, star formation and the evolution of star forming regions is of great scientific interest.

1.2 The basic picture of star formation

Stars form from large clouds of molecular gas, which are discussed in more detail in section 1.3.1. As an example the Taurus region's molecular cloud is shown in Fig. 1.1. These clouds contract under the force of their own self-gravity and/or due to compression by supersonic shocks. These mechanisms compete with turbulence as well as thermal and magnetic pressures within the cloud, which support it against collapse. At large size scales the pressure forces dominate, but at smaller scales pressure is overwhelmed by self-gravity. The transition between these two regimes occurs where the size scale equals a Jeans radius (Jeans 1902).

This can be derived for a cloud of point masses by solving for the length scale at which kinetic and potential energies are such that there is virial equilibrium. More details

regarding virial equilibrium can be found in section 1.2.1 but for now we simply state that in virial equilibrium:

$$KE = -\frac{PE}{2} \tag{1.1}$$

The kinetic energy of such a cloud is $\frac{3}{2}Nk_{\mathrm{B}}T$ **and the potential energy can be derived by integrating an energy element over the volume of the cloud.** dE **is the potential energy of a small mass** dM **on the edge of a sphere of mass** M**:**

$$dE = -\frac{GM(r)}{r}dM \tag{1.2}$$

$M(r)$ **is simply the volume of a sphere of radius** r **multiplied density of the gas** ρ_0**. Similarly** dM **is the volume element of a sphere multiplied by density. As such the potential energy of the cloud is:**

$$PE = -\frac{(4\pi)^2}{3}G\rho^2\int_0^R r^4 dr = -\frac{(4\pi\rho_0)^2}{3}\frac{R^5}{5} \tag{1.3}$$

By substituting in for the mass of a sphere of density ρ_0 **and radius** R **this can be expressed as**

$$PE = -\frac{3}{5}\frac{GM^2}{R} \tag{1.4}$$

By substituting the kinetic and potential energies into equation 1.1, using the fact the N **is equal to** M **divided by the mass per particle,** m**, and rearranging we find**

$$\frac{k_{\mathrm{B}}T}{m} = -\frac{GM}{5R}. \tag{1.5}$$

By eliminating M **as density times the volume of the sphere and substituting in** a_0**, the isothermal speed of sound, which is such that its square is equal to the left hand side of equation 1.5 we can solve for** R**, which is the Jeans radius:**

$$R_{\mathrm{J}} = a_0\sqrt{\frac{15}{4\pi G\rho_0}} \tag{1.6}$$

The mass within a spherical region of the cloud of this radius is referred to as a Jeans mass**, which**

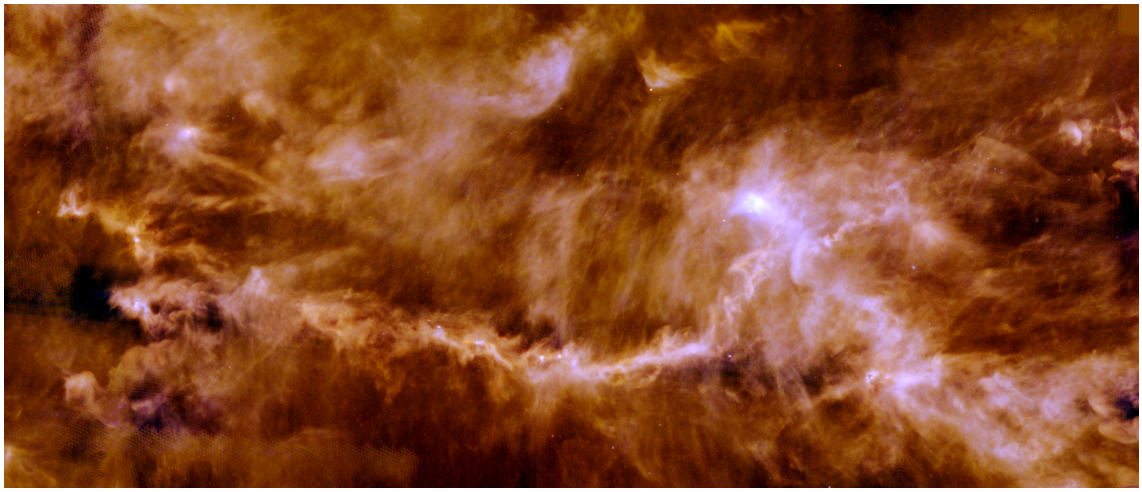

Figure 1.1: An image of the Taurus molecular cloud produced from data collected using *Herschel* to look at a wavelength of 250 μm. This data is presented in Palmeirim et al. (2013). It is clear from this image that the distribution of gas is highly non-homogeneous.

is simply the volume of a sphere with radius R_J multiplied by the gas density:

$$M_J = \frac{4\pi}{3} R_J^3 \rho_0. \tag{1.7}$$

By bringing some of the constants inside the square root and expressing 15 as 5×3 this can be rewritten as

$$M_J = a_0^3 \sqrt{\left(\frac{4\pi\rho_0}{3}\right)^2 \left(\frac{5 \times 3}{4\pi G \rho_0}\right)^3}. \tag{1.8}$$

Many of the terms can now be cancelled. The resulting constant in the numerator is 375, and the resulting equation is:

$$M_J = a_0^3 \sqrt{\frac{375}{4\pi G^3 \rho_0}}. \tag{1.9}$$

Dense condensations of gas called clumps with radii of around R_J (of order 1 pc) become unstable and begin to contract within the cloud. Note that as a clump within the cloud collapses the environment within that clump, e.g. pressure, changes too and the Jeans length is reduced. This can lead independent regions within the collapsing clump to self gravitate in turn, leading to contraction at multiple scales which is called fragmentation (Klessen et al. 1998).

The timescale that the cloud collapse occurs on is referred to as the free-fall timescale t_{ff}:

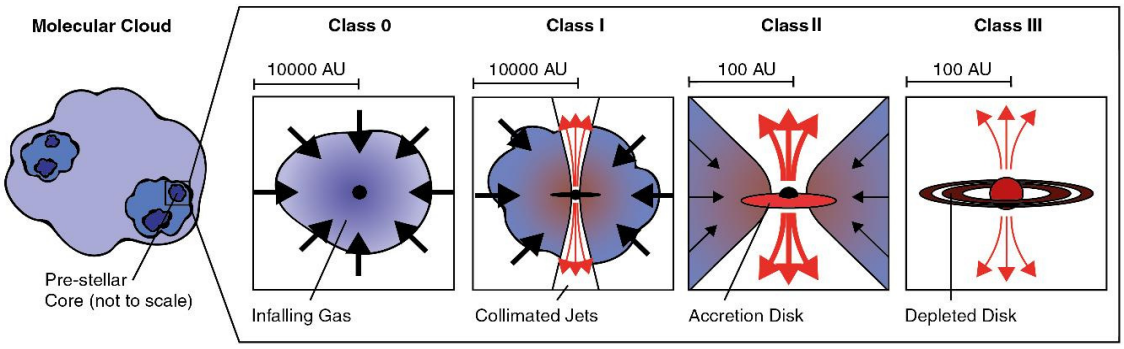

Figure 1.2: A diagram outlining the major steps and scales in star formation as described in section 1.2. This image is adapted from Griffiths (2018).

$$t_{\rm ff} = \sqrt{\frac{3\pi}{32G\rho}}. \tag{1.10}$$

Within these collapsing clumps particularly dense regions with masses around one $M_\odot$ form called cores. Similarly to clumps these are dense condensations of gas, the difference being that cores are typically gravitationally bound. Cores have temperatures of $\sim T = 10$ K (Andre et al. 2000), masses up to 10s of $M_\odot$, and sizes of order 10^5 AU (Ward-Thompson et al. 1999). Some are starless, but others are prestellar cores or protostellar cores also known as 'class 0' objects (André et al. 2009). These are the objects which evolve to become stars via a process presented in Larson (1969) which will be described in more detail here.

The stages of this evolution are divided into classes from 0 to III. The classification of young stellar objects (YSOs) into classes is done according to features of their spectral energy distribution (SED) and their bolometric temperature ($T_{\rm bol}$) (Lada & Wilking 1984; Greene et al. 1994; Chen et al. 1995; Enoch et al. 2009). Reviews on this topic can be found in Evans (1999), Lada & Lada (2003), McKee & Ostriker (2007), Kennicutt & Evans (2012) and Motte et al. (2018). A cartoon of this evolution is shown in Fig. 1.2, and a summary of the classes is provided here:

- Class 0: Prestellar core. This is a dense core with a disk embedded in a thick envelope. As such it is not yet a fully fledged star but a protostar. At this stage more material is in the envelope than in the protostar itself. The core is about $\sim 10^5$ years old.

- Class I: An accreting protostar with a disk. By this point (a few $\times 10^5$ years since the star began to form) more material is in the protostar than remains in the envelope. Note that the presence of a disk is recognised by **the shape of its SED**.

- Class II: Classical T Tauri star which is a pre main sequence (PMS) star with an age of a few 10^6 years. The YSO is no longer 'embedded' (surrounded by a large amount of dust and gas) so is much easier to observe from this point onward. It **also has** a disk.
- Class III: Weak line T Tauri which is also a kind of PMS star. These **objects have little of their disk remaining and** are around 10^7 years old. It is worth noting that PMS lifetimes are shorter for more massive stars.

Once stars have formed in a GMC **(Giant Molecular Cloud)** their feedback (especially from massive stars) causes the remainder of the gas they are embedded in to be pushed away. This process is referred to as gas expulsion and is discussed further in section 1.4. This leaves the stars that have formed exposed. As time passes the expelled molecular gas reforms/merges into a new GMC and the process repeats. A diagram of this process is shown in Fig. 1.3.

1.2.1 Key concepts

There are a number of key parameters and concepts of great importance to our understanding of star formation (in addition to those already outlined above such as free fall time and the **Jeans** mass). These will be mentioned in various places within this introduction, so we outline them here.

Perhaps the most important is the virial factor, which is the ratio **of the stars in a star forming region's kinetic energies to the potential energy of the region. According to the virial theorem s**tructures that are stable, i.e. neither expanding or collapsing have viral ratios of $\sim$ -0.5. If the virial factor is < -0.5 i.e. the region is 'subvirial' the system will likely undergo collapse. If it is > -0.5 the region is 'supervirial' and will most likely expand. Further if the virial factor is > 1 this means the region is unbound and its members will most likely disperse into the field.

The virial theorem can be derived by defining a variable I which is $\sum mr^2$ for the stars in a region. From this we can find

$$\frac{1}{2}\frac{d^2I}{dt^2} = \sum mv^2 + \sum mra \tag{1.11}$$

The first term on the right hand side is 2 times the kinetic energy of the system, and the second is the sum of the forces in the system multiplied by r, which is equal to the potential

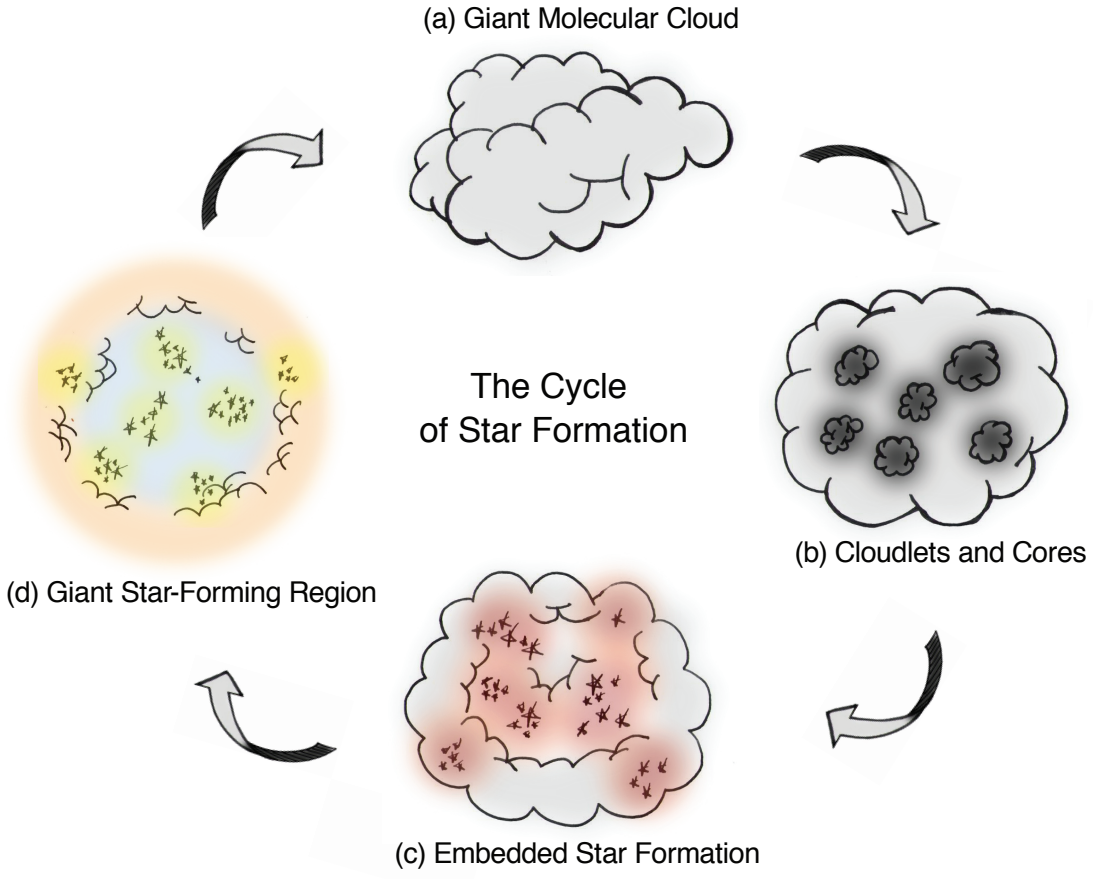

Figure 1.3: A diagram outlining the lifecycle of GMCs and how they relate to star formation. This image is taken from Gouliermis (2018). Part a) shows a GMC. In part b) gas condensations of $\sim$ Jeans length size form and develop cores. In part c) stars form from these cores and in part d) feedback mechanisms expel the remaining molecular gas they are embedded within. This expeled gas may form part of other GMCs in the future, and the cycle restarts.

energy of the system.

$$\frac{1}{2}\frac{d^2I}{dt^2} = 2KE + PE \tag{1.12}$$

If this equation is integrated over a long time T and divided by T the average of the right hand quantities are obtained:

$$\frac{1}{2T}\left[\frac{dI}{dt}\right]_0^T = \langle 2KE\rangle + \langle PE\rangle \tag{1.13}$$

Because T is long and for a bound system $\frac{dI}{dt}$ must be finite the left hand side must be 0, so for a bound system

$$\frac{-KE}{PE} = 0.5. \tag{1.14}$$

Also on the topic of stellar dynamics there are two important timescales to mention; the crossing time of a region ($t_{\rm cross}$), and its two body relaxation time ($t_{\rm relax}$). The crossing time is the approximate time it takes a star to cross from one side of a region that has radius R to the other. This is given by

$$t_{\rm cross} = \frac{2R}{\sigma} \tag{1.15}$$

where σ is the velocity dispersion of the region, i.e. the root mean square of its stellar velocities. The relaxation time is a little more involved. Stars in a star forming region exert gravitational forces on one another, changing their velocities. The two body relaxation time is the expected time for the magnitude of the changes to a star's velocity due to gravitational interactions with other stars to equal the magnitude of the star's initial velocity. The relaxation time is related to the crossing time such that

$$t_{\rm relax} = \frac{Nt_{\rm cross}}{10ln(N)} \tag{1.16}$$

where N is the number of stars in the region (Binney & Tremaine 1987).

1.3 The environment(s) stars form in

1.3.1 Giant molecular clouds

In this work the term 'association' is used to specifically describe distributed, unbound groups of stars, and the word 'cluster' is used to describe bound, centrally condensed groups of stars. The term 'star forming region' is used to describe both associations and clusters. Also note that associations may contain clusters.

Stars form in giant molecular clouds (GMCs) (Blitz 1993; Evans et al. 2009; Lada et al. 2010), which are clouds of mainly molecular hydrogen and helium. It is usually not possible to observe the hydrogen and helium, however molecular clouds also contain dust (Rosolowsky & Blitz 2005) and molecules such as CO (Heyer & Dame 2015), which are more easily detected and can be used to 'trace' the less easily observed hydrogen and helium gas content.

Molecular clouds have temperatures of around 10s of Kelvin and their masses span many orders of magnitude from 10^2 - $10^7 M_\odot$ (Brand & Wouterloot 1995; Heyer et al. 2001; Rosolowsky et al. 2008). **The mass spectrums of GMCs** approximately follow M^{-2}, however there is evidence **they** may vary with their environment (Engargiola et al. 2003; Colombo et al. 2014). It is difficult to accurately measure the sizes of GMCs due to the inherent limitations of 2D observations of 3D objects, and because they typically do not have clear boundaries. They typically range from 10^1 - 10^2 pc in radius (see Fig. 1.4 taken from Fukui & Kawamura (2010)).

The dynamics of GMCs are not simple (Zuckerman & Evans 1974); they are dominated by turbulent motion (Vázquez-Semadeni et al. 1997; Elmegreen & Scalo 2004; Scalo & Elmegreen 2004; McKee & Ostriker 2007; Ballesteros-Paredes et al. 2007; Hennebelle & Falgarone 2012). This turbulent motion can be **approximated** assuming the gas is an incompressible fluid, as outlined in Kolmogorov (1941) **which describes how kinetic energy can be transferred from large to small scales until the scales are small enough that it can be dissipated.** There have also been studies investigating turbulence in compressible fluids in order to better understand the dynamics of molecular clouds (Porter et al. 1992, 1994). Other models of turbulence, such as the pressure-less Burgers turbulence are also used (Burgers 1939; Bec & Khanin 2007). **It it worth noting that observationally this picture becomes considerably more complex (McKee & Ostriker 2007)**.

In a turbulent environment velocity dispersion in GMCs scales with their size (Larson 1981; Heyer & Brunt 2004), see Fig. 1.4. Given the sizes of GMCs these velocity dispersions are suffi-

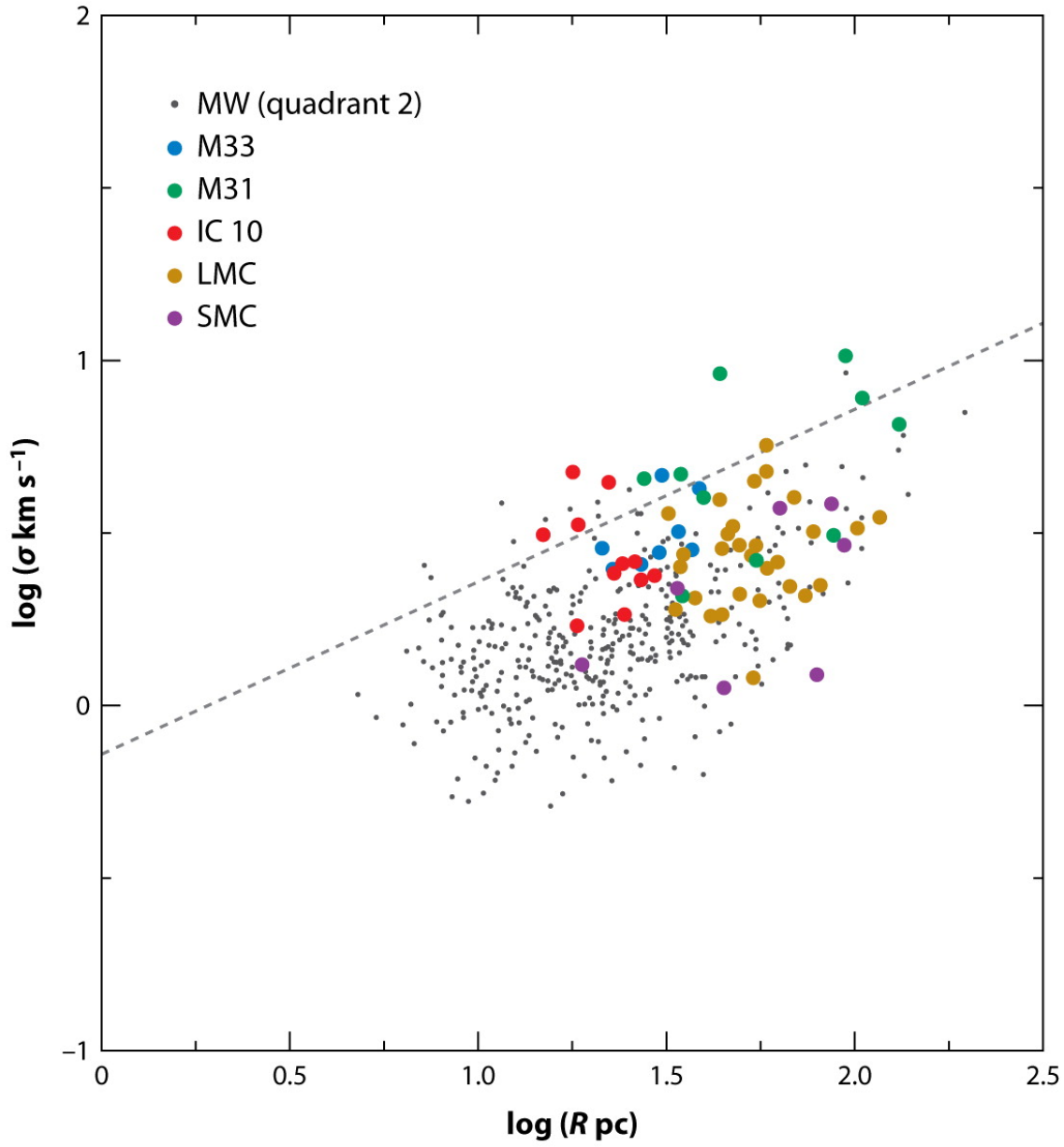

Figure 1.4: This figure is taken from Fukui & Kawamura (2010). It shows the log of the radii in parsecs of GMCs in a number of galaxies against their velocity dispersion. The data for this plot was assembled from a number of other papers, Solomon et al. (1987), Dame et al. (2001), Mizuno et al. (2001), Rosolowsky et al. (2001), Engargiola et al. (2003), Leroy et al. (2006), and Fukui et al. (2008). **The grey dashed line shows this same relation for GMCs found in the inner Milky Way (Solomon et al. 1987)**.

ciently large that motions are often supersonic, resulting in shocks (Crutcher 1999; Padoan et al. 1999, 2004). Filamentary structure is also found within these clouds both observationally (Bally et al. 1987; Nutter et al. 2008; Arzoumanian et al. 2011; Hacar & Tafalla 2011; André 2017) and in simulations (Gómez & Vázquez-Semadeni 2014; Vázquez-Semadeni et al. 2017; Zamora-Avilés et al. 2017). Further, young stellar objects are often observed within these filaments (Hartmann 2002; Teixeira et al. 2006; Chira et al. 2018) implying that star formation rates are elevated within them due to their high density.

1.3.2 The initial conditions of star forming regions

Stars sometimes form in dense ($\gtrsim 1$ $M_\odot$ pc^{-3}) clusters (Lada et al. 1991) and sometimes as more diffuse associations (de Zeeuw et al. 1997; Wright et al. 2014). Two major models of star formation have been proposed: hierarchical and monolithic. In the monolithic model of star formation the vast majority of stars form in dense stellar clusters (Zuckerman & Evans 1974; Krumholz & Tan 2007; Evans et al. 2009), but only around 7 % of these clusters survive beyond around 10 Myr (Lada & Lada 2003). The rest of the clusters are dissolved when gas expulsion (discussed in section 1.4) occurs. Therefore the monolithic model requires that gas expulsion be highly efficient at destroying star clusters. Gas expulsion is the result of the impacts of massive stars on the region. In the monolithic model massive stars form close to one another i.e. they are primordially mass segregated (Murray & Lin 1996; Fischer et al. 1998; de Grijs et al. 2002) via a process such as competitive accretion (Bonnell et al. 2001).

However the monolithic model of star formation cannot explain the existence of young associations that have no kinematic signatures of expansion **(such as Cygnus OB2 (Wright et al. 2014))** or other dynamical evolution (Gieles & Portegies Zwart 2011). Such associations have been observed which are 10s of pc across and only a few Myr old (Wright et al. 2014, 2016). If these associations formed as dense star clusters ($\sim$ 1 pc across) and expanded to this size as per the monolithic model we would expect to see the stars moving systematically outwards from the centre and we do not (Wright et al. 2014).

On the other hand in the hierarchical model (Efremov & Elmegreen 1998) the process of star formation occurs across a large range of densities and spatial scales (Bressert et al. 2010; Bonnell et al. 2011; Gutermuth et al. 2011; Burkert & Hartmann 2013; Gouliermis 2018) via cloud fragmentation, and takes a crossing time or so (Elmegreen 2000). This model permits the existence

of both dense stellar clusters and diffuse, non-expanding associations, with gas expulsion maybe or maybe not playing a large roll in the evolution of star forming regions. In this model massive stars form in 'random' locations rather than forming close together and become mass segregated via dynamical interactions (McMillan et al. 2007; Allison et al. 2009b; Domínguez et al. 2017).

There is also some evidence of massive stars forming in isolation i.e. away from any region that is concurrently forming other stars (de Wit et al. 2005). However closer studies of such apparently isolated stars have found the stars are in fact the most massive members of low mass ($\lesssim 100\ M_{\odot}$) star clusters (Parker & Goodwin 2007; Stephens et al. 2017). It is also hypothesised that these apparently isolated stars are in fact 'runaway' stars, i.e. stars that formed in a star cluster but were ejected at very high velocities (> 30 km s^{-1}) via dynamical interactions (Blaauw 1961; Gvaramadze et al. 2009; Lennon et al. 2018; Massey et al. 2018). Regardless of the origins of apparently isolated stars, it appears that the vast majority of young stars form in the presence of other young stars in GMCs.

1.4 The evolution of star forming regions

In order to begin to understand the evolution of star forming regions (as well as other related topics of interest such as planet formation), there are a myriad of interrelated processes and factors to consider. For example massive stars have a profound impact on the evolution of their star forming regions in multiple ways. The pressure of the radiation they output can substantially impact the surrounding region (Krumholz & Matzner 2009), and feedback from their stellar winds injects momentum into their surrounding medium (Hansen et al. 2012; Raskutti et al. 2016; Grudić et al. 2018). Aditionally, the UV photons they output photoevaporate their surroundings (Fatuzzo & Adams 2008) which can impact planet formation by eroding the protoplanetary disks of nearby stars (Nicholson et al. 2019).

Finally, massive stars impact their environments when they go supernova. Supernovae can enrich nearby protoplanetary disks (Adams et al. 2004; Nicholson & Parker 2017) which influences planet formation, but the most dramatic way that supernovae influence their environments is via their shockwaves. Supernova shockwaves push the gas around them outwards, leaving an empty bubble around them, e.g. Camps-Fariña et al. (2016), and these bubbles can expand to the size of an entire star forming region. A simulation of such an occurrence is shown in Fig. 1.5,

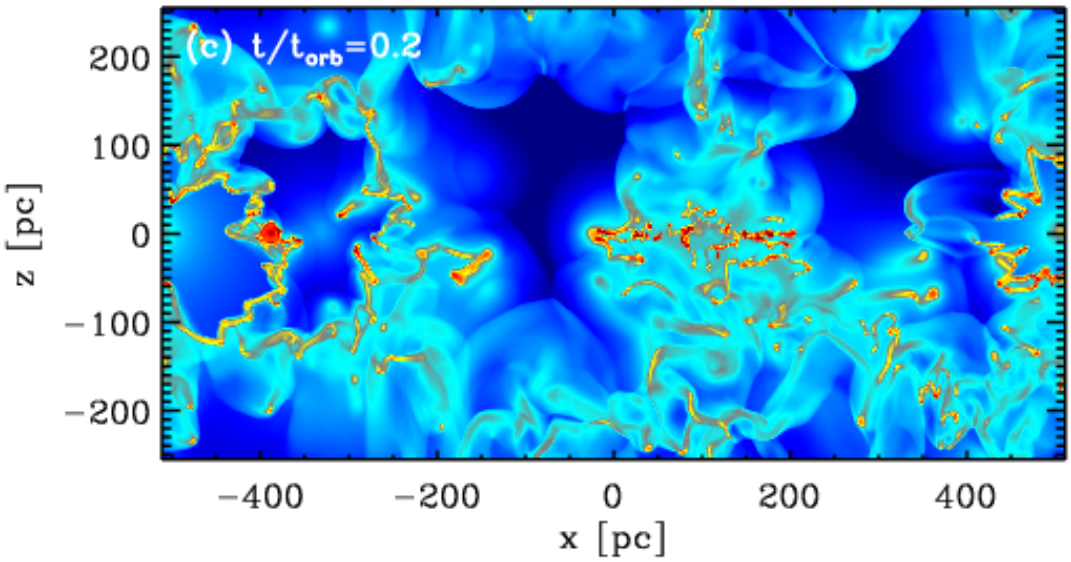

Figure 1.5: This figure is taken from Kim et al. (2011). It shows a hydrodynamic simulation of the ISM in which supernovae have occurred and the expanding shells around them are apparent. The figure is colour coded by gas density with redder gas being more dense and bluer gas less dense.

which is taken from Kim et al. (2011).

This process of gas being pushed out of a star forming region by supernovae shockwaves, stellar winds, and/or photoevaporation (Dale et al. 2012) is called gas expulsion. The swift removal of a significant amount of gas rapidly lowers the potential energy of the region, resulting in its virial factor increasing and the cluster expanding dramatically or even becoming unbound and dissolving into the field (Tutukov 1978; Hills 1980; Goodwin & Bastian 2006; Baumgardt & Kroupa 2007; Moeckel & Bate 2010; Pfalzner & Kaczmarek 2013; Brinkmann et al. 2017).

Whether a cluster survives gas expulsion or not depends partly on the star formation efficency (SFE) with increased SFE resulting in higher survival probability. However it also depends much more strongly on the virial state of the cluster immediately before the onset of gas expulsion, with higher virial ratios decreasing the probability of survival (Goodwin 2009). A cluster that does survive may do so only partially- losing a large number of stars to the field but retaining a small bound core (Goodwin & Bastian 2006).

However it has also been argued that in regions with dense substructures the impact of gas expulsion is minimal. This is because within the substructures gas is depleted as it is accreted onto the YSOs so the substructures become gas poor. As there is little gas in these substructures its removal (via gas expulsion) has little impact on their virial state, and the substructures remain gas-poor and in approximate virial equilibrium up to scales of order 0.5-1 pc (Kruijssen et al.

2012).

The impact of multiple stellar systems on the dynamics of their resident regions must also be considered as such systems can contain a great deal of potential energy**. This energy can be extracted from the binary system by three-body interactions with other members of the region, altering the virial ratio of the region as a whole. Such three body interactions can also** eject stars from the region **entirely** (Hut 1993; Gvaramadze et al. 2012) **if the multiple is wide enough. If there is a small separation between the members of a multiple then from the perspective of other stars in the region in appears to be a single point mass and they do not 'see' its potential energy.** Further, the initial multiple fraction of stars is observed to be high (Simon et al. 1995; Kouwenhoven et al. 2007; Eggleton & Tokovinin 2008; Reipurth et al. 2014), and is even higher for massive stars (Duchêne et al. 2001; Raghavan et al. 2010; Sana et al. 2013) though whether this is primordial or due to dynamics is debated (Pfalzner & Olczak 2007). As a result the initial distribution of periods of multiple systems has been a topic of interest (Zinnecker & Yorke 2007; Kroupa & Petr-Gotzens 2011; Duchene & Kraus 2013), as has the evolution of the binary population of a region with age (Connelley et al. 2008; King et al. 2012a,b).

The myriad dynamic processes outlined in this section (particularly supernovae) destroy the GMCs stars form from on timescales of order a crossing time ($\sim$ 5 Myrs) (Elmegreen 2000; Hartmann 2001, 2003; Larson 2003), causing star formation to cease. Further, these processes cross a huge range of time and spatial scales. For example the photoevaporation of disks depends on the interactions of individual photons and molecules over **nanometers and** a fraction of a second, whereas stars take millions of years to evolve and gravitationally influence objects parsecs away from themselves. This range of scales makes star forming regions very difficult to study. The field has developed tools to assist with the investigation of these regions, and among the most powerful of these are computer simulations, which allow the evolution of regions with given (initial) conditions to be studied. Additionally, simulations circumvent one of the major difficulties associated with studying the evolution of star clusters: these clusters take millions of years to change significantly so changes cannot be observed in a human lifespan. Simulations, however, can be used to study the entire lifetime of a region in a way that is not possible observationally.

N-body simulations are used extensively in this thesis. A description of how these work and why *N*-body simulations are used (as opposed to other methods of simulation) can be found in the next chapter.

1.5 Generating artificial star forming regions for simulations

In order to simulate the evolution of star forming regions artificial star forming regions must be generated. Here we outline different approaches that are taken to doing this and how they are based on what is known about the environments stars form in and the process of star formation.

1.5.1 Stellar positions and velocities

A number of different methods have been used for setting up the initial conditions of star forming regions for simulations. One such method is the box fractal method which attempts to simulate hierarchical star formation. Fractals are used because in the hierarchical model star formation is self similar on different scales, and this is a property which is shared by fractals. Detailed descriptions of the box fractal method presented in Goodwin & Whitworth (2004) can be found in chapter 3 and 4, but because it is used repeatedly in this thesis we also outline it here.

Simply put box fractals are built outwards from a single 'parent' star in the centre of a box. The box is divided into smaller boxes, and a 'child' star is put in the centre of each of them. Some of these child stars a randomly deleted. For those stars which survive the process repeats. They become parents so their boxes are subdivided and new child stars are created and randomly deleted within them. This is repeated for as may generations as necessary to produce the necessary number of stars. The probability the children survive their generation's culling is dictated by the user. If the probability is high the resulting stellar distribution will be relatively smooth, if it is low the distribution will be highly substructured.

The distributions generated by the box fractal method also have velocity structure. The initial parent star is given some velocity and its children inherit it plus a random component. When those (surviving) children become parents their offspring inherit their velocity, again plus a random component and so on. By this method on average stars that are close to each other have similar velocities, and stars that are far apart tend to have very different velocities. This is velocity substructure.

Another fractal-based method is proposed by Lomax et al. (2018). It generates star forming regions by first generating a fractal Brownian motion probability distribution, and then randomly sampling it to get stellar positions.

Another commonly used way of setting up the initial conditions of a region is to make a

Plummer sphere (Plummer 1911) which is a spherical, centrally concentrated distribution. This distribution was modeled to reproduce observations of globular clusters. Setting up simulations of star forming regions will be discussed further in section 1.7 and chapter 2.

1.5.2 The Initial Mass Function (IMF)

Attempts to understand star formation have to be able to explain observed properties of stars that have formed. The most crucial property in determining both the evolution of a star and its impact on its surroundings is its mass. The IMF is the distribution of masses that stars form with, and it is therefore a topic of considerable scientific curiosity. Some observations have found evidence the IMF is invariant across all star forming environments (Bastian et al. 2010; Offner et al. 2014), however other findings have disagreed (Jeffries 2012; Kroupa et al. 2013; Dib 2014). In either case it seems fair to say that the IMF of resolved populations is at least surprisingly constant across a very wide range of star forming environments (we do not discuss the IMF of unresolved populations of stars, such as those in high redshift galaxies, in this work).

Under the assumption that the IMF is universal there have been a number of attempts to mathematically characterise it. Such characterisations are extremely useful for simulating star forming regions. The earliest of these formulations is a power law presented by Salpeter (1955) which empirically fits the high mass slope of the IMF. This is built upon by Kroupa (2001) which instead uses three power law slopes to approximate a peak. The Chabrier formulation of the IMF (Chabrier 2003) has a lognormal distribution at low masses before transitioning to a power law slope at high masses, and the Maschberger IMF (Maschberger 2013) is broadly the same but with a more easily implemented mathematical form.

A comparison of the Salpeter, Kroupa, Chabrier, and Maschberger IMFs can be seen in Fig. 1.6.

1.6 Binary clusters

It is observed that star clusters are sometimes found in close pairs, and statistical arguments show that the number of aparent pairs is far higher than would be expected if clusters are randomly distributed (Rozhavskii et al. 1976; Bhatia & Hatzidimitriou 1988; Bhatia et al. 1991). From this it is concluded that some clusters are in binary or multiple systems, known as binary clusters.

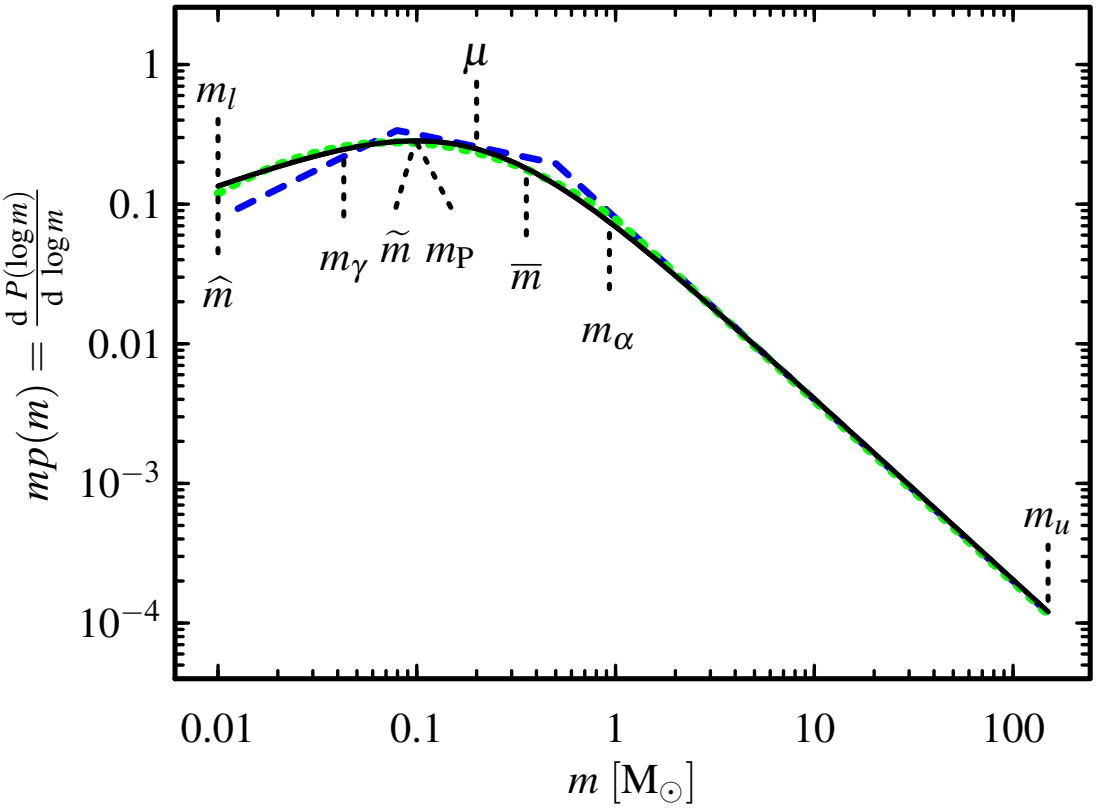

Figure 1.6: The probability density functions for the Kroupa (blue dashed line) Chabrier (green line), and Maschberger (black line) IMFs. At high masses ($\gtrsim 1\ M_\odot$) all three of these approximately match the Salpeter slope. Key masses used in the different models are marked on this figure, which is taken from Maschberger (2013).

Further studies have estimated that the fraction of star clusters in binaries/multiples is around 10 % (Hatzidimitriou & Bhatia 1990; Pietrzynski & Udalski 2000; De La Fuente Marcos & de La Fuente Marcos 2009). The separation of young star forming regions into binary cluster(-like structures) is also observed in N-body simulations, e.g. in Goodwin & Whitworth (2004), Parker et al. (2014), and chapter 3 of this thesis.

1.6.1 Observed features of binary clusters

Binary clusters are generally found to be young (of order 10^7 years old or less) (Kontizas et al. 1993; Pietrzynski & Udalski 2000; De La Fuente Marcos & de La Fuente Marcos 2009; Palma et al. 2016) and the clusters that make up the binary are often have similar ages (Kontizas et al. 1993; Pietrzynski & Udalski 2000) and radii (Bhatia et al. 1991; Pietrzynski & Udalski 2000) as their partners.

'Bridges' of stars between the two components of a binary cluster are sometimes observed. These features have mostly been observed between coeval binary clusters (i.e. the clusters that make up the binary are the same age as each other) such as NGC 2136 / NGC 2137 (Hilker et al. 1995; Mucciarelli et al. 2012), SL 537 / SL 538 (Bica et al. 1996; Dieball & Grebel 1998), SL 387 / SL 385 (Vallenari et al. 1998), and SL 353 / SL 349 (Dieball et al. 2000). However bridges have also been observed between non-coeval binaries e.g. Sersic 13-N and Sersic 13-S (Minniti et al. 2004), though the possibility remains that such apparent bridges may not be real but instead a chance line up with stellar overdensities in the foreground/background.

1.6.2 The formation of binary clusters

Models of binary cluster formation generally assume that the clusters that form a binary were always distinct, but formed near one another. From this starting point, theoretical predictions can be made about the lifespan of binary clusters. This lifespan is predicted to be $\sim 10^7$ years by many independent studies (Sugimoto & Makino 1989; Bhatia 1990; De Oliveira et al. 1998; Portegies Zwart & Rusli 2007; Priyatikanto et al. 2016). These simulations show that after this the clusters would most likely merge if they are gravitationally bound, or, if they formed far enough apart, disperse. It bears noting that the early stages of a cluster merger appear similar to a binary cluster with a bridge between its members (Dieball & Grebel 1998).

Observations find coeval binary clusters older than these predictions can explain, for exam-

ple Leon et al. (1999) finds ages ranging from $10^6 - 10^9$ Myr in a sample of coeval binary clusters. This is the overmerging problem.

One model of binary cluster formation is given by Fujimoto & Kumai (1997) which suggests that binary clusters form as a result of gas cloud collisions triggering fragmentation in two or more close regions. This would explain why many binary clusters are coeval but cannot explain observed binary clusters in areas with low velocity dispersions, as it requires large velocity amplitudes to form them. Further, this model fails to solve the overmerging problem.

Another model states that binary clusters form by tidal capture, and that the likelihood of this is increased by resonant trapping (Dehnen 1998). Resonant trapping is a gravitational effect of the galactic disk, which creates stable 'islands' of phase space. Clusters within these islands can capture each other more easily due to the small difference between the phases of their galactic orbits. This model permits binary clusters with ages of $> 10^7$ years to form via this capture process, making the overmerging problem moot. However this model also predicts that the clusters that make up a binary would generally have different ages to one another, and this is counter to observations as outlined in section 1.6.1.

1.7 Stellar dynamics

Binary clusters are a phenomenon of stellar spatial distributions, but there are a great many other properties that are important to consider when specifying and studying the state of a star forming region. One of the most important of these other factors to consider is the region's stellar velocity distribution. This aspect of star forming regions has historically been less well studied than the stellar spatial distributions because of the increased observational difficulties presented when studying stellar velocities**.**

- In order to measure the proper motions of stars they must be relatively close to us and have very accurate astrometric measurements over a period of time.
- Radial velocity measurements require spectra to be taken so that the relative Doppler shifts of stars in a region can be calculated. For stars in multiple systems multi-epoch data is necessary so that the orbital contribution to each star's **radial** velocity can be modeled and accounted for. Even with multi-epoch data this process is difficult and introduces uncertainties.

Despite the difficulties stellar velocity studies present they are still conducted and much has been learned from them. For example studies have found kinematic substructure in young star forming regions (Fűrész et al. 2006; Jeffries et al. 2014; Tobin et al. 2015; Wright et al. 2016). This informs our understanding of, and allows us to put constraints on, how these regions form. For example, the discovery of two kinematically distinct populations is used as evidence for multiple epochs of star formation in Gamma Velorum (Jeffries et al. 2014; Franciosini et al. 2018). The velocity distributions of prestellar cores have also been studied (André et al. 2007) to better characterise the initial conditions of star forming regions. Further studies have compared the velocity structures of molecular gas and young stars in star forming regions and found that they are correlated (Fűrész et al. 2008).

Studies of velocities within star forming regions have also been undertaken from a theoretical standpoint. It is found that star cluster evolution is an extremely stochastic process, i.e. statistically identical clusters can evolve to be entirely different to one another (Parker & Goodwin 2012). However, general trends can be observed. For example, clusters with a low virial ratio tend to collapse, which destroys their substructure. On the other hand, supervirial clusters generally expand, and their substructure can survive for several crossing times (Goodwin & Whitworth 2004). It is worth noting that as a cluster expands its crossing time changes (Bastian et al. 2008). Therefore a cluster's age in terms of its current crossing time does not necessarily represent how dynamically evolved it is.

The virial state of young star clusters is of considerable interest for differentiating between the hierarchical and monolithic models of star formation, which are discussed in section 1.3.2. The monolithic model predicts that most star clusters become supervirial and dissolve, but this is not required by the hierarchical model. The virial ratio of a region also may or may not be drastically impacted by the process of gas expulsion, as discussed in section 1.4.

The virial state of a region is related to its velocity dispersion as kinetic energy is proportional to the square of the region's velocity dispersion and the region's virial factor is the ratio of its potential and kinetic energies. Hydrodynamical simulations find that the velocity dispersion of stars that form from a molecular cloud is approximately a factor of five smaller than the velocity dispersion of the cloud itself (Offner et al. 2009) which is useful when considering the initial conditions of these regions.

This is a very exciting time for the field of stellar kinematic studies. The existence and

longer time-baselines for proper motion studies, and even more excitingly, the advent of *Gaia* means that high quality stellar velocity data is being produced at an unprecedented rate. For example Gaia surveys over a billion stars and DR2 provides velocity measurements with errors around 0.3 - 1 km s^{-1} for a G dwarf at a distance of 1 kpc. See table 1.1 taken from Lindegren et al. (2018) for more detailed information on the properties and accuracies of sources recorded in Gaia DR2. However, attempts to analyse velocity data have faced difficulties. Several approaches have been attempted, however they have largely depended on subjective, by-eye judgements of the properties of dynamical structures in star forming regions (Galli et al. 2013; Wright et al. 2016; Da Rio et al. 2017; Wright & Mamajek 2018; Kounkel et al. 2018). Such qualitative analysis makes it difficult to rigorously compare regions to each other or to theoretical models, and therefore is of limited use for confidently advancing our understanding of the process of star formation. More quantitative methods of analysing kinematic structure are required.

1.8 Statistical methods

As discussed (see section 1.7) in order to most usefully analyse datasets (both observational and simulated) statistical methods are required. As such a variety of different methods have been developed by the field to quantify different properties of interest in star forming regions.

It is observed that rather than being randomly distributed within star forming regions massive stars appear to be located systematically closer to one another than would be expected by chance (Hillenbrand 1997; Gennaro et al. 2011; Kirk & Myers 2011; Pang et al. 2013; Gavagnin et al. 2017; Plunkett et al. 2018). This phenomenon is referred to as mass segregation, and its origin has been the subject of much debate; is it primordial or the result of dynamics? In order to effectively study how the degree of mass segregation in star forming regions varies with age it must be quantified and several parameters have been developed to do so.

Allison et al. (2009a) presents the Λ parameter, which uses minimum spanning trees (MSTs) to quantify mass segregation. A MST is the shortest possible set of edges that connects a group of points. Λ is the ratio of the mean of the edge length in an MST of random stars ($\langle l_{\rm norm} \rangle$) to the mean edge length in an MST of the most massive stars ($l_{\rm massive}$):

$$\Lambda_{MSR} = \frac{\langle l_{\rm norm} \rangle}{l_{\rm massive}}. \tag{1.17}$$

By this definition a cluster is mass segregated if Λ is greater than 1.

Allison et al. (2009b) applies Λ to simulations of young star forming regions and shows that clusters can dynamically mass segregate within a few Myr, meaning primordial mass segregation isn't necessary to explain mass segregation observed in regions older than this. A follow up paper, Allison et al. (2010), uses simulations to explore parameter space and finds mass segregation correlates with both low virial ratios and high levels of substructure. It also shows that mass segregation can cause a multiple of massive stars to form (similar to the one we see in the ONC), and that the decay of this multiple can destroy its host cluster.

Maschberger & Clarke (2011) proposes calculating Λ using median edge lengths rather than means, which reduces the effects of outliers. A different modification to Λ is proposed in Olczak et al. (2011). They propose using the geometric mean rather than the arithmetic mean. Again, the goal of this modification is to reduce the effects of outliers.

Maschberger & Clarke (2011) also proposes another parameter that attempts to quantify mass segregation, Σ. It is a measure of local surface density of each star:

$$\Sigma = \frac{5}{\pi r_6^2} \tag{1.18}$$

where r_6 is the distance to the 6th nearest neighbour to the star. They apply this Σ to data from simulations, and show that massive stars generally have higher Σ than less massive ones. This indicates that massive stars in their simulations are preferentially found in densely populated areas which often (but not always) signifies mass segregation.

Another property of star forming regions that there have been attempts to quantify is the degree of spatial substructure. One such attempt is made in Cartwright & Whitworth (2004) which presents the Q parameter, which is the ratio of the mean edge length in the cluster's MST ($\bar{m}$) to the average distance between stars in the cluster ($\bar{s}$).

$$Q = \frac{\bar{m}}{\bar{s}} \tag{1.19}$$

Low values of Q (0.45 - 0.7) are evidence of subclustering, and the lower the Q the higher the degree of substructure. Qs greater than 0.8 indicate regions are centrally concentrated. The higher the value of Q the more centrally concentrated the region is.

Another method of quantifying spatial substructure is the INDICATE method presented by

Buckner et al. (2019) which generates an index I for each star. Broadly, I is a measure of how many stars are within a given distance of a certain star compared to the number that would be expected in a uniform stellar distribution. It is calculated by generating a random distribution of points and calculating the average distance of each star to the Nth nearest of these points, where N is chosen by the user. This average distance is $\bar{r}$. For each star, j, the number of other stars within $\bar{r}$ is calculated, this is called N_r. I for star j using nearest neighbour number N is defined as

$$I_{j,N} = \frac{N_r}{N} \tag{1.20}$$

High I indicates that a star is in a clustered environment, and the method has the advantage of being scale independent.

An example of statistical parameters being used to study and compare star forming regions can be found in Parker et al. (2014). Here the changes in Σ, Λ (in its original form), and Q are observed as simulated clusters evolve. Σ of the most massive stars is always found to be higher than the median Σ for all stars. Λ only becomes significant in regions with subvirial and/or clumpy initial conditions. Q is plotted against Λ and Σ, and clusters with different initial conditions are found to evolve (or not evolve) across these plots differently. Inspection of these figures shows that Q tends to increase with time if the initial conditions are virial or subvirial and to stay around the same if they are supervirial. Σ tends to increase in all cases, and Λ tends to increase if regions are not supervirial.

By combining statistical methods (such as those outlined in this section) with data (real or simulated) we can come to meaningful conclusions about the process of star formation (Alfaro & Román-Zúñiga 2018; Lomax et al. 2018; Busquet et al. 2019; Cantat-Gaudin et al. 2019; Reiter & Parker 2019; Rodríguez et al. 2019).

1.9 Major ongoing issues in the field.

Some of the most significant issues facing the field have already been discussed, such as the origin and possible invariance of the IMF (see section 1.5.2), and the mechanism by which star clusters form (see section 1.3.2). Many other questions facing the field are on longer timescales than the lifetimes of individual star forming regions, however.

How the process of star formation has changed with the aging of the universe is one

such question. At high redshift there is evidence galactic mergers play a significant role (Stewart et al. 2009; Perret et al. 2014). As such the study of the kinematic signatures of early galaxies has been valuable in constraining the earliest epoch of star formation (Barnes & Hernquist 1996) but there is still work to be done. The chemistry of this population of stars, known as population III stars, is of particular importance as their metallicity has a significant knock on impact for later populations (Maio et al. 2011) although this is not fully understood. Further, stars at the highest redshifts had significantly higher masses than is the case in the present day (Bromm et al. 2002; Yoshida et al. 2008) increasing the relevance of their supernovae.

Nevertheless the next earliest generation of stars (population II stars) formed from gas with metallicities as low as of order 10^{-4} (Schneider et al. 2003; Latif et al. 2016) and as such are metal poor. They are often found in globular clusters which themselves present a number of ongoing challenges to the field. Specifically very little is understood about how these dense, centrally condensed clusters form. They are generally found at redshifts < 2, (star formation is thought to have peaked at around a redshift of 2 (Hopkins & Beacom 2006)) however observation of high mass (10^4-10^8 $M_\odot$) clusters with ages less than a Gyr means their formation may continue into the present day in galaxy mergers (Bastian et al. 2006; Kruijssen 2014). The possible presence of stars with distinct sets of ages in globular clusters (referred to as multiple populations) is also of considerable interest to the field with regards to studying the formation and evolution of globular clusters (Gratton et al. 2012; Bastian & Lardo 2018).

The age distribution and spatial variation of star clusters within individual galaxies is also a topic of interest as it informs our understanding of the conditions under which star formation occurs and how galaxies evolve (Chandar et al. 2017; Piskunov et al. 2018). The cluster mass function is a key aspect of this and studies comparing it within different galaxies/galactocentric radii (González-Lópezlira et al. 2012; Pflamm-Altenburg et al. 2013) has been useful in terms of constraining how environment impacts the probability/properties of star clusters formed, however these relationships and their physical origins remain not fully understood. Such studies have also offered evidence that cluster's survival times are mass dependent (Lamers et al. 2005; Adamo & Bastian 2018; Messa et al. 2018). The positive relationship between cluster radius and mass has also been a topic of study (Ryon et al. 2015)

and is of considerable curiosity because cluster density is thought to play a significant role in planet formation. This is due to the increased rate of encounters and density of photoionising UV photons in high density star dorming regions, which can erode/disrupt planet-forming disks (see section 1.4).

Reducing time and spacial scales once more, down to the scales of individudal stars, while the main sequence of stars is relatively well understood their births and deaths still contain many mysteries despite extensive study. The evolution of stars on the HR-diagram prior to the zero age of the main sequence is unclear (Palla 2005), though the study of lithium abundances has been of use in investigating this pre main sequence evolution (Xing 2010). With regards to the ultimate fates of stars while it clear mass is the most critical factor in determining when and how a star will 'die' the exact mechanisms remain unclear, especially for type Ia supernovae (Sarbadhicary et al. 2019; Seitenzahl et al. 2019; Soker 2019).

On a technical note, perhaps the most pressing questions facing the field relate to how it must adapt to embrace a new era of big-data astrophysics. This paradigm change, while tremendously exciting, presents numerous challenges. We must first consider what it is that makes data big, which can be broadly split into three features as per Garofalo et al. (2017): volume, variety, and velocity.

- **Volume: the raw number of bytes in a dataset becomes difficult to manage at large scales, and cannot be managed effectively with conventional methods used for smaller datasets.**
- **Variety: astrophysical data comes in countless forms and from a huge number of sources. Using these dataselts together effectively presents a challenge given most are not immediately compatible.**
- **Velocity: The speeds at which data is gathered may exceed the speed at which data can practically and usefully stored. As such high-speed pipelines are required.**

The first of these we will discuss is volume, i.e. simply how to physically store and process such large datasets. For example, FAST generates 20 petabytes per year (Yue & Li 2019), and the data output of LSST over ten years of operation is expected to be in excess of 85 petabytes (LSST Science Collaboration 2009). To put that in perspective as of 2017

the entirely of YouTube's video database totaled 15 petabytes. That said, this is not an entirely untried regime for scientific research; CERN's data centre holds over 230 petabytes (CERN Science Collaboration 2018). That is not to say that the challenges presented to astrophysics by big data have already been solved, but that an interdisciplinary approach to these problems would be advantageous (Hu & Zhang 2017; Kremer et al. 2017).

Obviously it is impossible for these datasets to be analysed entirely manually by humans, they are simply too large. As such while machine learning has been made use of by astrophysics for a long time (Tagliaferri et al. 2003; Baron 2019) it is being employed more and more commonly in order to relive some of this burden (Lochner et al. 2016; Ravanbakhsh et al. 2016). In part this is because of its wider accessibility for example via DAMEWARE (Data Mining and Exploration Web Application REsource) (Brescia et al. 2016), an online data mining framework.

However access to methods and resources is only part of the problem; machine learning itself presents new challenges to the field, specifically how can it be used for maximum efficiency and reliability. As Allen et al. (2019) phrases it 'New tools come with new failure modes, and machine learning [sic] poses the temptation to choose expediency over understanding. A common complaint about machine learning [sic] methods is that they are black boxes that cannot lead to physical understanding'

Next we move on to the issue of variety. This issue is two-fold. The first component is the huge number of sources of data, and how these can be curated and used effectively (Mickaelian 2016). The second is the variety of computing platforms and environments used to handle different varieties of data. Cloud computing platforms in particular present opportunities and challenges (Landoni 2019), and are used both for data analysis e.g. Hong et al. (2019) and management (Blanco-Cuaresma et al. 2019). Cloud resources are offered by Amazon, Google, and Microsoft, amongst others commercial options such as Apache Spark and Hadoop. Additionally some resources have been developed specifically for scientific research, such as SciServer (Taghizadeh-Popp et al. 2020). The question of how to identify and utalise the best of these tools for a specific problem does not have an obvious answer.

Lastly there is the problem of data velocity. Many of the issues related to this also concern the data volume so we will not restate them, simply highlight real-time discovery campaigns as a particularly vulnerable part of the field to this issue (Allen et al. 2019).

Related to the issue of the computing challenges posed to astrophysics by big data are the mathematical issues posed by it. Statistical methods are having to evolve to cope with a data-driven paradigm (Buhlmann & van de Geer 2018; Galeano & Peña 2019). Using statistics to tackle large and complex datasets is one of the main themes of this thesis, which will be further discussed below.

1.10 Unifying themes of this thesis

With these issues in mind this thesis, while made up of a number of distinct projects, has a number of unifying themes which will now be outlined.

1.10.1 Using simulations to study the evolution of star forming regions

The projects in this thesis make use of N-body simulations to study different aspects of how star forming regions evolve. Chapter 3 investigates the morphological evolution of some some simulated star forming regions into two distinct clumps, and argues this is how binary clusters form. It also contains a parameter space study in which a large number of simulations are used to study the impact of the initial conditions of a region on its probability of undergoing different modes of morphological evolution.

Chapter 4 is concerned with studying velocity structure and makes use of simulations to test a method of quantifying this. It also uses simulations with known and characteristic velocity structures to benchmark the method's performance when faced with simulated observational constraints. Chapter 5 uses this method to investigate how Cygnus OB2 may have formed/evolved. It highlights the region's high velocity dispersion and very limited velocity structure to suggest that most stars in the observed field of view likely did not form in that part of the Cygnus OB2 region

Chapter 6 uses simulations to explore how stars are ejected from star forming regions with a focus on how different properties of the stars and region correlate with this. No high mass runaway stars are found, supporting the idea discussed in section 1.3.2 that apparently isolated high mass stars are not in fact runaways but instead the most massive members of low-mass clusters.

1.10.2 The dynamics of star forming regions

Chapter 3 we find that distinct regions with very different velocities can develop from single star forming regions. Further we find that in order for this to occur there must be velocity substructure of *some* sort in the region's initial conditions. Two realistic methods of generating initial velocity substructure are applied (one imposes a turbulent velocity field, the other uses inherited velocities to mimic how velocities are inherited from the molecular gas stars form from) and both result in binary cluster formation. However no binary clusters form in another set of simulations in which there is no initial velocity structure.

Chapter 4 is concerned with the development of a technique to study how velocities are structured in star forming regions. This technique calculates how different stellar velocities are on average as a function of how far apart the stars are and produces a figure. Velocity 'difference' can be defined in different ways which highlight different aspects of a region's velocity structure. Two definitions, referred to the magnitude and directional definitions are used. The former acts as a raw measure of the magnitude of the difference between velocity vectors, while the latter highlights regions which are expanding/contracting and how sub-regions are moving relative to one another.

Chapter 5 applies the method presented in chapter 4 to investigate the velocity structure of Cygnus OB2. Velocity substructure is found on scales < 0.5 pc which may indicate the presence of bound sub-groups on this size scale. No evidence of systematic expansion or collapse is found in any part of the region.

Chapter 6 looks into the ejection of stars from young star forming regions. Ejected stars by their very definition have velocities that are very different to their regions of origin, and chapter 6 looks into how these high velocity amplitudes come to be.

1.10.3 Using statistical methods to exploit data

Chapter 3 includes and analyses a set of 450 simulations which are made up of 50 of each of 9 different sets of initial conditions. These initial conditions cover a small area of 2D parameter space. Three different initial virial ratios are used for the simulations, one of which is subvirial, (0.3), one of which is virialised (0.5), and one of which is supervirial (0.7) Additionally, three different initial degrees of substructure are imposed by specifying the fractal dimension of the initial conditions, D as 1.6, 2.2 and 2.9.

Without any processing, just the raw data of positions and velocities at given timesteps, the evolutionary patterns of these simulations are inscrutable. In order to analyse the outcomes of this set of simulations they are classified into different evolutionary patterns. The correlation of different patterns with different initial conditions can then be more readily studied by conventional statistics. However the process of classification is labour intensive and while a large sample size is necessary to provide reliable results this study approaches the limits of what can be achieved without automation. As such this acts as a case study on the limits of conventional statistical methods for analysing such sets of N-body simulations.

In chapter 4 a new statistical technique for analysing velocity structure in star forming regions is presented. It is also tested on synthetic datasets and its performance when faced with realistic simulated observational constraints, such as missing data from low mass stars, observational uncertainties, and binary systems is assessed. The method is found to be resilient against all of these and in chapter 5 it is applied to a real dataset.

Chapter 6 makes use of a number of different statistical techniques to study stellar ejections, such as cumulative distribution plots and violin plots. This demonstrates how a statistical technique does not necessarily have to provide a single numerical output to be a valuable tool for data analysis.

1.11 Summary

In conclusion star formation and the evolution of star forming regions are extremely complex, rapidly-evolving fields of research. Findings in these arenas have major implications for other fields, for example by informing our understanding of the conditions necessary for life to develop. **This thesis makes use of simulations and statistical techniques to explore a number of open questions in this field, particularly those related to stellar dynamics.**

Quantity	Median value at magnitude G										Unit
	$\leqslant 12$	13	14	15	16	17	18	19	20	21	
Fraction of sources with 5-param. solution	99.1	99.0	99.0	99.0	98.9	98.6	97.6	94.5	82.9	15.9	%
Standard uncertainty in α ($\sigma_{\alpha*}$) at J2015.5	0.033	0.023	0.023	0.031	0.047	0.077	0.137	0.268	0.548	1.457	mas
Standard uncertainty in δ (σ_{δ}) at J2015.5	0.030	0.022	0.020	0.027	0.041	0.069	0.123	0.242	0.490	1.559	mas
Standard uncertainty in ϖ (σ_{ϖ})	0.041	0.029	0.028	0.038	0.057	0.094	0.165	0.317	0.651	2.104	mas
Standard uncertainty in $\mu_{\alpha*}$ ($\sigma_{\mu\alpha*}$)	0.068	0.047	0.047	0.063	0.096	0.158	0.280	0.550	1.164	3.114	mas yr^{-1}
Standard uncertainty in μ_{δ} ($\sigma_{\mu\delta}$)	0.059	0.042	0.040	0.054	0.082	0.137	0.243	0.479	1.011	3.374	mas yr^{-1}
Fraction with significant excess noise	20.6	21.0	17.8	17.9	18.4	19.2	20.6	21.2	18.2	10.6	%
Excess source noise (when significant)	0.183	0.249	0.311	0.331	0.367	0.474	0.701	1.226	2.235	4.563	mas
Number of visibility periods used	13	13	13	13	13	12	12	12	12	9	
Number of field-of-view transits used	26	26	26	26	25	25	24	23	22	12	
Number of good CCD observations AL	220	227	226	223	218	215	212	199	194	102	
Fraction of bad CCD observations AL	2.7	0.8	0.0	0.4	0.4	0.4	0.4	0.5	0.4	0.5	%

Table 1.1: Properties and errors of *Gaia* DR2 sources with full astrometric solutions. This is table B.1 in Lindegren et al. (2018). The table gives the median quantities at the magnitudes indicated in the header. For $G \leqslant 12$ the median values were computed using all the sources in that range; at other magnitudes about 2 million sources were used around the indicated G.

Chapter 2

N-body simulations

2.1 Definition

The N-body problem involves N point mass particles interacting via gravity. It is a referred to as a 'problem' because it has no analytic solution when $N > 2$ except in special cases, however an approximate solution can be found using N-body simulations. In **star forming regions** stellar-stellar interactions are dominated by gravity**. The typical distances between stars vastly exceed the scales of the stars themselves; $R_\odot$ = 6.96 $\times 10^8$ m while young star clusters are typically of order 1 pc (3.09 $\times 10^{16}$ m). As a result tidal forces can be neglected. This in combination with the fact that stars are smooth spheroids means they can be well approximated in simulations** by point mass particles. As such these simulations are uniquely well suited for studying the evolution of star forming regions.

Because N-body simulations rely on very simple physics they are relatively quick to perform, however neglecting all forces but gravity does limit the physics they can incorporate. A review of N-body simulations can be found in Dehnen & Read (2011). The main N-body simulation code I will be using is KIRA which is part of the STARLAB package presented in Portegies Zwart et al. (2001), however other N-body codes exist such as NBODY6 (Aarseth 2003). **KIRA is chosen for this work because of features it incorporates to improve the speed and accuracy of simulations (which are discussed further in Section 2.3.2), and because of existing familiarity with it in the Sheffield astrogroup.**

2.2 Solving the N-body problem

N-body simulations take the positions and velocities of point masses and calculates the forces they exert on one another according to **Newton's** law of universal gravitation. According to this law the gravitational force stars i and j exert on each other is:

$$\boldsymbol{F_{ij}} = \frac{Gm_i m_j}{|\ \boldsymbol{r_{ij}}^2\ |}\hat{\boldsymbol{r_{ij}}} \tag{2.1}$$

Where G is the gravitational constant, m is mass, and $\boldsymbol{r_{ij}}$ is the distance between stars i and j. From these forces the future positions and velocities of the particles after some timestep are estimated. This is repeated over many timesteps until the system has been evolved to the desired age or some other **criterion** is met. Using this method for a given set of initial conditions a simulation of how a region would evolve is generated. To advance the simulation by a timestep these simulations make use of a fourth order Hermite integrator which is outlined below.

2.2.1 Fourth Order Hermite integrator

This section is based on Aarseth (2003)**,** Allison (2010) and Dehnen & Read (2011). The fourth order Hermite integrator is also known as the Predict-Evaluate-Correct (PEC) scheme. As the name suggests it has three steps; predict, evaluate, and correct**.**

2.2.2 Predict

Use a simple Taylor series to predict each particles' position $\boldsymbol{x}$ and velocity $\dot{\boldsymbol{x}}$ after one timestep Δt, where t is time and $\boldsymbol{a}$ is acceleration.

$$\boldsymbol{x}_{t+\Delta t} = \boldsymbol{x}_t + \dot{\boldsymbol{x}}_t \Delta t + \frac{1}{2}\boldsymbol{a}_t \Delta t^2 + \frac{1}{6}\dot{\boldsymbol{a}}_t \Delta t^3, \tag{2.2}$$

$$\dot{\boldsymbol{x}}_{t+\Delta t} = \dot{\boldsymbol{x}}_t + \boldsymbol{a}_t \Delta t + \frac{1}{2}\dot{\boldsymbol{a}}_t \Delta t^2. \tag{2.3}$$

2.2.3 Evaluate

From these predicted positions and velocities, evaluate what acceleration and jerk (the time derivative of acceleration) each particle will experience at $t + \Delta t$ **(Dehnen & Read 2011)**. This involves

calculating the force exerted on each particle (indexed by i) by every other particle (index j). G is the gravitational constant.

$$\boldsymbol{a}_{i,t+\Delta t} = -G \sum_{i \neq j}^{N} m_j \frac{\boldsymbol{x}_{i,t+\Delta t} - \boldsymbol{x}_{\mathbf{j},t+\Delta t}}{|\boldsymbol{x}_{i,t+\Delta t} - \boldsymbol{x}_{j,t+\Delta t}|^3}, \tag{2.4}$$

$$\dot{\boldsymbol{a}}_{i,t+\Delta t} = -G \sum_{i \neq j}^{N} m_j \frac{\boldsymbol{x}^2_{ij,t+\Delta t} \dot{\boldsymbol{x}}_{ij,t+\Delta t} - 3\boldsymbol{x}_{ij,t+\Delta t}(\boldsymbol{x}_{ij,t+\Delta t} \cdot \dot{\boldsymbol{x}}_{ij,t+\Delta t})}{|\boldsymbol{x}_{i,t+\Delta t} - \boldsymbol{x}_{j,t+\Delta t}|^5}. \tag{2.5}$$

N.B the notation in equation 2.5 is such that $\dot{\boldsymbol{x}}_{ij,t+\Delta t}$ is the velocity vector between stars i and j at time $t + \Delta t$.

2.2.4 Correct

Use these values for $\boldsymbol{a}_{t+\Delta t}$ and $\dot{\boldsymbol{a}}_{t+\Delta t}$ to calculate more accurate values for $\boldsymbol{x}_{t+\Delta t}$ and $\dot{\boldsymbol{x}}_{t+\Delta t}$. This is done by first expanding the Taylor series for position, velocity, acceleration and jerk:

$$\boldsymbol{x}_{t+\Delta t} = \boldsymbol{x}_t + \dot{\boldsymbol{x}}_t \Delta t + \frac{1}{2}\boldsymbol{a}_t \Delta t^2 + \frac{1}{6}\dot{\boldsymbol{a}}_t \Delta t^3 + \frac{1}{24}\ddot{\boldsymbol{a}}_t \Delta t^4, \tag{2.6}$$

$$\dot{\boldsymbol{x}}_{t+\Delta t} = \dot{\boldsymbol{x}}_t + \boldsymbol{a}_t \Delta t + \frac{1}{2}\dot{\boldsymbol{a}}_t \Delta t^2 + \frac{1}{6}\ddot{\boldsymbol{a}}_t \Delta t^3 + \frac{1}{24}\dddot{\boldsymbol{a}}_t \Delta t^4, \tag{2.7}$$

$$\boldsymbol{a}_{t+\Delta t} = \boldsymbol{a}_t + \dot{\boldsymbol{a}}_t \Delta t + \frac{1}{2}\ddot{\boldsymbol{a}}_t \Delta t^2 + \frac{1}{6}\dddot{\boldsymbol{a}}_t \Delta t^3, \tag{2.8}$$

$$\dot{\boldsymbol{a}}_{t+\Delta t} = \dot{\boldsymbol{a}}_t + \ddot{\boldsymbol{a}}_t \Delta t + \frac{1}{2}\dddot{\boldsymbol{a}}_t \Delta t^2, \tag{2.9}$$

and then eliminating $\ddot{\boldsymbol{a}}_t$ and $\dddot{\boldsymbol{a}}_t$ to find

$$\boldsymbol{x}_{t+\Delta t} = \boldsymbol{x}_t + \frac{1}{2}(\dot{\boldsymbol{x}}_{t+\Delta t} + \dot{\boldsymbol{x}}_t)\Delta t + \frac{1}{12}(\boldsymbol{a}_t - \boldsymbol{a}_{t+\Delta t})\Delta t^2, \tag{2.10}$$

$$\dot{\boldsymbol{x}}_{t+\Delta t} = \dot{\boldsymbol{x}}_t + \frac{1}{2}(\dot{\boldsymbol{a}}_{t+\Delta t} + \boldsymbol{a}_t)\Delta t + \frac{1}{12}(\dot{\boldsymbol{a}}_t - \dot{\boldsymbol{a}}_{t+\Delta t})\Delta t^2. \tag{2.11}$$

Finally, substitute $\boldsymbol{a}_{t+\Delta t}$ and $\dot{\boldsymbol{a}}_{t+\Delta t}$ as estimated in the evaluate step into these equations to obtain the corrected position and velocity after the timestep. This process is repeated for as many

timesteps as necessary to evolve the region to a desired age.

2.3 Techniques to improve speed and accuracy

2.3.1 Variable timesteps

The choice of how long a timestep, Δt, to use is a critical one, and it contains an unavoidable trade-off. The shorter Δt is the more accurate the resulting simulation will be. This is because the terms which are not calculated in the Taylor series (and therefore introduce error into the results) all depend on Δt taken to increasingly high powers. Therefore the smaller Δt is the smaller error is introduced.

However the drawback of having a small Δt is that it is more computationally expensive. For example, if a simulation is to evolve a star forming region to an age of 10 Myr in timesteps of 0.1 Myr the positions and velocities of the stars only need to be recalculated 100 times. If the timestep is 0.01 Myr then this increases to 1000 and the simulation will take ten times longer to run.

Variable timesteps are a computational tool used to try to maximise accuracy while minimising runtime by not using a 'one size fits all' timestep. Instead Δt is varied between stars depending on the rate at which their acceleration and its time derivatives are changing. Stars which are experiencing rapid changes in their accelerations are regularly updated (i.e. they are evaluated with small timesteps) in order to produce reliable results. In contrast stars with more slowly changing accelerations, such as those in low density regions, are evaluated with much longer timesteps.

The procedure for advancing a simulation from time t to time $t+\Delta t$ using variable timesteps is now described. This explanation will refer to a diagram of the process shown in Fig. 2.1 to improve clarity. Simulations have different 'levels' of timesteps, the highest of which is the full Δt. The next is $\frac{\Delta t}{2}$, and the next $\frac{\Delta t}{4}$ and so on with Δt divided by increasing powers of two. Only three levels (Δt, $\frac{\Delta t}{2}$, and $\frac{\Delta t}{4}$) are shown in Fig. 2.1 to prevent the figure becoming crowded, but any number of levels can be used. At time t (the far left hand side of Fig. 2.1) the conditions each star is experiencing are assessed and the best level of timestep for them is chosen.

Once the stars have all been allocated to levels the simulation is advanced. The process of advancing a simulation at a given time is as follows:

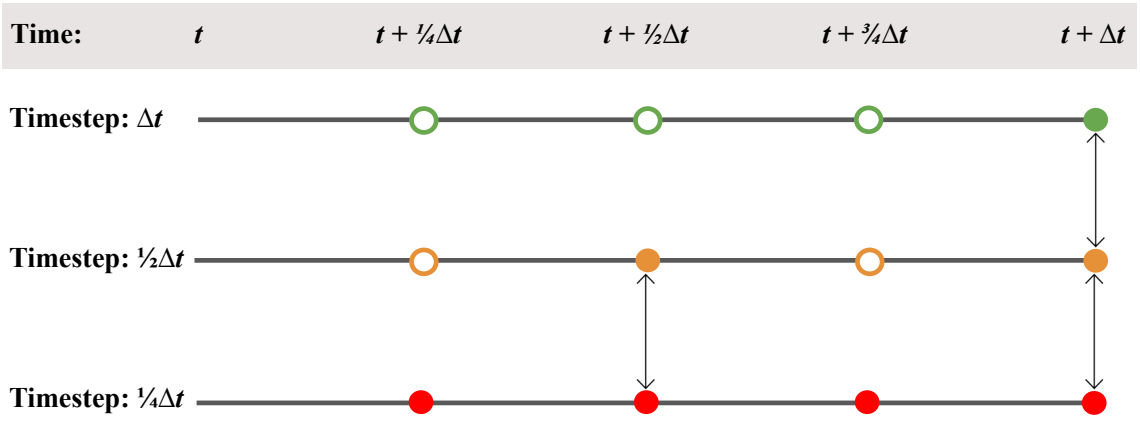

Figure 2.1: A diagram of how an N-body simulation is updated with variable timesteps. In this figure time progresses from left to right starting at t and ending at $t + \Delta t$. It shows three levels of timesteps, once every Δt (top), once every $\frac{\Delta t}{2}$ (middle), and once every $\frac{\Delta t}{4}$ (bottom). Coloured circles show where the positions and velocities of stars are recalculated between t and $t + \Delta t$. These are green on the Δt timestep level, orange on the $\frac{\Delta t}{2}$ timestep level and red on the $\frac{\Delta t}{4}$ level. Solid circles are used where the stars are updated by taking into account the forces exerted on them by all other stars via the fourth order Hermite integrator. Hollow circles are used where stellar positions and velocities are updated using only the star's previously calculated spatial and dynamical properties.

1. Advance the positions and velocities of all the stars by the smallest timestep.

   (a) For stars evaluated on this timestep update them by taking into account the forces exerted on them by all the other stars using the fourth order Hermite integrator. These types of updates are shown by solid circles in Fig. 2.1.

   (b) For stars evaluated on timesteps longer than this calculate their new position and velocity using previously calculated values of their position and kinematic properties. These types of updates are shown by hollow circles in Fig. 2.1.

2. If stars on more than one timestep level have been updated then, if appropriate, stars can be swapped between these levels. For example at $\frac{\Delta t}{2}$ both stars with timesteps of $\frac{\Delta t}{4}$ and $\frac{\Delta t}{2}$ are updated. This swapping is illustrated by double-headed arrows in Fig. 2.1.

3. Return to step 1.

2.3.2 Other techniques employed by KIRA to improve speed and accuracy

N-body simulations make use of other 'tricks' to improve their performance. One such trick is to convert their input into N-body units by doing things such as setting commonly used values such as the gravitational constant G and the total mass in the system M to 1 as outlined in Hénon (1971).

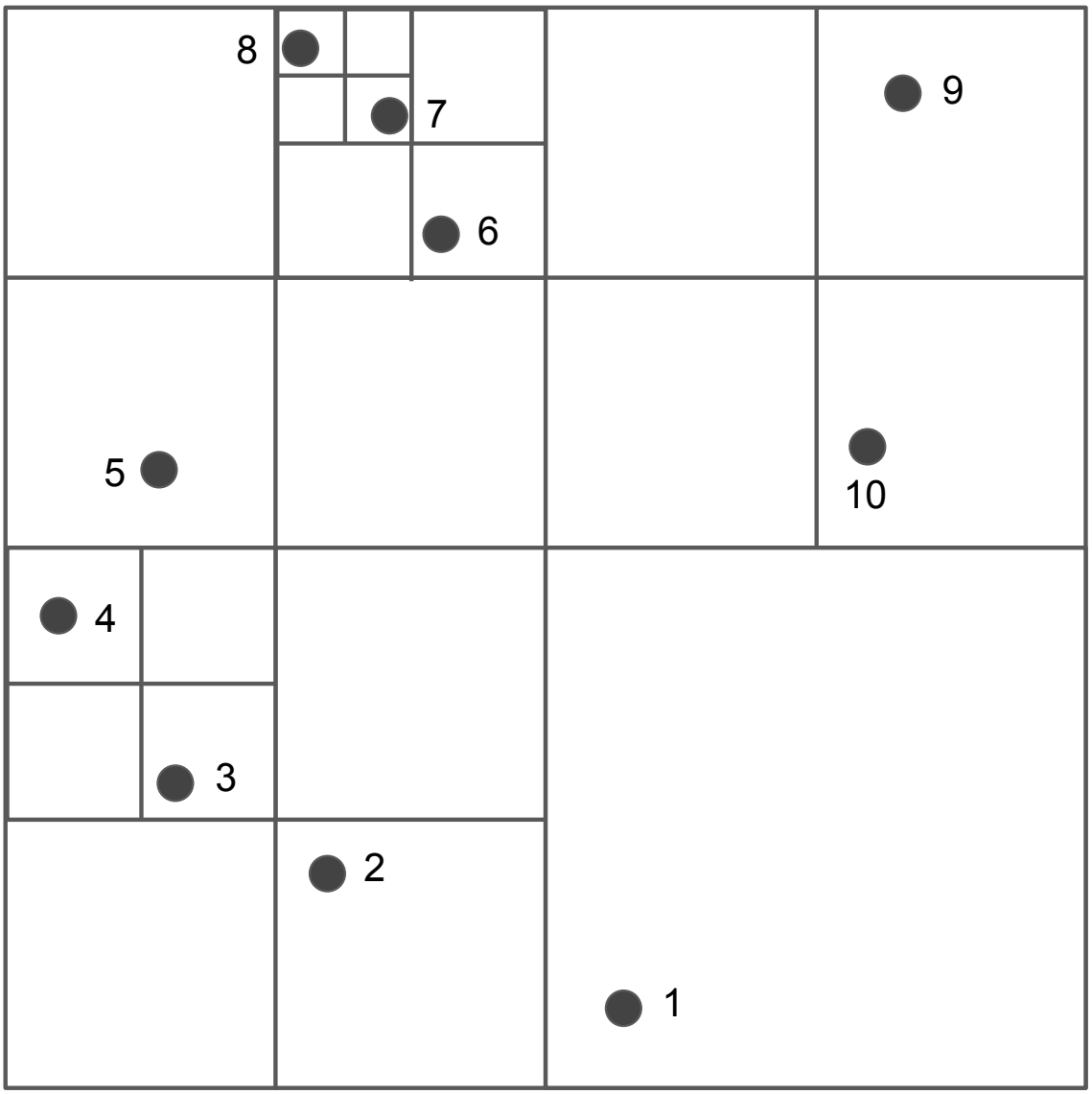

Figure 2.2: A system of ten particles for which a tree has been built. This figure is adapted from educational materials developed by Prof. Frans Pretorius for Princeton university, which can be viewed here `http://physics.princeton.edu/~fpretori/Nbody/intro.htm`.

Doing this frees up more bytes to define useful information within the simulation. If, for example, masses were stored in kg bytes would need to be occupied storing a power of $\sim 10^{30}$. By removing that need those bytes can instead store additional decimal places of simulation parameters, such as stellar masses. **Because of the chaotic nature of dynamical systems small improvements in accuracy can propagate exponentially over many timesteps and have a large impact on simulation results.**

Another method used to speed up N-body simulations (albeit at the cost of some accuracy) is to make use of computational trees. Trees divide the physical space the simulation takes place

over into subregions, which themselves are subdivided into smaller regions if they contain multiple particles and so on. An illustration of such a tree for a system of ten particles is shown in Fig. 2.2. This example shows a Barnes-Hut tree (Barnes & Hut 1986)**, the type used by KIRA,** although other methods of constructing trees exist. As you can see in this figure particle 1 is alone in its region so the region is not subdivided further. In contrast particles 2, 3, and 4 are in the same subregion so the region is subdivided once, which isolates particle 2, and then again to isolate particles 3 and 4. A further level of region subdivision is necessary to isolate particles 7 and 8.

In each subregion the total mass, location of the centre of mass, and the quadropole and octopole moments of the cell are calculated. These can be used instead of calculating the impacts of the individual stars in some cases, which saves time. For example in Fig. 2.2 particle 1 is very far away from particles 6, 7 and 8, and as such it is likely the gravitational force they exert on it will be weak. Therefore instead of laboriously calculating the gravitational forces each of these three particles exert on particle 1 the total mass and centre of mass of their subregion (which was calculated when building the tree) can be used instead, speeding up the calculation at the cost of a small amount of accuracy.

2.4 Other methods of simulating star forming regions

Adaptive mesh refinement (AMR) (Berger & Jameson 1985) and smoothed particle hydrodynamics (SPH) (Gingold & Monaghan 1977) are two more sophisticated methods used to simulate star forming regions. They incorporate more physics, but require increased complexity and runtime. Further, such complex simulations are often vulnerable to effects such as artificial viscosity which distort their output. Hybrid N-body/SPH codes have been created, such as SEREN (Hubber et al. 2011). The bridging of the N-body and SPH methods is improved in Hubber et al. (2013). More recently SEREN has been succeeded by GANDALF (Hubber & Rosotti 2016).

Further details on alternative methods of simulating star forming regions are not provided here as they are not used in this thesis.

The major exclusions from KIRA are gas and stellar evolution. However both of these can be approximated within KIRA. For gas this is done by including a crude background potential energy to mimic the potential that would be induced by the presence of gas.

Stellar evolution can be mimicked by reducing the masses of stars as a function of time,

however the simulations in this paper are mostly too short for stellar evolution to have a large impact (∼ 10 Myr or so). Further they had few enough stars (∼ 1000) that each simulation was only likely to contain very few high mass stars, which are most strongly impacted by stellar evolution. As a result this feature of KIRA is not used.

Chapter 3

The origins of binary clusters

3.1 Summary

This chapter presents the paper 'How do binary clusters form?' (Arnold et al. 2017). In this work *N*-body simulations are performed and it is demonstrated that single star forming regions can divide into binary (or higher-order multiple) clusters. It is proposed that this may be the mechanism by which binary/multiple clusters form in reality. It is further demonstrated that velocity substructure in the initial conditions is required for such division to occur. Finally a parameter space study is conducted and the rates and properties of multiple cluster formation are recorded. It is found that in order for binary clusters to form a region must typically be at or above a virial ratio of 0.5. It is also found that the primary determinant of the mass ratios of multiple clusters that form is the initial degree of substructure in the region, and this relationship is nonlinear.

3.2 Description of my contribution to this work

The original idea for this paper was devised by S. Goodwin, who also provided advice as this study was conducted. Further he provided guidance on the writing of the paper, and feedback/editing on multiple drafts. An interface provided by D. Griffiths was used to assist in setting up and running the simulations presented in this paper. Additional feedback on the paper was provided by R. Parker. Otherwise the work presented in this chapter is my own.

3.3 The paper

The published version of Arnold et al. (2017) is presented here:

Monthly Notices
of the
ROYAL ASTRONOMICAL SOCIETY

MNRAS **471,** 2498–2507 (2017)
Advance Access publication 2017 July 13

doi:10.1093/mnras/stx1719

How do binary clusters form?

Becky Arnold,* Simon P. Goodwin, D. W. Griffiths and Richard. J. Parker†
Department of Physics and Astronomy, University of Sheffield, Sheffield S3 7RH, UK

Accepted 2017 July 7. Received 2017 June 28; in original form 2016 December 20

ABSTRACT

Approximately 10 per cent of star clusters are found in pairs, known as binary clusters. We propose a mechanism for binary cluster formation; we use *N*-body simulations to show that velocity substructure in a single (even fairly smooth) region can cause binary clusters to form. This process is highly stochastic and it is not obvious from a region's initial conditions whether a binary will form and, if it does, which stars will end up in which cluster. We find the probability that a region will divide is mainly determined by its virial ratio, and a virial ratio above 'equilibrium' is generally necessary for binary formation. We also find that the mass ratio of the two clusters is strongly influenced by the initial degree of spatial substructure in the region.

Key words: stars: formation – stars: kinematics and dynamics – open clusters and associations: general.

1 INTRODUCTION

Star clusters are fascinating objects as they provide crucial tracers of the star formation and chemical and dynamical histories of galaxies. Most star clusters are thought to form in a single star formation event and remain as coherent bound entities following this event. (If they disperse rapidly they are not 'star clusters' under this definition.)

An interesting observation is that star clusters are quite often found in pairs or higher-order systems (Rozhavskii, Kuz'mina & Vasilevskii 1976). Such pairs are an expected result of chance line-ups (clusters far from each other appearing to be close due to viewing angle; e.g. Conrad et al. 2017). However, once the effects of chance line-ups are accounted for a surplus of cluster pairs is still observed, indicating that at least some of them are related objects which are physically close to one another. Studies of the Large Magellanic Cloud (LMC) and Small Magellanic Cloud (SMC) appear to show that roughly 10 per cent of clusters are in such pairs, which are known as binary clusters (Pietrzynski & Udalski 2000). The fraction of binary clusters in the Milky Way has been found to be lower than this by some studies (Subramaniam et al. 1995) and about the same by others (De La Fuente Marcos & de La Fuente Marcos 2009).

Binary clusters are systematically younger than single clusters, e.g. half of the clusters in binaries identified by De La Fuente Marcos & de La Fuente Marcos (2009) are <25 Myr old, and almost all of these are in coeval pairs (see also Dieball, Müller & Grebel 2002; Palma et al. 2016). This is not an unusual result; the clusters that constitute a binary are often coeval (e.g. Kontizas, Kontizas & Michalitsianos 1993; Mucciarelli et al. 2012). The most obvious explanation for pairs of clusters with very similar ages is that their formation was linked in some way, but the origins of these pairs are not understood.

Some multiplicity may be expected as a natural consequence of structure in molecular clouds (e.g. Elmegreen & Falgarone 1996). This paper presents an additional mechanism for binary cluster formation: the division of a single star-forming region (as seen to some degree in e.g. Goodwin & Whitworth 2004 and Parker et al. 2014).

In this paper, we present a series of *N*-body simulations. We show that, at least for some initial conditions, binary clusters are a fairly common outcome of the dynamical evolution of these systems. We describe our initial conditions in Section 2, present detailed results from a small set of simulations in Section 3, conduct a parameter space study in Section 4 and conclude in Section 5.

2 METHOD

We perform purely *N*-body simulations of fractal distributions using the KIRA integrator, which is a part of STARLAB (Portegies Zwart et al. 1999; Portegies Zwart et al. 2001). Our simulations include no gas, no stellar evolution and no external tidal fields. As such, they are very simple numerical experiments, but we argue that they capture all of the essential physics of a possible binary cluster formation mechanism. We run the simulations for 20 Myr.

2.1 Positions and masses

Artificial young star-forming regions are constructed using the box fractal method, which is described in detail in Goodwin & Whitworth (2004). In brief, box fractals are generated by creating a cube and placing a 'parent' star at its centre. The cube is divided into subcubes, which have 'child' stars placed at their centres, with

* E-mail: rjarnold1@sheffield.ac.uk
† Royal Society Dorothy Hodgkin Fellow.

© 2017 The Authors
Published by Oxford University Press on behalf of the Royal Astronomical Society

Downloaded from https://academic.oup.com/mnras/article-abstract/471/2/2498/3964531 by University of Sheffield user on 14 May 2019

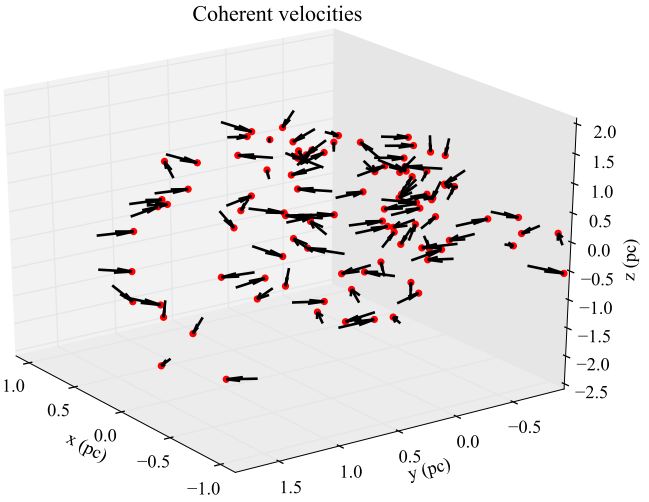

Figure 1. A set of initial conditions demonstrating velocity structure in a region with 100 stars and a radius of 1 pc. The red dots indicate the positions of stars, and their velocity vectors are denoted by black arrows.

noise added to avoid a grid-like structure. Parent stars are deleted, and the children become the new generation of parents. This process is repeated until the desired number of stars, N, has been overproduced. Finally, a sphere of radius R is cut from the initial box, and stars are randomly deleted until the N stars remain. We take regions with $N = 1000$ and $R = 2$ pc as our 'standard'. The degree of substructure (space-filling) is set by the fractal dimension D (e.g. 1.6 is very substructured and 3 is roughly uniform density).

The stars are assigned masses drawn randomly from the Maschberger IMF (Maschberger 2013) with the scale parameter $\mu = 0.2\,\mathrm{M}_\odot$ and the high mass exponent $\alpha_{\rm IMF} = 2.3$. The low mass exponent is calculated using $\beta = 1.4$. The lower and upper mass limits used are 0.1 and 50 $\mathrm{M}_\odot$, respectively. The Maschberger IMF is similar to the Chabrier IMF (Chabrier 2003) and the Kroupa IMF (Kroupa 2002).

2.2 Velocity structure

As will become apparent later in the results, the velocity structure of the fractal is very important. The gas from which stars form is known to have a complex (turbulent) structure (Larson 1981), and the stars in young regions appear to retain this structure (e.g. Fűrész et al. 2006; Jeffries et al. 2014; Tobin et al. 2015; Wright et al. 2016).

To mimic this, we assign star velocities such that the regions are velocity coherent; stars that form near each other have initially similar velocities. We do this by one of two methods: either inheriting velocities from their parents as the fractal is generated (this is the main method used) or by imposing velocities from a divergence-free turbulent velocity field.

Inherited velocities: Following Goodwin & Whitworth (2004), parent stars at the first level are given a random velocity. Child stars inherit their parent's velocity plus a random component that scales with the depth in the fractal (i.e. the random component is large at the higher levels and becomes smaller). This creates a velocity field in which stars that are close together in space tend to have initially similar velocities.

Fig. 1 shows an $N = 100$ fractal produced by this method. Star positions are indicated by red dots plotted in three-dimensional space and their velocities by arrows. As can be seen, the velocity field has local 'coherence'. For example, the stars on the upper far left of the figure are all moving to the right, while on the lower far left there is a group of four stars moving downwards and slightly to the left.

Turbulent velocity fields: We generate divergence-free turbulent velocity fields with a power spectrum $P(k) = k^{-\alpha}$ for the region, where $\alpha = 2$ (e.g. Burkert & Bodenheimer 2000; Lomax et al. 2014). The initial positions of the stars are mapped on to these fields, and they are assigned the field velocity at their locations.

Table 1. Letters are used to describe the initial conditions in each set of simulations. Two parameters are varied: the fractal dimension D and the virial ratio (i.e. the ratio of kinetic to potential energy) $\alpha_{\rm vir}$. Highly substructured simulations ($D = 1.6$) are denoted by the letter 'H', moderate substructure ($D = 2.2$) is denoted by the letter 'M' and smooth structure ($D = 2.9$) by 'S'. Simulations of cool regions ($\alpha_{\rm vir} = 0.3$) are denoted by 'C', virialized regions ($\alpha_{\rm vir} = 0.5$) are denoted by 'V' and warm regions ($\alpha_{\rm vir} = 0.7$) by 'W'.

		D		
		1.6	2.2	2.9
$\alpha_{\rm vir}$	0.3	HC	MC	SC
	0.5	HV	MV	SV
	0.7	HW	MW	SW

2.3 Virial ratio

Finally, the velocities are scaled to set the desired virial ratio, $\alpha_{\rm vir} = T/|\Omega|$ (where T is the total kinetic energy and Ω is the total potential energy).

2.4 Ensembles

We perform simulations with fractal dimensions of $D = 1.6$, 2.2 and 2.9. We describe the simulations as highly substructured ('H') when $D = 1.6$, as moderately substructured ('M') when $D = 2.2$, and as smooth ('S') when $D = 2.9$. The velocities are scaled to have a virial ratio of $\alpha_{\rm vir} = 0.3$ (cool, 'C'), 0.5 (virialized, 'V') or 0.7 (warm, 'W').

We refer to the initial conditions of a simulation by these identifying letters, e.g. 'MW' is a moderately substructured, warm region ($D = 2.2$, $\alpha_{\rm vir} = 0.7$). A summary of the simulations is shown in Table 1.

For each set of initial conditions, we run an ensemble of 50 simulations in which only the random number seed used to set the initial conditions is changed.

2.5 Cluster finding

In the Appendix, we describe our cluster-finding algorithm. This is used to distinguish bound 'clusters' within our larger regions as they evolve. It is able to determine which stars are locally bound to a particular object and which are 'halo' stars. The algorithm is not perfect and sometimes struggles when applied to regions with ambiguous or unusual morphologies. However, it allows us to avoid 'by-eye' determinations of membership when the region evolves to a distinct single or a binary cluster, which occurs in the vast majority of cases.

Downloaded from https://academic.oup.com/mnras/article-abstract/471/2/2498/3964531 by University of Sheffield user on 14 May 2019

3 THE FORMATION OF A BINARY CLUSTER

First, we will examine the process of binary cluster formation in a small set of simulations. This allows us to investigate the process in detail. Twelve MW simulations ($D = 2.2$, $\alpha_{\rm vir} = 0.7$) are chosen at random for this; binary cluster formation is fairly common in the MW ensemble, and the number 12 is chosen to produce an easily readable figure. Later, we will examine parameter space to see which initial conditions are most likely to form binary clusters.

3.1 An ensemble of moderately substructured, warm regions

In Fig. 2, we show the stellar distributions of each of the 12 regions after 20 Myr. The distributions are presented in the x–y projection in 35 pc × 35 pc boxes. All these simulations use inherited velocities (see Section 2.2).

A visual inspection of Fig. 2 shows that distinct binary clusters form in four of the 12 realizations, as shown in panels (c), (d), (g), and (i).[1]

Simulation (f) has an overdensity at coordinates roughly −2 pc, −7 pc, which could be a small companion cluster. Despite the other structure in the region and the significant halo, our cluster-finding algorithm does distinguish it as a distinct entity. We therefore define simulation (f) as a binary cluster.

Simulations (a), (b), (h), (j), (k) and (l) have evolved into single, central star clusters.

Simulation (e) has also evolved into a single cluster but is elongated. Elongated clusters are discussed later in Section 4.3.

It is important to remember that all 12 simulations had statistically the same initial conditions, only the random number seed has been changed. The wide range of morphologies apparent at the end of the simulations is not particularly surprising as the evolution of substructured initial conditions is known to be highly stochastic (Allison et al. 2010; Parker & Goodwin 2012).

3.2 Future evolution

We may naively expect binary clusters to orbit one another in the same manner as binary stars do; however, in these simulations the two clusters move directly apart and are usually unbound from each other. At the end of the simulations, two of the binaries are unbound, two are *just* unbound and one is bound. The bound binary could recombine at some point in the future. In fact, such recombinations are observed in the full ensemble of simulations and discussed in Section 4. In reality, such mergers may be less likely as the Galactic potential could shear the clusters away from each other.

Typically, the relative velocities of the clusters in our simulations are only $\sim$1 km s^{-1}, so they could remain observationally associated for many tens of Myr even if they are formally unbound.

3.3 The division of a star-forming region

We now examine how binary clusters form in more detail. In Fig. 3, we show the evolution of the region from panel (c) of Fig. 2 for the first 2 Myr of its evolution in steps of 0.4 Myr (in panel (c) of Fig. 2 the region is 20 Myr old). We identify the two clusters at 3 Myr when they are distinct, well-separated entities with our cluster-finding algorithm. Then, at each time we colour code the stars by *which cluster they will eventually be members of*: blue for the cluster on the left, red for the cluster on the right and black for unbound to either cluster. Therefore, all of the red stars in the top left panel at 0 Myr are the same stars as are coloured red in the final panel (and all panels in-between). For each star, we also plot its velocity vector (an arrow pointing from the position of the star).

It is immediately obvious from inspection of Fig. 3 that the stars from each cluster are initially very well mixed. The red and blue stars (that will end up in the right- and left-hand clusters, respectively) are each found everywhere in the region at 0 Myr. Without the colour coding (which is based on where we know they will be in the future), from the positions of the stars alone it would be (a) impossible to tell that this region would evolve into a binary cluster and (b) impossible to tell which stars would end up in which clusters. This is true for *all* the simulations in this paper.

As the region evolves, the stars that will end up in each cluster begin to separate out into two distinct sub-clusters. At 0.4 Myr, there has been some separation; while the three classes of stars are still generally mixed, clumps of just red or blue stars have begun to form. After 0.8 Myr, there has been further separation, and these clumps appear to have grown. By 1.2 Myr, the blue stars are predominantly on the left and the red stars on the right. At 1.6 Myr, the two groups of stars have formed roughly spherical shapes, but it is not until 2 Myr that clusters are well separated.

This behaviour appears to be the result of the initial velocity coherence. Inspection of Fig. 3 shows that whilst the red and blue points are initially mixed, they are not completely randomly distributed. Even at the very beginning, there are small groups of either red or blue stars with low velocity dispersion. These groups go on to merge with other groups with (usually) similar velocities. The details of the velocity structure in this particular case mean that a significant number of stars move in roughly the same two directions. In cases where the velocity structure is such that they tend to move in many different directions a single cluster is formed.

We run 50 simulations with the same input parameters as the previous set, i.e. moderately substructured and warm, but the velocities are randomized. As one would expect, all 50 of the regions evolve into single clusters. This confirms that velocity structure is necessary for a binary cluster to form.

Given the importance of velocity structure to the formation of binary clusters, it is reasonable to wonder to what extent this might be an artefact of the (somewhat unphysical) generation of velocity coherence via inheritance. To test this, we re-run the 12 simulations with coherence set-up using a different method: velocities are sampled from a turbulent velocity field (see Section 2.2). The initial spatial distributions of the simulations are unchanged.

Binary clusters form in two of these simulations (example shown in Fig. 4). In Fig. 5, we show the initial conditions of the realization that evolves into the binary cluster in Fig. 4: the blue stars are those that end up in the left-hand cluster, the red stars end up in the right-hand cluster and black stars are unbound to either cluster (cf. Fig. 3).

There is arguably less mixing in Fig. 5 than in the first panel of Fig. 3; the blue points are mostly initially close together towards the upper centre. However, without the colour coding, it is still not obvious that this part of the initial conditions will produce a separate cluster. So, as was the case in the simulations with inherited velocities, we argue that from the initial conditions (a) it is not at all obvious whether a binary cluster will be produced, and (b) it is

[1] Interestingly, in (c), (d) and (g) there are 'bridges' of stars linking the two clusters. These 'bridges' are present when viewed in 3D suggesting they are real features. Similar 'bridges' have been found in observations of binary clusters (Dieball & Grebel 1998; Dieball & Grebel 2000; Minniti et al. 2004).

Downloaded from https://academic.oup.com/mnras/article-abstract/471/2/2498/3964531 by University of Sheffield user on 14 May 2019

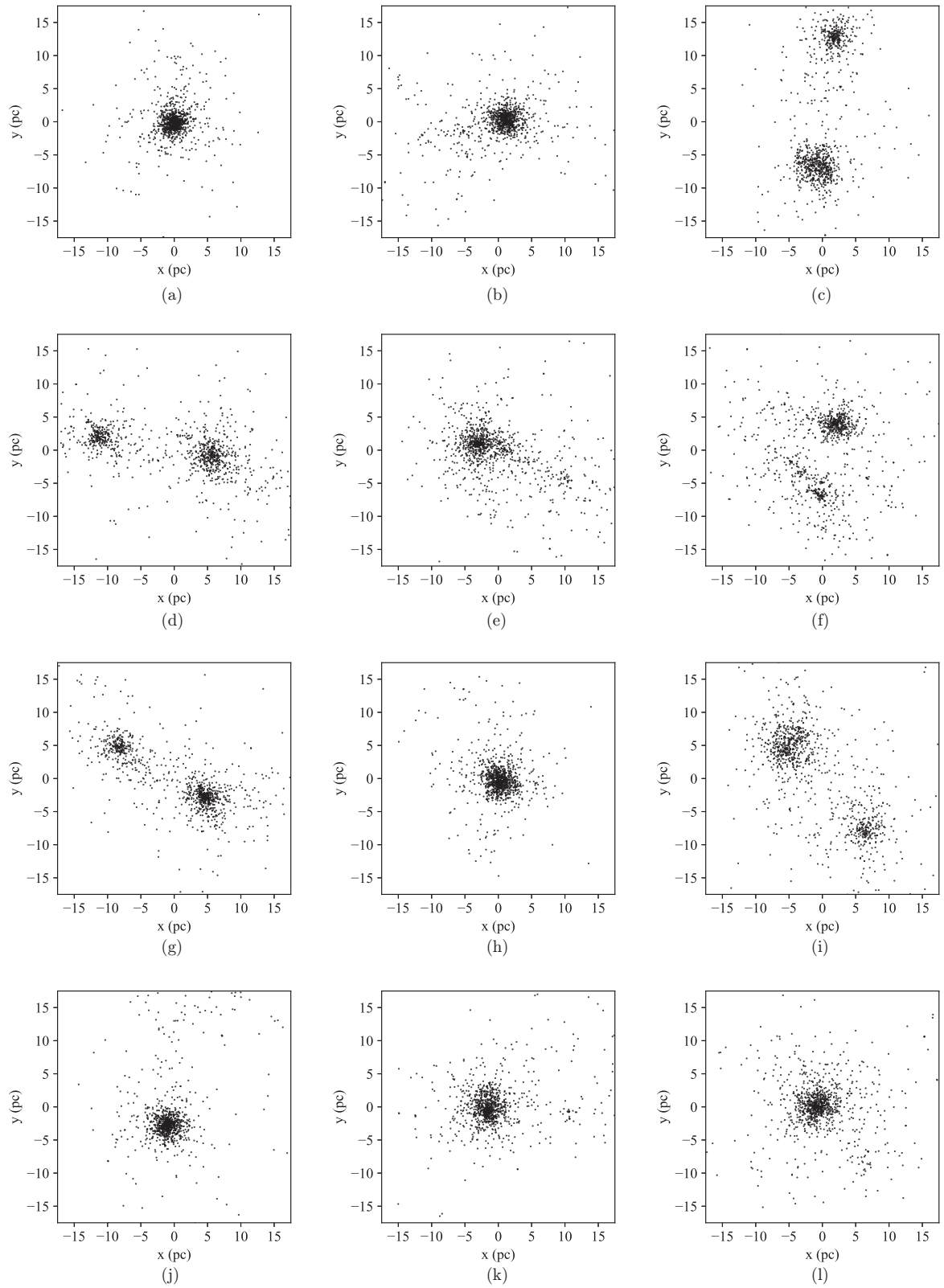

Figure 2. 35 pc × 35 pc *x*–*y* projections of 12 realizations of warm, moderately substructured initial conditions that have been evolved for 20 Myr. The only difference between realizations is the random number seed used. Every realization contains 1000 stars.

Downloaded from https://academic.oup.com/mnras/article-abstract/471/2/2498/3964531 by University of Sheffield user on 14 May 2019

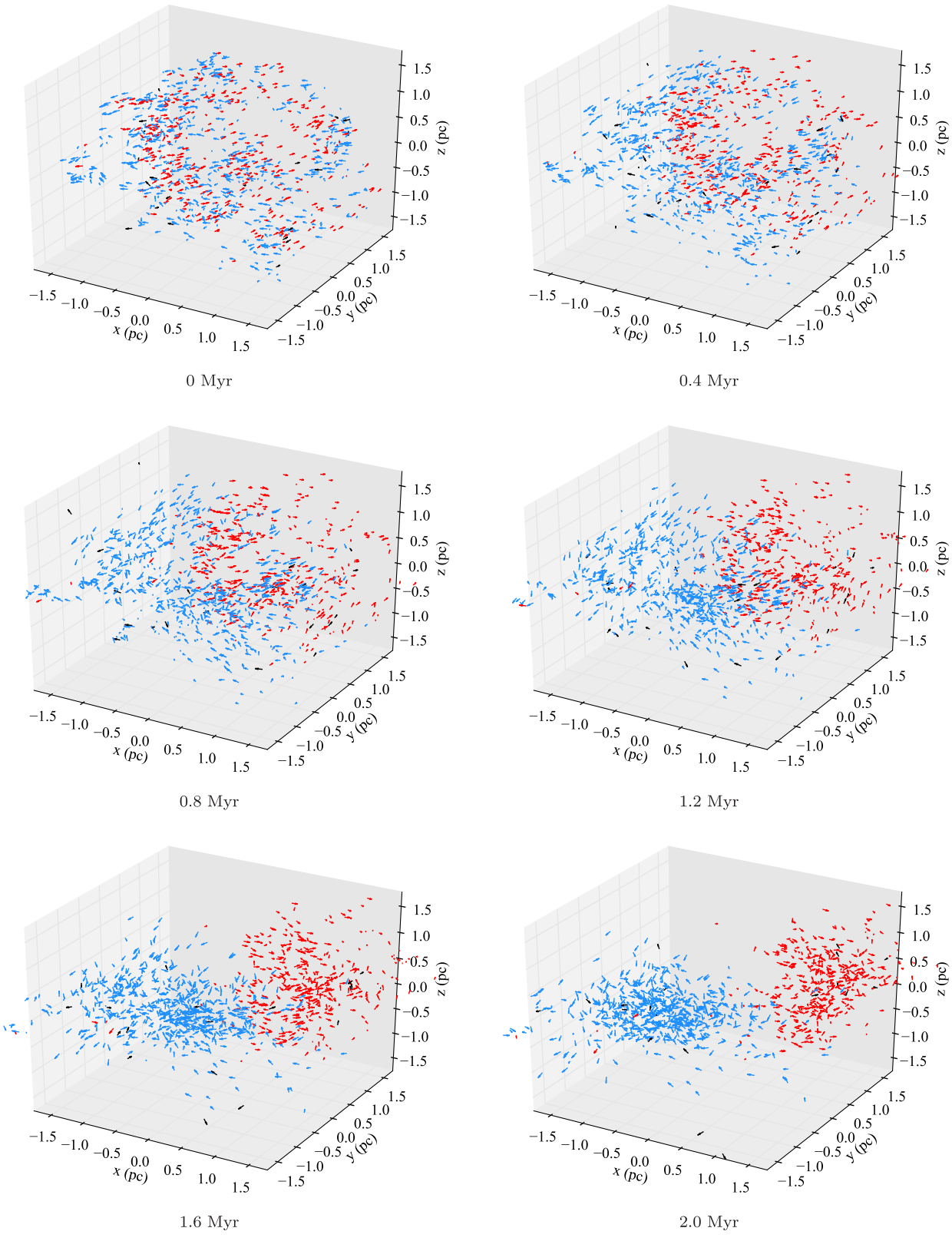

Figure 3. Snapshots at 0 Myr, 0.4 Myr, 0.8 Myr, 1.2 Myr, 1.6 Myr and 2 Myr of the simulation (c) from Fig. 2. Stars are represented by arrows plotted in 3 pc × 3 pc × 3 pc boxes. The arrow's positions indicate star's positions in space and the arrow's directions indicate the star's velocities. The arrows are colour coded: blue if the star is in the left-hand cluster after the region finishes dividing, red if it is in the right cluster after the division and black means the star is unbound.

Downloaded from https://academic.oup.com/mnras/article-abstract/471/2/2498/3964531 by University of Sheffield user on 14 May 2019

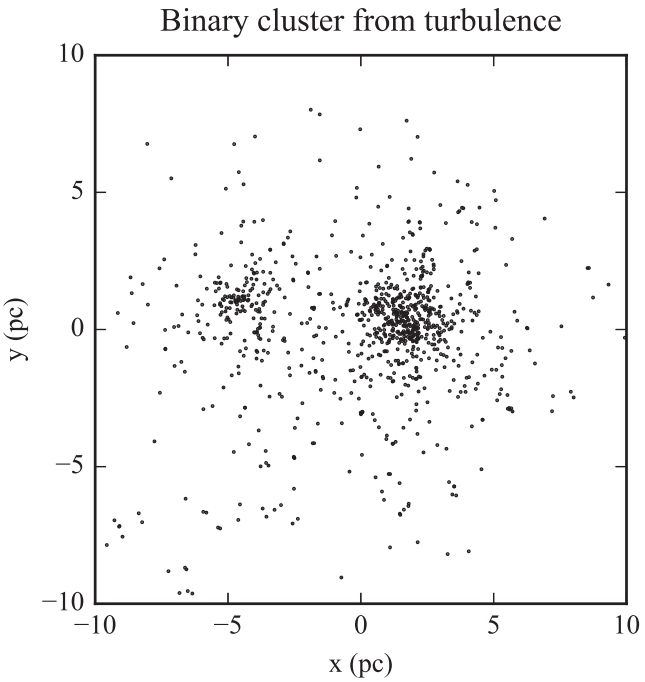

Figure 4. A 20 pc × 20 pc *x*–*y* projection of a simulation with initially turbulent velocities after 20 Myr. The region has developed into a binary cluster.

impossible to say which stars will end up in which clusters (or be unbound).

To review, binary clusters form in 2/12 simulations that use a turbulent velocity field, compared to 5/12 binary clusters from inherited velocities. This test consists of too few simulations to estimate the different rates of binary formation using each of the methods, and a detailed investigation of different methods of setting-up velocity coherence is beyond the scope of this paper. The important points here are as follows:

(1) Velocity coherence is necessary for binary clusters to form.
(2) Two independent methods are used to generate coherence and binary formation results from both. Therefore, our results are not an artefact of the method used to initialize velocity structure.

4 PARAMETER SPACE STUDY

In this section, we explore parameter space to probe which initial conditions can form binary clusters and investigate the properties of the binary clusters which form.

As described in Section 2, nine ensembles of 50 simulations are performed. The fractal dimension D is varied such that $D = 1.6$, 2.2 or 2.9 (highly substructured (H), moderately substructured (M) and smooth (S)). The virial factor $\alpha_{\rm vir}$ is varied such that $\alpha_{\rm vir} = 0.3$, 0.5 or 0.7 (cool (C), virialized (V) or warm (W)). The simulations are run for 20 Myr and are summarized in Table 1.

4.1 Which initial conditions produce binary clusters?

We classify the final state of each simulation as one of the three basic categories.

Binary clusters: Two clearly distinguished clusters as identified by the cluster finder and/or by eye. (In highly ambiguous cases when the cluster finder struggles preference is given to the by-eye conclusion.) Note that 4 of our 450 simulations develop triple clusters. For the sake of simplicity, we classify these as binary clusters.

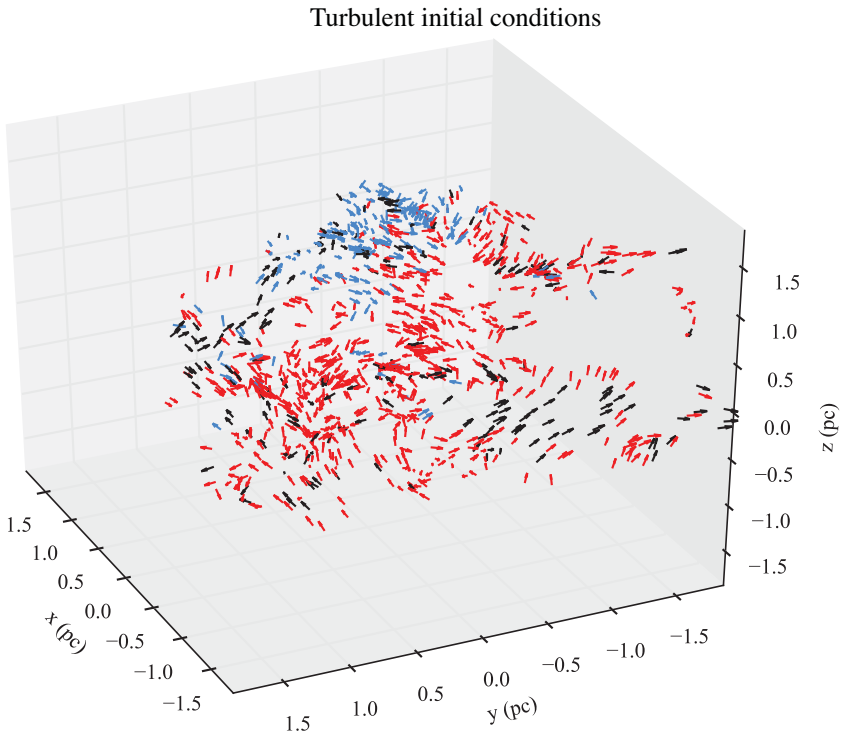

Figure 5. The initial conditions of the simulation shown in Fig. 4, which evolves into a binary cluster. Inspection of the figure clearly shows velocity coherence, which is produced by mapping the positions of the stars on to a turbulent velocity field. The colour coding is the same as described in Fig. 3.

Downloaded from https://academic.oup.com/mnras/article-abstract/471/2/2498/3964531 by University of Sheffield user on 14 May 2019

Single clusters: One significant cluster (often with an unbound 'halo' of stars).
Binary merger: A region that is a single cluster at 20 Myr but was a binary cluster at some earlier time. This may be because a binary cluster formed and then merged into a single cluster, or one of the two clusters dissolved. Therefore, depending on the time of an observation, they could be seen by an observer as a (young) binary or a single cluster.[2]

The classifications of the HV and HW simulations should be treated with some caution as their long-lived substructure makes several of them difficult to classify. Four of the 450 simulations in this parameter space study are deemed 'unclassifiable' and are omitted.

In Fig. 6, we present the fractions of regions which evolve into single, binary-merger and binary clusters. These fractions approximate the probability of each outcome, and the multinomial distribution is used to calculate to 1σ confidence where the true probability lies, which is indicated in Fig. 6 by error bars.

The top panel of Fig. 6 shows the results for the highly substructured ($D = 1.6$) ensembles with virial ratios $\alpha_{\rm vir} = 0.3$, 0.5 and 0.7 on the x-axis. The green circles are the fraction of single clusters, yellow diamonds are the fraction of binary mergers and red diamonds are the fraction of binary clusters. The middle panel of Fig. 6 is the same plot but for the moderately substructured ($D = 2.2$) ensembles, and the bottom panel is for smooth ($D = 2.9$) ensembles.

Each panel of Fig. 6 shows the same essential behaviour: binary clusters are more common as the virial ratio increases.

When the regions are dynamically cool ($\alpha_{\rm vir} = 0.3$, the left most results in each panel), almost all the simulations form a single cluster. This is as expected, as a dynamically cool distribution will collapse and erase substructure (Allison et al. 2009; Parker et al. 2014). However, the cool ensembles also produce some binary mergers; even though these regions are collapsing, velocity structure can allow them to 'divide' for some amount of time.

When regions have a moderate virial ratio ($\alpha_{\rm vir} = 0.5$, the middle results in each panel), the fraction of regions which evolves into single clusters drops, and the fraction that evolves into binary mergers increases concurrently. The exception to this is the H simulations, where both binaries and binary mergers form.

When the regions are dynamically warm ($\alpha_{\rm vir} = 0.7$, the right most results in each panel), the fraction of single clusters drops again and the fraction of binary mergers drops somewhat at all levels of substructure. In contrast, the fraction of binary clusters increases.

The main result from ensembles of different initial conditions as summarized in Fig. 6 are as follows:

(1) Higher $\alpha_{\rm vir}$ increases the probability that a region will divide.
(2) Binary clusters mainly form in dynamically warm regions.

4.2 'Micro-clusters'

Regions do not always divide into a clean binary or single clusters. In particular, the highly substructured regions ($D = 1.6$), especially with a high virial ratio ($\alpha_{\rm vir} = 0.5, 0.7$), can often form several small, bound objects that we refer to as 'micro-clusters'. Fig. 7 shows an

[2] The longest observed interlude between division and recombination of a binary merger in these simulations is ∼20 Myr. At the other extreme, some binary mergers separate so briefly they are only 'binary clusters' for ∼1 Myr.

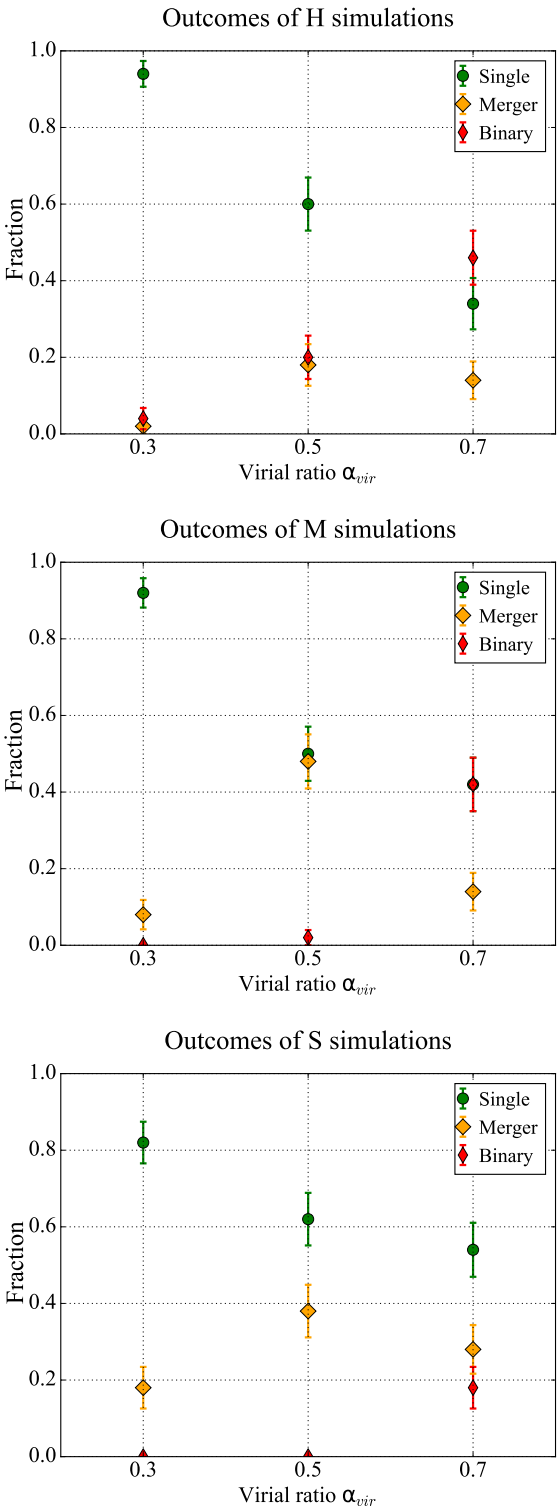

Figure 6. The fraction of regions which evolve into single, binary-merger and binary clusters for each set of simulations. The highly substructured (H) simulation results are shown in the top panel, the moderately substructured (M) simulations in the middle panel and the smooth (S) simulations in the bottom panel. The x-axis separates the simulations by their virial ratio $\alpha_{\rm vir}$ (0.3, 0.5 or 0.7). The fraction of regions in a given set of simulations which evolves into single clusters is indicated by green circles. The fraction of binary mergers is indicated by wide yellow diamonds, and the fraction of binary clusters is shown by narrow red diamonds.

Downloaded from https://academic.oup.com/mnras/article-abstract/471/2/2498/3964531 by University of Sheffield user on 14 May 2019

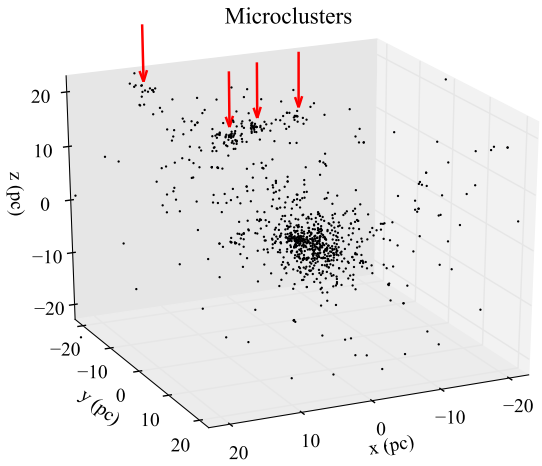

Figure 7. A highly substructured, dynamically warm region that has been evolved for 20 Myr. The star's positions are indicated by dots in a 40 pc × 40 pc × 40 pc box. The simulation has developed numerous long-lived overdensities. We call these overdensities 'micro-clusters', and they are highlighted by red arrows.

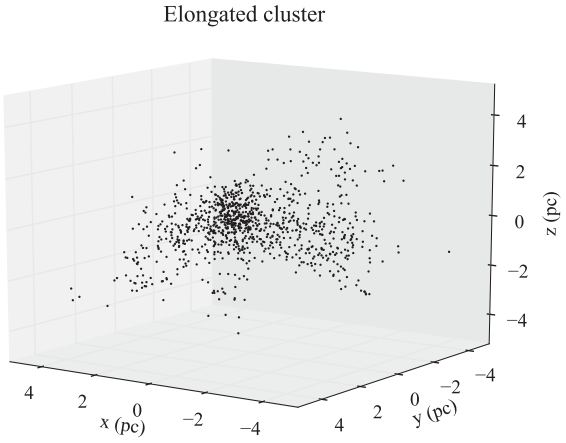

Figure 8. An initially smooth, virialized region after evolving for 3 Myr. It has developed an elongated shape that collapses back into a sphere within the next few Myr.

example of an HW simulation at 20 Myr with four micro-clusters (indicated by the red arrows).

Whilst these micro-clusters are able to survive 20 Myr, they will have short lifetimes because they only contain tens of members so their two-body relaxation time is very short. Nevertheless, they could be observed around young clusters and mistaken for independent objects instead of potential evidence that the region was initially highly substructured.

4.3 Elongated clusters

Some S regions undergo a period of elongation followed by collapse within the first ∼5 Myr. This is observed mainly in S simulations and is most common when $\alpha_{\rm vir}$ is high. An example is shown in Fig. 8.

4.4 Cluster mass ratios

We determine the mass ratios of the binary clusters (and binary mergers when they are distinct entities) using the cluster-finding algorithm. In highly ambiguous cases, where the algorithm struggles, the cluster memberships are determined by eye. This means that in some cases a *particular* mass ratio should be treated with caution. However, the trends we describe should not be affected by a small number of ambiguities. Note that we define mass ratios as the mass of the lighter cluster divided by the mass of the heavier one. Therefore, if the cluster masses are very different the mass ratio is low, and if their masses are fairly equal the mass ratio is high, with a maximum of unity.

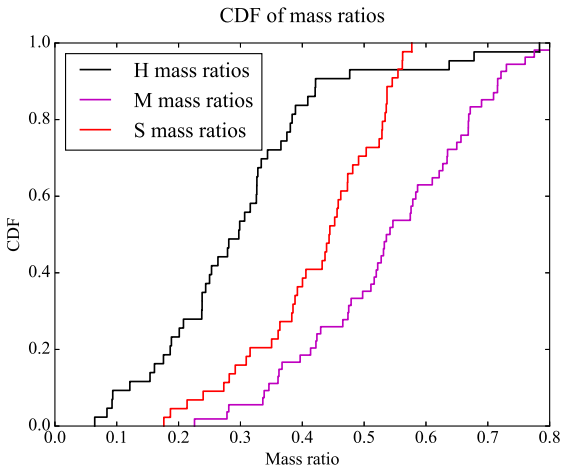

Figure 9. Cumulative distribution functions of the cluster mass ratios. The CDF for highly substructured (H) simulations is plotted by a black line, the moderately substructured (M) simulations by a magenta line and the smooth (S) simulations by a red line.

The cumulative distribution functions (CDFs) of highly substructured (H, black line), moderately substructured (M, purple line) and smooth (S, red line) binary mass ratios are shown in Fig. 9. Most binary clusters are from warm simulations ($\alpha_{\rm vir} = 0.7$) as these are the ensembles that produce the vast majority of binary clusters.

From Fig. 9, it is clear that the mass ratio distributions for each level of substructure are distinct (a KS test gives a P-value $< 10^{-4}$ for any pair of distributions, confirming that they are statistically different).

Binary clusters that form from highly substructured initial conditions (H, black line) tend to have low mass ratios (i.e. very unequal cluster masses), almost all between 0.1 and 0.4 (median 0.3).

Binary clusters that form from smooth initial conditions (S, red line) have higher mass ratios, almost all between 0.3 and 0.6 (median 0.44).

Binary clusters that form from moderately substructured initial conditions (M, purple line) have generally higher mass ratios still, ranging mostly between 0.4 and 0.8 (median 0.54).

We may have expected to see a sequence in mass ratio distributions which moves from highly substructured, to moderately substructured, to smooth. Instead, the smooth region's mass ratios are intermediate between those of the highly and moderately substructured regions.

We explain this by first considering the smooth regions (red line) as a baseline. They have no spatial structure so their mass ratios are entirely due to velocity structure.

The moderately substructured regions contain fairly large spatial structures, which themselves are correlated with the velocity structure. As a result, there are often natural 'starting points' for sizable portions of the regions to separate from the rest, resulting in more even mass ratios.

Downloaded from https://academic.oup.com/mnras/article-abstract/471/2/2498/3964531 by University of Sheffield user on 14 May 2019

In contrast, the highly substructured regions contain many small spatial structures which may divide from the main cluster, resulting in many low mass ratio systems.

4.5 Comparison with observations

Probably, the best-known binary clusters, h and χ Per, have a mass ratio of 0.76 (masses of 3700 and 2800 $M_{\odot}$, respectively (Slesnick, Hillenbrand & Massey 2002), which, from Fig. 9, suggests moderate initial substructure. However, this is only a single binary cluster, which may not be representative of the conditions that the majority binary clusters form from.

A catalogue of well-measured mass ratios could potentially provide observational clues as to the initial conditions of the regions that produce real-world binary clusters. Unfortunately, the current state of observational data cannot provide good constraints (Conrad et al. 2017). However, if more than one mechanism is responsible for binary cluster formation, the cluster mass ratio distribution would be a combination of those produced by all different mechanisms and would be much harder to interpret.

5 CONCLUSIONS

We perform ensembles of N-body simulations of $N = 1000$, $R = 2$ pc regions, which have evolved for 20 Myr. These regions start with fractal dimensions of $D = 1.6$, 2.0 or 2.9 (from highly substructured to smooth) and virial ratios (the ratio of kinetic to potential energy) of $\alpha_{\rm vir} = 0.3$, 0.5 or 0.7 (from cool to warm). The velocities of stars are 'coherent'; stars that are initially close together tend to have similar velocities.

We find that single star-forming regions can dynamically evolve into binary clusters (although this is not necessarily the only way binary clusters may form). We find that initial velocity structure is necessary for a region to divide, and in all cases it is essentially impossible to determine from the initial state of a region:

(1) If a binary cluster will form (although most of the regions that *do* form binaries are initially dynamically warm ($\alpha_{\rm vir} = 0.7$)).

(2) Which stars will end up in which component of the binary cluster.

The two clusters move directly apart from one another with relative velocities typically $\sim$1 km s^{-1}, so pairs will appear associated for tens of Myr. In some cases, the clusters remain bound to one another and recombine at a later time. We describe these as binary mergers, and they are most common in regions that begin in virial equilibrium.

We find that the level of initial spatial structure in a region strongly influences the mass ratio of a resulting binary cluster. High levels of initial substructure tend to result in very unequal masses (mass ratios 0.2–0.4), no initial spatial substructure results in slightly more equal mass ratios (0.3–0.6) and moderate substructure in even more equal mass ratios (0.4–0.8).

ACKNOWLEDGEMENTS

BA acknowledges PhD funding from the University of Sheffield and DWG from the STFC. RJP acknowledges support from the Royal Society in the form of a Dorothy Hodgkin Fellowship. Thanks also to Søren Larsen for useful discussions.

REFERENCES

Allison R. J., Goodwin S. P., Parker R. J., de Grijs R., Portegies Zwart S. F., Kouwenhoven M. B. N., 2009, ApJ, 700, L99
Allison R. J., Goodwin S. P., Parker R. J., Portegies Zwart S. F., de Grijs R., 2010, MNRAS, 407, 1098
Burkert A., Bodenheimer P., 2000, ApJ, 543, 822
Chabrier G., 2003, PASP, 115, 763
Conrad C. et al., 2017, A&A, 600, A106
De La Fuente Marcos R., de La Fuente Marcos C., 2009, A&A, 500, L13
Dieball A., Grebel E. K., 1998, A&A, 339, 773
Dieball A., Grebel E. K., 2000, A&A, 358, 897
Dieball A., Müller H., Grebel E. K., 2002, A&A, 391, 547
Elmegreen B. G., Falgarone E., 1996, ApJ, 471, 816
Fűrész G. et al., 2006, ApJ, 648, 1090
Goodwin S. P., Whitworth A. P., 2004, A&A, 413, 929
Jeffries R. D. et al., 2014, A&A, 563, A94
Kontizas E., Kontizas M., Michalitsianos A., 1993, A&A, 267, 59
Kroupa P., 2002, Science, 295, 82
Larson R. B., 1981, MNRAS, 194, 809
Lomax O., Whitworth A. P., Hubber D. A., Stamatellos D., Walch S., 2014, MNRAS, 439, 3039
Maschberger T., 2013, MNRAS, 429, 1725
Minniti D., Rejkuba M., Funes J. G., Kennicutt R. C., Jr, 2004, ApJ, 612, 215
Mucciarelli A., Origlia L., Ferraro F. R., Bellazzini M., Lanzoni B., 2012, ApJ, 746, L19
Palma T., Gramajo L. V., Clariá J. J., Lares M., Geisler D., Ahumada A. V., 2016, A&A, 586, A41
Parker R. J., Goodwin S. P., 2012, MNRAS, 424, 272
Parker R. J., Wright N. J., Goodwin S. P., Meyer M. R., 2014, MNRAS, 438, 620
Pietrzynski G., Udalski A., 2000, Acta Astron., 50, 355
Portegies Zwart S. F., Makino J., McMillan S. L. W., Hut P., 1999, A&A, 348, 117
Portegies Zwart S. F., McMillan S. L. W., Hut P., Makino J., 2001, MNRAS, 321, 199
Rozhavskii F. G., Kuz'mina V. A., Vasilevskii A. E., 1976, Astrophysics, 12, 204
Slesnick C. L., Hillenbrand L. A., Massey P., 2002, ApJ, 576, 880
Subramaniam A., Gorti U., Sagar R., Bhatt H. C., 1995, A&A, 302, 86
Tobin J. J., Hartmann L., Fűrész G., Hsu W.-H., Mateo M., 2015, AJ, 149, 119
Wright N. J., Bouy H., Drew J. E., Sarro L. M., Bertin E., Cuillandre J.-C., Barrado D., 2016, MNRAS, 460, 2593

APPENDIX: THE CLUSTER-FINDING ALGORITHM

We briefly describe how clusters are identified in a snapshot of the simulation.

(i) Step 1: Distinguish areas of high stellar density.

Space is divided into equally sized boxes by a three-dimensional grid. The resolution of this grid is initially low, and it is increased until 75 per cent of the stars are contained within at least 20 boxes. This resolution distinguishes areas of high stellar density without being too fine or coarse.

(ii) Step 2: Find the position of a cluster.

The box containing the most stars is located. By definition, clusters are regions with many stars so this box will be at, or close to, the centre of a cluster. The centre of mass and the centre of velocity of the stars in this box are calculated. The mass of stars in this box is used to crudely estimate the mass of the cluster.

(iii) Step 3: Identify cluster members.

Downloaded from https://academic.oup.com/mnras/article-abstract/471/2/2498/3964531 by University of Sheffield user on 14 May 2019

The programme goes through each star and calculates its kinetic and potential energy relative to the position, velocity and mass determined in step 2. Bound stars are identified as cluster members.

(iv) Step 4: Identify further cluster members.

The centre of mass, centre of velocity and total mass of the cluster members are calculated. Step 3 is repeated using these values, i.e. the kinetic and potential energy of each star relative to the position, velocity and mass is calculated to identify further members.

(v) Step 5: Find additional clusters.

Repeat steps 2–5. In order to prevent the same cluster being identified multiple times, stars that have already been identified as members of a cluster are excluded in step 2. Therefore, when all the clusters have been identified the box containing the most stars, as identified in step 2, contains so few stars that it could not reasonably be the centre of a new cluster. The programme stops searching for additional clusters after that point. Any remaining stars are determined to be unbound.

(vi) Step 6: Clean-up.

This step prevents the order in which the clusters are identified from influencing the final membership lists. All information on which stars belong to which cluster is thrown away; only the positions, masses and velocities of the clusters are retained. The potential and kinetic energy of each star compared to these clusters is calculated to determine which cluster (if any) the star is most strongly bound to. This produces the final membership list for each cluster. The mass, centre of mass and centre of velocity of each cluster are recalculated using this membership list.

This paper has been typeset from a TEX/LATEX file prepared by the author.

Downloaded from https://academic.oup.com/mnras/article-abstract/471/2/2498/3964531 by University of Sheffield user on 14 May 2019

Chapter 4

Quantifying velocity structure

4.1 Summary

This chapter presents 'A method to analyse velocity structure' (Arnold & Goodwin 2019). In this work a quantitative method of analysing the kinematic structure of star forming regions is presented. It is tested on a variety of datasets, and its features are demonstrated. The impact of various observational constraints on the output of the method is assessed. These constraints are:

- **i**ncomplete data due to non-observations of faint, low mass stars**;**
- **o**bservational uncertainties on measured stellar velocities **and**
- **t**he orbital velocity components of binary star systems

The method is found to be robust against all these constraints.

4.2 Description of my contribution to this work

I developed and tested this method, and wrote a piece of open source software that applies the method to a user-provided dataset. This software, VSAT, can be found at `https://github.com/r-j-arnold/VSAT`. S. Goodwin gave feedback and did some editing on drafts of this paper, however I was lead author and produced the overwhelming majority of the paper content, including all the figures.

4.3 The paper

The full published version of Arnold & Goodwin (2019) is provided below. **An addendum to footnote 4 of this paper is provided here. The median uncertainties on the velocities of individual stars with five parameter solutions at a magnitude of G = 16 is given as a guide. It is 0.096 mas yr^{-1} in the RA direction and 0.082 mas yr^{-1} in Dec.**

Monthly Notices
of the
ROYAL ASTRONOMICAL SOCIETY

MNRAS **483,** 3894–3909 (2019)
Advance Access publication 2018 December 17

doi:10.1093/mnras/sty3409

A method to analyse velocity structure

Becky Arnold★ and Simon P. Goodwin
Department of Physics and Astronomy, University of Sheffield, Sheffield S3 7RH, UK

Accepted 2018 December 11. Received 2018 December 11; in original form 2018 August 17

ABSTRACT

We present a new method of analysing and quantifying velocity structure in star-forming regions suitable for the rapidly increasing quantity and quality of stellar position–velocity data. The method can be applied to data in any number of dimensions, does not require the centre or characteristic size (e.g. radius) of the region to be determined, and can be applied to regions with any underlying density and velocity structure. We test the method on a variety of example data sets and show it is robust with realistic observational uncertainties and selection effects. This method identifies velocity structures/scales in a region, and allows a direct comparison to be made between regions.

Key words: methods: data analysis – methods: statistical – stars: formation – stars: kinematics and dynamics – open clusters and associations: general.

1 INTRODUCTION

Star-forming regions are an important part of our understanding of the Universe. Their formation and evolution has important implications for our grasp of planet formation, star formation, and stellar evolution.

In an effort to understand these regions and their evolution, several methods have been developed for quantifying aspects of their spatial structure. For example, the Q parameter (Cartwright & Whitworth 2004) describes the degree of spatial substructure in a region which aids investigations into how substructured regions evolve. The Λ (Allison et al. 2009) and Σ (Maschberger & Clarke 2011) parameters evaluate the degree of mass segregation in a region which has significant implications for our understanding of how massive stars form, how clusters form, and how clusters evolve.

Such methods of quantifying spatial structure have proved valuable and are well used, but there are not corresponding widely used methods for quantifying velocity structure. In the absence of such methods, several approaches have been used. The most basic approach is to look at the raw velocity data, often in the form of arrows overplotted on physical space, e.g. Galli et al. (2013) and Kounkel et al. (2018). This is taken further in Wright et al. (2016) and Wright & Mamajek (2018) which colour code arrows according to their direction. This approach can be helpful for getting a sense of a region's velocity structure, but does not provide an objective output that quantifies it. As a result, interpretation based on this alone is often subjective. Wright et al. (2016) and Wright & Mamajek (2018) also perform spatial correlation tests to confirm the presence of kinematic substructure in their data sets, but these tests can say little about the distribution of that substructure.

Alfaro & González (2016) present a minimum-spanning-tree-based method of quantifying kinematic substructure. This method also provides graphical indications of how this substructure is distributed. However, it is primarily designed for (and solely applied to) radial velocity data sets.

Another tool that has been used to study velocity structure is the PPV (position–position–velocity) diagram which plots stellar positions on two axes and one velocity component on a third, e.g Da Rio et al. (2017). Efforts to include extra velocity components using, for example, colour-coding or different-sized data points generally make the diagram far too complex to reasonably interpret. It is also difficult to display multidimensional errorbars. This limits the usefulness of PPV diagrams when the third spatial component and/or additional velocity components are measured.

The lack of objective, quantitative tools for studying kinematic substructure can in part be attributed to a previous absence of significant quantities of high-quality velocity data. However, the next few years will see a revolution in kinematic data for Galactic astrophysics due to *Gaia*, large multi-object spectroscopy radial velocity surveys, and longer time–baseline proper motion studies. With more and more position–velocity data becoming available, we need tools with which to analyse and interpret it.

In this paper, we introduce a new method for analysing velocity structure, borrowing from the concept of variograms (a tool used in geology), which are based on principles introduced in Krige (1951), and formalized in Matheron (1963). Here, the method is discussed in the context of analysing velocity structure in star-forming regions, but the method is extremely general and can be applied to regions of any size and morphology. This makes it well suited for objectively comparing very different regions. The method can also be applied to data sets in any number of dimensions without additional difficulty and it does not demand that the position and velocity data are in the same number of dimensions. High-dimensional data sets

★ E-mail: rjarnold1@sheffield.ac.uk

© 2018 The Author(s)
Published by Oxford University Press on behalf of the Royal Astronomical Society

Downloaded from https://academic.oup.com/mnras/article-abstract/483/3/3894/5251842 by University of Sheffield user on 14 May 2019

are often hard to visualize and apprehend, so this method aids the interpretation of such data sets (e.g. as provided by *Gaia*). Its quantative nature also makes it well suited for objectively analysing the degree of kinematic substructure in a region. Examples of data sets that this method could be applied to include Wright et al. (2016), Gagné & Faherty (2018), Franciosini et al. (2018), Kuhn et al. (2018), and Wright & Mamajek (2018).

A program called the Velocity Structure Analysis Tool, VSAT, which runs this method is available at https://github.com/r-j-arnold/VSAT.

2 THE VSAT METHOD

We outline the method below before applying it to a variety of test data sets.

In brief, for every possible pair of stars, the distance between them (Δr) is calculated along with the pairs velocity difference (Δv). Pairs are then sorted into Δr bins. In each bin, the mean Δv of the pairs it contains is calculated. These mean Δv values are then plotted against their corresponding Δr values. The values and shape of this distribution can be used to understand the velocity structure of the region and can be directly compared with those produced for any other region (i.e. they are in informative physical values of km s^{-1} and parsecs).

The method is applied twice, each using a different definition of velocity difference, Δv, which highlight different aspects of a region's velocity structure. The first definition is referred to as the magnitude definition, $\Delta v_{\rm M}$. If star i has velocity vector $\boldsymbol{v}_i$ and star j has velocity vector $\boldsymbol{v}_j$ then $\Delta v_{\rm M}$ is the magnitude of their difference, $|\,\boldsymbol{v}_i - \boldsymbol{v}_j\,|$. We stress that $\Delta v_{\rm M}$ is the *magnitude of the difference* of the star's velocities, and *not the difference of the magnitudes.* The equation to calculate $\Delta v_{\rm M}$ (assuming two dimensions for simplicity) is:

$$\Delta v_{ij\rm M} = \sqrt{(v_{xi} - v_{xj})^2 + (v_{yi} - v_{yj})^2}. \tag{1}$$

As $\Delta v_{\rm M}$ is a magnitude, it is always positive.

The other definition of Δv is referred to as the directional definition, $\Delta v_{\rm D}$. It is the rate at which the distance between the stars, Δr, is changing, i.e. it is how fast the stars are moving towards/away from one another. This value is positive if Δr is increasing (stars are moving away from each other), negative if Δr is decreasing (they are moving towards each other), and zero if they are not moving relative to each other. As such, this could be considered a measure of velocity divergence. In two dimensions, the equation to calculate $\Delta v_{\rm D}$ is:

$$\Delta v_{ij\rm D} = \frac{(x_i - x_j)(v_{xi} - v_{xj}) + (y_i - y_j)(v_{yi} - v_{yj})}{\Delta r_{ij}}. \tag{2}$$

This definition is particularly useful for investigating if a region (or structures within a region) are expanding or collapsing.

The method makes no assumptions about the underlying distribution of the star's positions or velocities and does not require the region's radius or centre to be defined. We show in Section 5 that it is relatively insensitive to even quite large observational uncertainties and biases, and works reasonably even when N is small ($<$100).

Throughout, we will assume that the data we are dealing with is 2D velocities (proper motion) and 2D positions: i.e. what would be provided by *Gaia* with good precision (and what is also simple to present in a figure). It is trivial to extend the method to full 6D information from simulations, or to add radial velocities (with a different uncertainty), or indeed any combination of spatial and velocity dimensions.

A full step-by-step explanation of the method now follows.

(i) **Calculate Δr and Δv for every possible pair of stars.**
For any pair of stars i and j, their separation Δr_{ij} is (in 2D):

$$\Delta r_{ij} = \sqrt{(x_i - x_j)^2 + (y_i - y_j)^2}. \tag{3}$$

Calculate Δv using either the magnitude or directional definition as desired. Note that as all measures are relative, the frame of reference is irrelevant (i.e. there is no need to shift into a centre-of-mass or -velocity frame).

(ii) **Calculate errors on Δv.**
If there are observational errors, propagate them to calculate $\sigma_{\Delta v_{ij}}$, the error on each Δv_{ij}. A measurement Δv_{ij} has weight

$$w_{ij} = \frac{1}{\sigma^2_{\Delta v_{ij}}}. \tag{4}$$

Observational errors on stellar positions are typically *much* smaller than on their velocities, so they are neglected in this paper.

(iii) **Sort the pairs into Δr bins.**
Each bin should contain a significant ($>>$30) number of pairings, but because the number of pairings scales as N^2 (where N is the number of stars in the data set) even fairly low N will result in a relatively large number of pairings. As long as the number of pairings in each bin is large, the bin widths have very little impact on the results (in the examples shown later, we use bins of width 0.1 parsecs and most bins contain $>$ 1000 pairs).

(iv) **For each Δr bin, calculate the mean Δv of the pairs it contains, $\Delta v(\Delta r)$.**
This gives the mean velocity difference of stars separated by a given Δr.
In the case that there are observational errors, use the weighted mean for this step. The uncertainty on this mean due to observational errors is:

$$\sigma_{\rm obs} = \sqrt{\frac{1}{\sum w_{ij}}}, \tag{5}$$

where the sum is over the pairs of stars ij in the bin.

(v) **Calculate errors due to stochasticity.**
The value of $\Delta v(\Delta r)$ calculated for each bin obviously depends on the precise positions and velocities of the stars.
However, even in 'perfect' data, there is a stochastic error due to the sampling of an underlying distribution with N points. The uncertainty due to stochasticity in each bin is the standard error of the Δv values in the bin, $\sigma_{\rm stochastic}$, which is calculated by

$$\sigma_{\rm stochastic} = \frac{\sigma_{\Delta v(\Delta r)}}{\sqrt{n_{\rm pairs}}}, \tag{6}$$

where $\sigma_{\Delta v(\Delta r)}$ is the standard deviation of the Δv values in the bin, and $n_{\rm pairs}$ is the number of pairs of stars in the bin.
If there are observational errors, then the stochastic error must use the weighted standard deviation of the Δv:

$$\sigma_{\Delta v(\Delta r)} = \sqrt{\frac{\sum w_{ij}(\Delta v_{ij} - \Delta v(\Delta r))^2}{\sum w_{ij}}}, \tag{7}$$

where the sums are over pairs ij in the bin.

(vi) **Combine the errors.**
Combine the stochastic errors with the observational errors calculated in step (iv) to get the total error on $\Delta v(\Delta r)$ in each bin:

$$\sigma_{\rm total} = \sqrt{\sigma^2_{\rm obs} + \sigma^2_{\rm stochastic}}. \tag{8}$$

Downloaded from https://academic.oup.com/mnras/article-abstract/483/3/3894/5251842 by University of Sheffield user on 14 May 2019

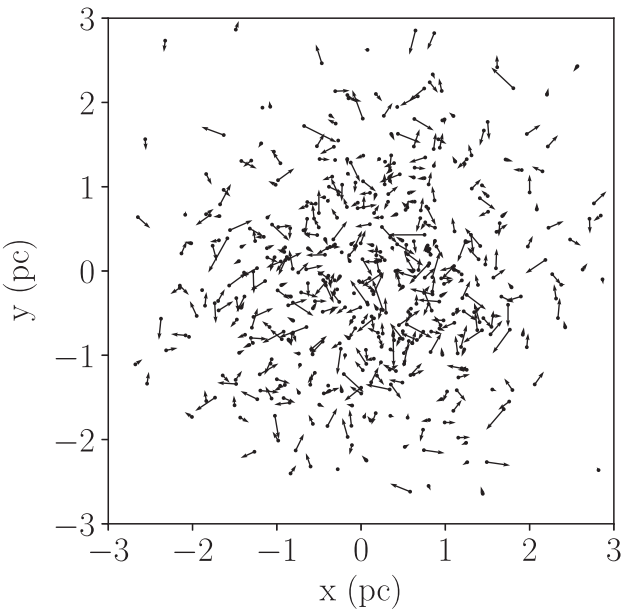

Figure 1. An artificial region with random velocities projected on to a 6 parsecs by 6 parsecs box in the *x*–*y* plane. Each star is represented by a dot with an arrow showing its velocity.

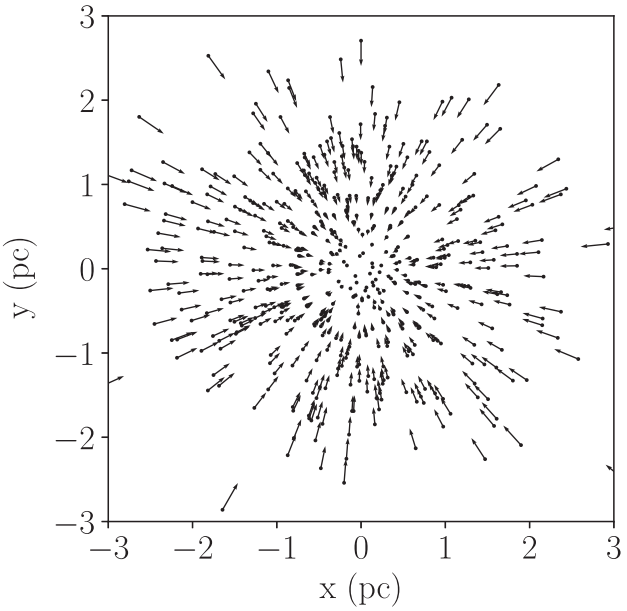

Figure 2. An artificial region projected on to a 6 parsecs by 6 parsecs box in the *x*–*y* plane. Each star is represented by a dot with an arrow showing its velocity. The velocity of each star is the negative of its position in order to produce a very simple collapsing velocity structure.

(vii) **Plot $\Delta v(\Delta r)$ with errorbars.**
Produce a plot using the magnitude definition Δv_{ijM} and the directional definition Δv_{ijD}.

As we will show, these plots contain a significant amount of quantitative and qualitative information on the spatial-velocity structure of a distribution.

To help illustrate the step by step explanation, we apply the method to two simple cases shown in Figs 1 and 2, both of which have 500 stars with Gaussian random positions. In Fig. 1, the velocities are also drawn randomly from a Gaussian, so there is no correlation between a star's position and its velocity. In Fig. 2, the star's velocities are the negative of their positions to create a 'collapsing' distribution. We provide more realistic examples later, but these suffice to illustrate the method.

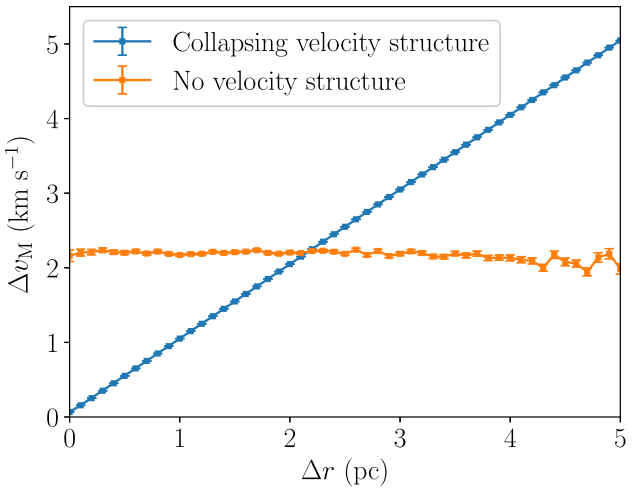

Figure 3. Physical separation, Δr, plotted against velocity difference as calculated by the magnitude definition, Δv_M, for the region shown in Fig. 1 in orange, and for the region shown in Fig. 2 in blue.

Fig. 3 shows Δv_M plotted against Δr for for the random (orange line) and simple collapsing (blue line) distributions shown in Figs 1 and 2.

The orange line is flat which shows that in the region with random velocities there is no velocity structure on any spatial scale. This is as expected as in this region there is no correlation between the distance between two stars and their velocity difference. It is worth noting that from Fig. 1 the eye can be fooled into thinking that the locations of high velocity stars are biased towards the centre. This is an artefact of there being more stars near the centre, and so there is a greater chance of a high-velocity star appearing there. This highlights the need for objective numerical methods for analysing velocity structure.

The blue line (collapsing region) is more interesting. Because the velocities in this region are the negative of the star's position, the difference in two star's velocities is directly proportional to how far apart they are. Therefore, we expect a linear relationship between Δr and Δv_M, and this is clearly visible in Fig. 3. Inspection of Fig. 2 confirms that in this region stars that are very close to one another (low Δr) have practically identical velocities, so low velocity differences Δv_M. As a result in Fig. 3, Δv_M is low at low Δr. In contrast, inspection of Fig. 2 shows that stars that are far apart (high Δr) have very different velocities (high Δv_M), which is reflected in Fig. 3.

In Fig. 4, $\Delta v_D(\Delta r)$ is plotted for the random and collapsing distributions shown in Figs 1 and 2. Recall that by this definition, negative Δv_D means the stars are moving towards one another, and positive Δv_D means the stars are moving apart.

For the random velocity distribution (orange line) $\Delta v_D(\Delta r)$ is flat, again showing no preferred scales or trends. It has a value of roughly zero showing no global expansion or contraction as expected given the velocities were drawn from a Gaussian distribution centred on zero.

The blue line (collapsing distribution) is entirely negative indicating that at all separations stars are moving towards each other.

Downloaded from https://academic.oup.com/mnras/article-abstract/483/3/3894/5251842 by University of Sheffield user on 14 May 2019

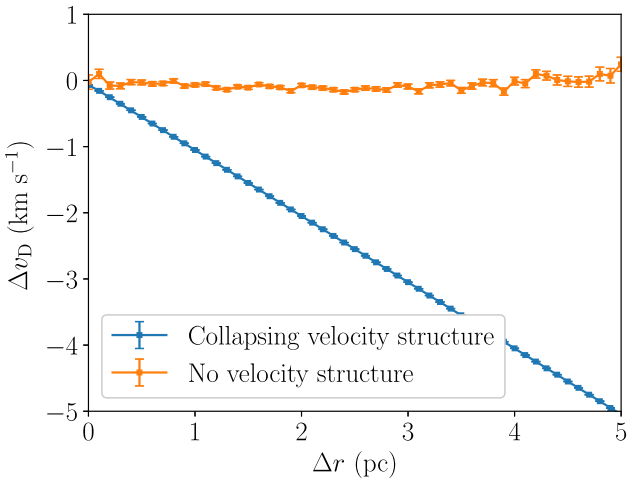

Figure 4. This plot shows physical separation, Δr, against velocity difference as calculated by the directional definition, $\Delta v_{\rm D}$, for the region shown in Fig. 1 in orange, and for the region shown in Fig. 2 in blue.

Again, given that this region is collapsing that is expected. We also see that $\Delta v_{\rm D}$ becomes more negative as Δr increases. This is because stars that are further apart are moving towards each other faster in this region.

We draw the readers' attention to the increase in the error with Δr visible in Figs 3 and 4. This is due to the decreasing number of pairs in bins with larger and larger Δr. As a result, $n_{\rm pairs}$ is low for very high Δr bins and from equation (6) the uncertainties are larger.

3 PLUMMER SPHERES

The examples used above are very simplistic. In this section, we apply the method to the more realistic case of Plummer spheres.

We generate a Plummer sphere using the method of Aarseth, Henon & Wielen (1974), with 1000 stars and a half mass radius of 2 parsecs. We scale the velocities by three different factors to produce one Plummer sphere with virial ratio $\alpha_{\rm vir} = 0.3$ (sub-virial), one with $\alpha_{\rm vir} = 0.5$ (virialized), and one with $\alpha_{\rm vir} = 0.7$ (super-virial). Here, $\alpha_{\rm vir} = T/|\Omega|$, where T is the kinetic energy, and Ω is the potential energy.

We would expect a sub-virial distribution to collapse and a super-virial distribution to expand but we have not imposed this in any way other than by scaling *all* velocities by the appropriate factor. We run an N-body simulation of each Plummer sphere for 1 Myr in order to allow them to start to adapt to the imposed virial ratios.

Fig. 5 shows $\Delta v_{\rm M}(\Delta r)$, and Fig. 6 $\Delta v_{\rm D}(\Delta r)$ for all three Plummer spheres. In both figures, the green lines are used for the $\alpha_{\rm vir} = 0.3$ Plummer sphere, orange for the $\alpha_{\rm vir} = 0.5$ Plummer sphere, and blue for the $\alpha_{\rm vir} = 0.7$ Plummer sphere.

In Fig. 5 all three lines have the same shape: large $\Delta v_{\rm M}$ at low Δr which decreases towards high Δr. The reason for this is that Plummer spheres have a high central velocity dispersion (at the deepest part of the potential) which decreases at larger radii. The majority of pairs of stars with low Δr are located in the core as, by definition, this area is dense and so contains many stars that are close together. These low Δr pairs are therefore made up of stars with a high velocity dispersion so any two star's velocity vectors are likely to be very different, and the magnitude of this difference, $\Delta v_{\rm M}$, will be large. In contrast, stars that make up high Δr pairs are predominantly located in the halo, where the velocity dispersion is smaller, so $\Delta v_{\rm M}$ is low.

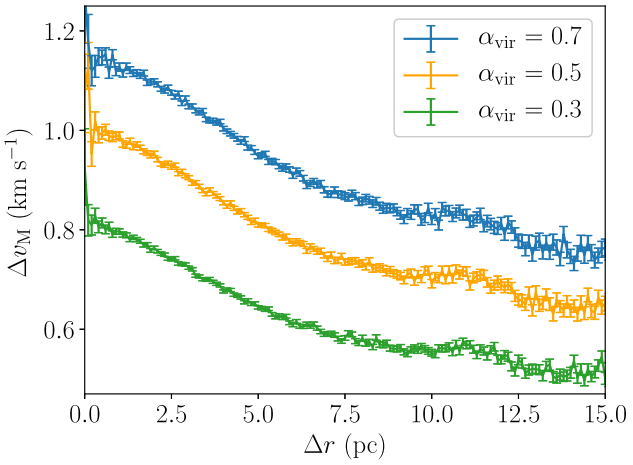

Figure 5. Plot showing $\Delta v_{\rm M}(\Delta r)$ for three Plummer spheres. The x-axis is the physical separation Δr and the y-axis is the velocity difference $\Delta v_{\rm M}$. $\Delta v_{\rm M}(\Delta r)$ of the $\alpha_{\rm vir} = 0.7$ case is shown by a blue line, the $\alpha_{\rm vir} = 0.5$ case by an orange line, and the $\alpha_{\rm vir} = 0.3$ case by a green line.

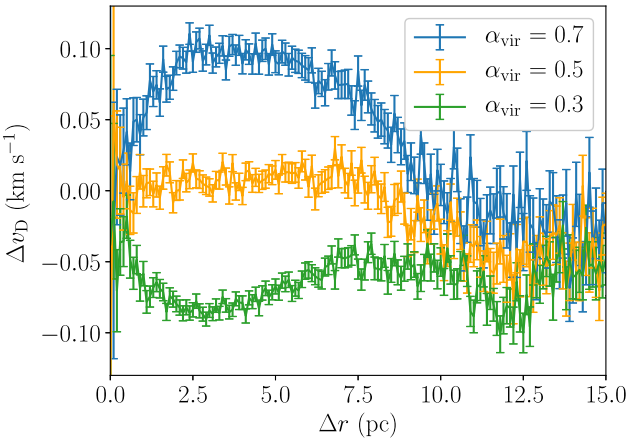

Figure 6. Plot showing $\Delta v_{\rm D}(\Delta r)$ for three Plummer spheres. The x-axis is the physical separation Δr and the y-axis is the velocity difference $\Delta v_{\rm D}$. $\Delta v_{\rm D}(\Delta r)$ of the $\alpha_{\rm vir} = 0.7$ case is shown by a blue line, the $\alpha_{\rm vir} = 0.5$ case by an orange line, and the $\alpha_{\rm vir} = 0.3$ case by a green line.

There is a clear vertical offset between Plummer spheres with higher virial ratios in this figure. This is because, as virial ratio is the ratio of kinetic to potential energies, stars in regions with high virial ratios will have higher speeds on average. Therefore, velocity differences between pairs of stars in those regions are more likely to be high.

Otherwise, the velocity structures of the three Plummer spheres are near-identical according to $\Delta v_{\rm M}$. There is a 'kink' present in all three lines at $\Delta r \sim 11$ parsecs. This is just a peculiar feature of this particular Plummer sphere realization (a similar feature is not present in Plummer spheres generated with different random number seeds).

In Fig. 6, we show $\Delta v(\Delta r)$ for each of the Plummer spheres using the directional definition $\Delta v_{\rm D}$. While in Fig. 5 all three Plummer spheres showed the same velocity structure with only a vertical offset due to their virial ratio, here the three Plummer spheres appear quite different.

Recall that positive $\Delta v_{\rm D}$ is indicative of expansion, and a negative value is indicative of collapse. The blue line ($\alpha_{\rm vir} = 0.7$) has values

Downloaded from https://academic.oup.com/mnras/article-abstract/483/3/3894/5251842 by University of Sheffield user on 14 May 2019

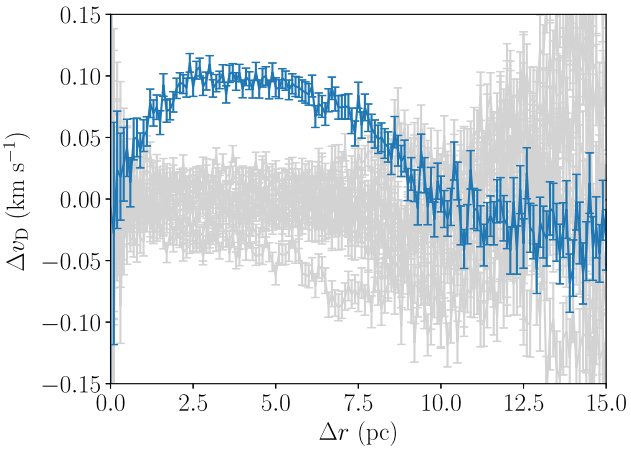

Figure 7. Plot showing $\Delta v_D(\Delta r)$ for the $\alpha_{vir} = 0.7$ Plummer sphere. The true velocity structure is shown in blue. After the velocities are randomly shuffled between stars, the recalulated velocity structure is plotted in grey. The x-axis is the physical separation Δr and the y-axis is the velocity difference Δv_D.

that are generally positive, the orange line ($\alpha_{vir} = 0.5$) is roughly flat, and the green line ($\alpha_{vir} = 0.3$) is always negative.

We examine the $\alpha_{vir} = 0.5$ Plummer sphere (orange line) first. For separations of less than 10 parsecs (i.e. separations that contain the majority of the pairs of stars), Δv_D is flat, showing that stars are equally likely to be moving towards each other as away from each other. This is as would be expected for a region that is in neither bulk expansion nor contraction. At separations above 10 parsecs, the stars are generally moving towards each other. This may be due to stars with such extreme separations being mainly found in the extreme halo of the Plummer sphere, and they are being attracted back towards the centre. As a result, they are moving towards each other on average. However, given the size of the error bars, it is also possible the apparent inconsistency of the velocity structure with zero at large separations is an artefact of stochasticity.

For the collapsing ($\alpha_{vir} = 0.3$) case, the line is below zero at every separation. That means, at every separation, on average, the stars are moving closer together.

The expanding case has positive Δv_D at separations below ∼10 parsecs; on average, stars at these separation are moving away from each other. As in the $\alpha_{vir} = 0.5$ case, stars with extreme separations are found to be moving towards one another. Again, this may be due to stars on the outskirts being attracted back towards the centre or it may due to a combination of stochasticity and large error bars at high Δr.

Uncertainty over whether a feature is real or an 'artefact' can be an issue in bins where n_{pairs} is low, as is typically the case in large Δr bins. To examine whether this feature is significant, velocities are shuffled randomly between stars which removes any real velocity structure from the data. The method is then reapplied and any 'features' observed in the result must be due to stochasticity. This is done 10 times and the results are plotted in grey in Fig. 7. The actual velocity structure is again plotted in blue for comparison.

From Fig. 7, it is is clear that any 'features' in the actual velocity stucture of the $\alpha_{vir} = 0.7$ Plummer sphere at $\Delta r >$ ∼9 parsecs are not significant. The same analysis is applied to the $\alpha_{vir} = 0.3$ and $\alpha_{vir} = 0.5$ Plummer spheres. In the $\alpha_{vir} = 0.3$ case, all features are found to be significant up to $\Delta r \sim 13$ parsecs, and in the $\alpha_{vir} = 0.5$ case, the structure is found to be consistent with the randomized cases (so no systematic expansion or contraction) at all Δrs.

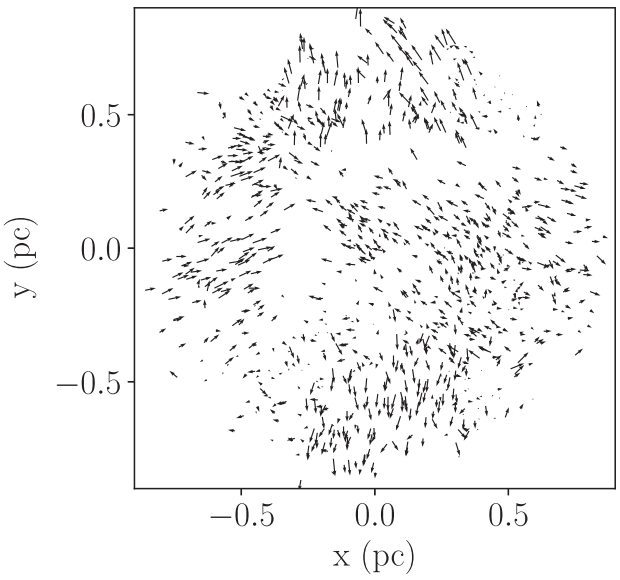

Figure 8. A distribution with low substructure generated by the box fractal method projected into a 1.8 parsec × 1.8 parsec box. Each star is represented by an arrow. The position of the arrow corresponds to the position of the star and the arrow itself indicates the star's velocity.

3.1 Interpreting observations

If an observer observed the three spherical clusters in this section, they would find them to be very similar in their spatial structure. An analysis of their velocity magnitudes Δv_M would show a structure such as in Fig. 5 and it would be possible to say that they each have a Plummer-like velocity distribution. Additionally, an analysis of $\Delta v_D(\Delta r)$ would show that one is expanding, another collapsing, and the other appears static.

4 COMPLEX SUBSTRUCTURED REGIONS

Plummer spheres are fairly simple example distributions. We now apply the method to complex substructured distributions generated by the box fractal method.

A full description of the box fractal method is available in Goodwin & Whitworth (2004); however, a brief overview is given here. A single 'parent' star is placed in the centre of a box, and then the box is divided into smaller boxes. The probability that each of these smaller boxes has of containing a 'child' star is chosen by the user. If the probability is low the fractal will have a high degree of substructure, and if the probability is large the fractal will be more smooth. If a box does contain a child star, it is placed approximately in the centre of the box (noise is added to the position to avoid an obviously gridlike structure). The velocity of the child star is the same as its parent's velocity plus some random component. After this, each child star becomes a parent and the process is repeated to produce the desired number of stars (extra stars can be deleted at random).

Note that here we are only interested in investigating the application of the VSAT method to substructured distributions, so the absolute values of e.g. radius and virial ratio are unimportant.

4.1 Distributions with low substructure

An example of a fractal with low substructure and 1000 stars is shown in Fig. 8 and the arrows show 2D velocity vectors. Clear

Downloaded from https://academic.oup.com/mnras/article-abstract/483/3/3894/5251842 by University of Sheffield user on 14 May 2019

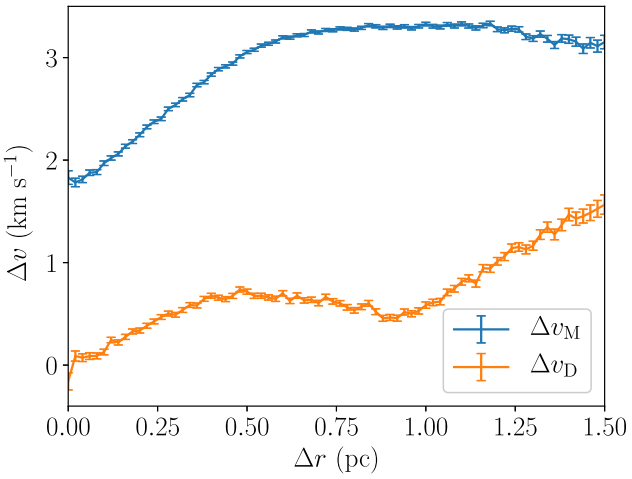

Figure 9. The velocity structure of the distribution with low substructure shown in Fig. 8. The velocity structure $\Delta v_M(\Delta r)$ is shown by a blue line and $\Delta v_D(\Delta r)$ by an orange line.

structure in both the positions and velocities of the stars is obvious, but too complex to interpret by eye in any meaningful way. It is possible to tell there is substructure, but without other information the eye could not reasonably judge the degree of velocity substructure or how it is distributed.

In Fig. 9, we show the magnitude (blue line) and directional (orange line) $\Delta v(\Delta r)$ plots for the fractal in Fig. 8 (note that everything is done in 2D).

$\Delta v_M(\Delta r)$ (blue line), is $\sim$2 km s^{-1} when the separations are low, rising to $\sim$3 km s^{-1} at separations of $\sim$0.7 parsecs and then remaining roughly constant.

This initial increase of Δv_M with Δr is because, as described above, when child stars are produced they inherit most of their velocities from their parents, plus a random component. As a result, in the completed distributions, the stars closest together have very similar velocity vectors, so the magnitude of their difference, Δv_M, is small. Stars further away from each other are very distantly 'related' so have very different velocity vectors and their Δv_M is big.

The 0.7 parsecs length scale is significant because it is the approximate radius of the distribution. Stars separated by this length scale or greater are generated from different 'child stars' of the very first generation in the production of the fractal. The random changes applied at each generation after that average to a net additional difference of zero, so Δv_M remains roughly flat at $\Delta r \geq$ 0.7 parsecs.

The directional velocity structure, $\Delta v_D(\Delta r)$ (orange line), is always positive meaning that stars tend to move away from each other on all scales. There is some structure in Δv_D showing that expansion increases on scales up to 0.5 parsecs, then is roughly even, before increasing again on scales of $>$1 parsec.

Fig. 10 shows $\Delta v_M(\Delta r)$ (top panel) and $\Delta v_D(\Delta r)$ (bottom panel) for nine distributions statistically identical to that in Fig. 8 (only the random number seed used to generate the distributions has been changed). Each distribution has the same colour in both panels.

In the top panel of Fig. 10, every distribution's velocity magnitude structure has the same basic shape: low Δv_M at small separations which increases with separation to up to around 0.7 parsecs and then is roughly flat. That said, the details of each individual line (distribution) are different, and some show 'structure' at larger scales.

In the bottom panel of Fig. 10, some distributions have predominantly negative (collapsing) Δv_D and some predominantly positive

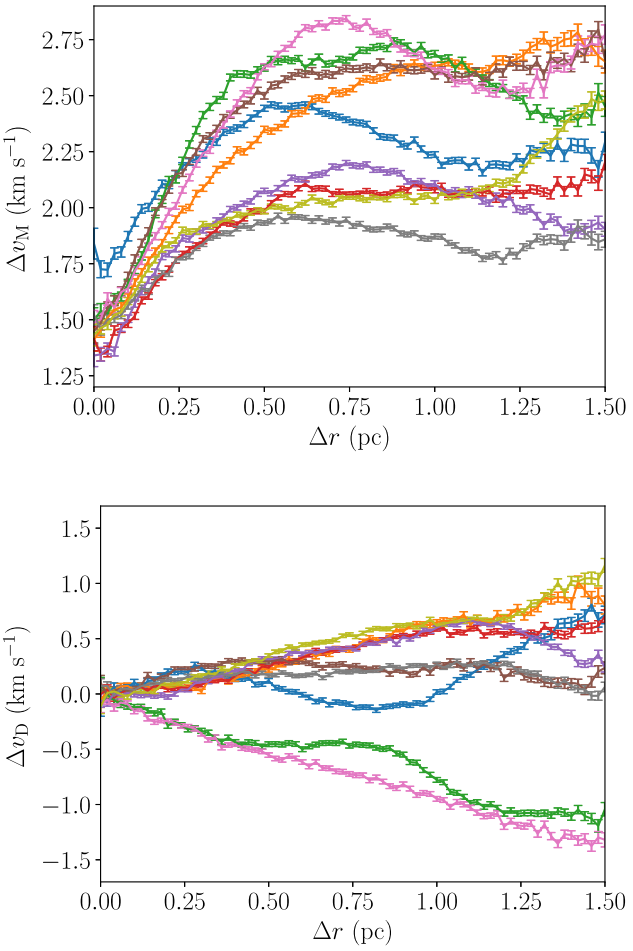

Figure 10. This figure shows $\Delta v_M(\Delta r)$ (top panel) and $\Delta v_D(\Delta r)$ (bottom panel) of nine distributions with low substructure generated by the box fractal method.

(expanding) because the box fractal method does not preferentially make either expanding or collapsing distributions. There are features visible on individual lines in this plot, reflecting that individual distributions (and parts of individual distributions) do have some velocity structure.

4.2 Highly substructured distributions

We now examine in detail a distribution with high substructure, illustrated in Fig. 11, again with arrows showing the 2D velocities. This distribution has very clear spatial and velocity structure on a variety of scales. Highly substructured distributions are produced using the box fractal method by reducing the probability of each box containing a 'child' star. The resulting distribution is less smooth as stars only continue to be generated in boxes that do have children.

The velocity structure of the highly substructured distribution from Fig. 11 is shown in Fig. 12, where $\Delta v_M(\Delta r)$ is shown by the blue line and $\Delta v_D(\Delta r)$ is shown in orange.

Broadly, the $\Delta v_M(\Delta r)$ of the highly substructured distribution has the same shape as $\Delta v_M(\Delta r)$ of the distribution with low substructure: Δv_M increases with Δr and then plateaus. However, as we would expect, in the highly substructured case, the line has additional features, including a plateau at $\sim$ 0.3 parsecs and a dip at $\Delta r >$ 1.1 parsecs. As will be shown in Fig. 14 and discussed later,

Downloaded from https://academic.oup.com/mnras/article-abstract/483/3/3894/5251842 by University of Sheffield user on 14 May 2019

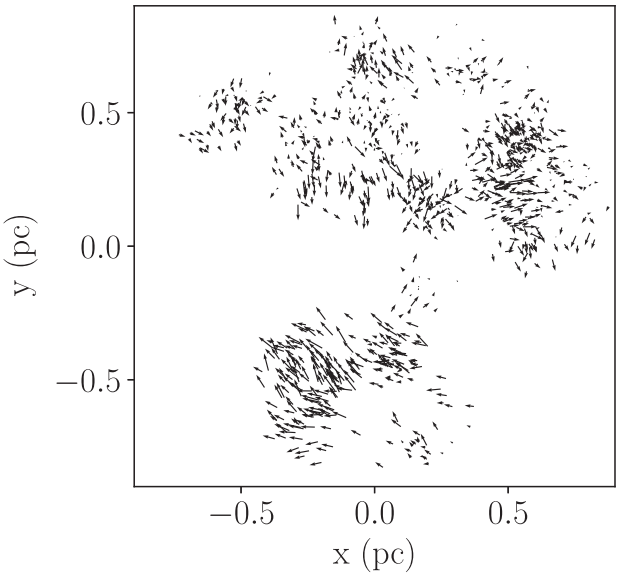

Figure 11. A highly substructured distribution generated by the box fractal method projected into a 1.8 parsec × 1.8 parsec box. Each star is represented by an arrow. The position of the arrow corresponds to the position of the star and the arrow itself indicates the star's velocity.

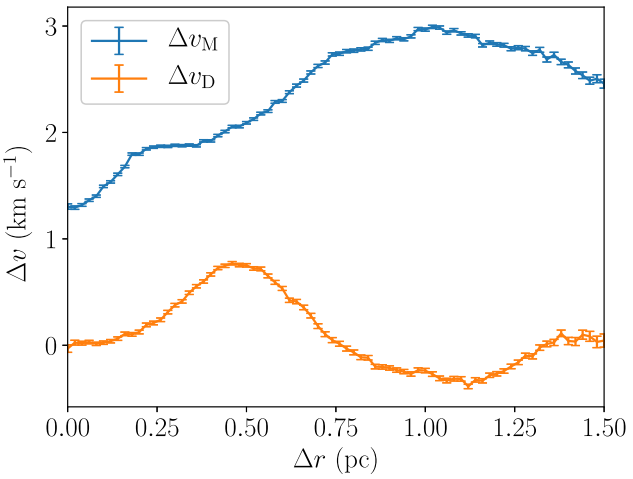

Figure 12. The velocity structure of the distribution with high substructure shown in Fig. 11. The velocity structure $\Delta v_M(\Delta r)$ is shown by a blue line and $\Delta v_D(\Delta r)$ by an orange line.

the features in $\Delta v(\Delta r)$ due to the velocity substructure are often significant in the highly substructured distributions.

The $\Delta v_D(\Delta r)$ of the distribution in Fig. 11 will now be examined in detail in order to demonstrate using the velocity structure plots to investigate the detailed dynamical structure of a region (recall that this is the orange line in Fig. 12). Inspection of this figure shows a 'peak' in Δv_D between $\Delta r \sim 0.3$ and $\Delta r \sim 0.6$ parsecs and a 'trough' in Δv_D between $\Delta r \sim 0.8$ and $\Delta r \sim 1.2$ parsecs.

To interpret these features, we can consider which stars contribute more than others in these separation ranges. For example, if a star is in densely populated area, it would be part of many low Δr pairs and would appear many times in low Δr bins. Understanding which stars are contributing most heavily to the interesting regions of the velocity structure (in this example's case 0.3–0.6 parsecs and 0.8–1.2 parsecs) helps us to understand the structure. Accordingly,

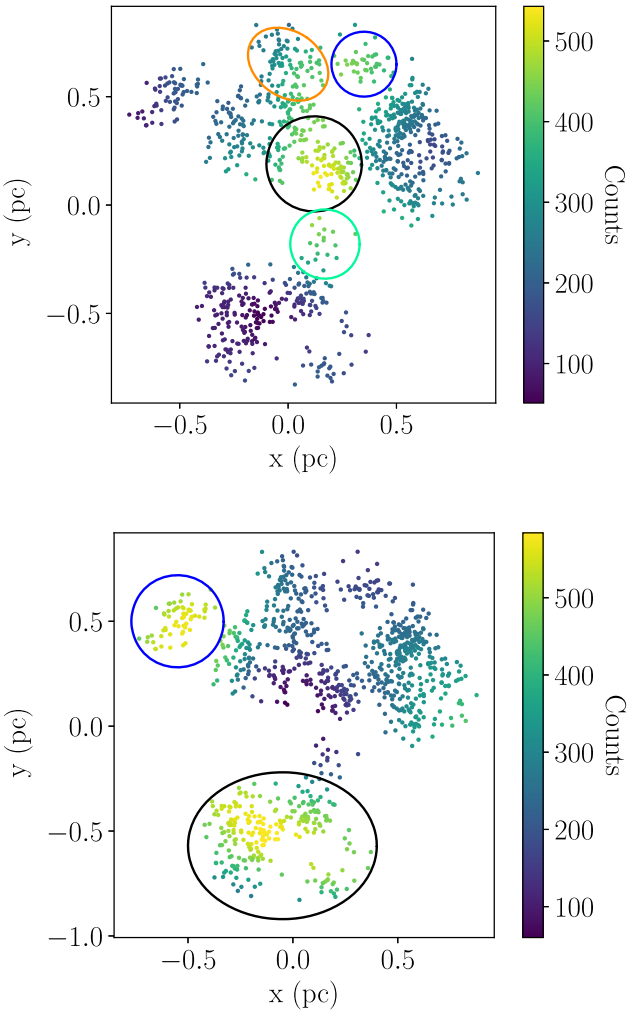

Figure 13. This figure shows the highly sustructured distribution from Fig. 11. The stars are colour-coded according to how many times they appear in Δr bins between 0.3 and 0.6 parsecs (top panel), and between 0.8 and 1.2 parsecs (bottom panel).

the number of times each star appears in Δr bins between 0.3 and 0.6 parsecs is counted. The fractal is plotted with the stars colour-coded by their counts in these bins in the top panel of Fig. 13. The same is done for the Δr bins between 0.8 and 1.2 parsecs in the bottom panel of Fig. 13.

First, we will look at the simpler case, which for this distribution is the Δr 0.8–1.2 parsecs range, where Δv_D is negative. Inspection of the bottom panel of Fig. 13 shows that two clumps contribute strongly to these bins. These clumps have been circled in blue and black on the figure for clarity. Comparison of this figure with Fig. 11 shows that these clumps are moving towards each other, therefore Δv_D is negative in this Δr range. From this analysis, we can anticipate that these clumps will continue to move towards one another (at least in the short term, and in the 2D plane we are observing – we have no idea here about the third dimension of either position or velocity).

The 0.3–0.6 parsecs range is more complicated. Inspection of the top panel of Fig. 13 shows that stars in a small clump at coordinates around (0.15, 0.15) parsecs which has been circled in black contribute most often to these bins. The stars in several surrounding

Downloaded from https://academic.oup.com/mnras/article-abstract/483/3/3894/5251842 by University of Sheffield user on 14 May 2019

clumps also contribute significantly, and these clumps have also been circled for clarity.

By comparing Fig. 11 and the top panel of Fig. 13, we see that the stars in the central clump (black circle) have a bulk motion downwards on the figure (this direction is defined as 'south' for simplicity). To the north, there are two clumps, one circled in orange which is moving to the north-west, and the other one circled in blue moving east. Therefore, these three clumps are all moving away from each other, resulting in $\Delta v_{\rm D}$ being positive. In particular, the clump circled in orange is moving directly away from the main body of the distribution. In the short term, we would expect this clump to continue to separate from the majority of the distribution (at least in this projection).

There is one other clump with stars which contribute significantly to the 0.3–0.6 parsecs Δr bins, which is in the south and circled in green. This clump is moving northeast, directly towards the central clump and the clump circled in blue (so negative $\Delta v_{\rm D}$) and away from the clump circled in orange (positive $\Delta v_{\rm D}$). Although the $\Delta v_{\rm D}$ contribution from stars in this clump is mostly negative, the number of stars it contains is small, so it is easy to explain why the mean $\Delta v_{\rm D}$ in the 0.3-0.6 parsecs Δr range is positive. It seems likely that the black- and green-circled clumps will continue to move towards each other in the short term.

In summary, with only the raw stellar positions and velocities shown in Fig. 11, the complex velocity structure of the distribution is very difficult to understand or make judgements on by eye. The method presented in this paper has been used to explore and interpret the dynamical state of this distribution and make predictions about its short-term future.

For the purpose of comparison, nine additional highly substructured regions are generated using the same method but different random number seeds. These region's velocity structures are shown in Fig. 14 where the top panel shows $\Delta v_{\rm M}(\Delta r)$ and the bottom panel $\Delta v_{\rm D}(\Delta r)$.

The first feature of note is that there is much less structure in both panels of Fig. 10 than in their corresponding panels in Fig. 14, which reflects the significant velocity substructure in this latter set of distributions. This is useful because while it is easy to distinguish the differing levels of spatial structure in Figs 8 and 11 by eye the distributions are too complex to tell simply by looking if the velocity structures are different. Therefore, even if the actual degree of velocity structure in each set of distributions were unknown, we could still say with confidence that there is significantly more velocity structure in this latter set.

We also note that in Fig. 14 each individual line in both panels appears quite different from the others. This is unsurprising as the distributions are produced using different random number seeds so each is unique, and the distributions are highly substructured so two statistically identical distributions may have very different forms .[1]

In the top panel ($\Delta v_{\rm M}$), the velocity structures show a general upwards trend; although individual structures show significant deviation from this (as was mentioned in the discussion of Fig. 12) on the whole $\Delta v_{\rm M}$ correlates positivity with Δr. This increase of $\Delta v_{\rm M}$ with Δr is a result of the box fractal generation method which produces distributions where stars that are near one another have similar velocities and stars that are far apart have very different velocities. The magnitude of the features on each line makes it difficult to say with confidence if there is a plateau at large Δr.

[1]This raises the question as to if these distributions are indeed 'the same', however, that is a discussion beyond the scope of this paper.

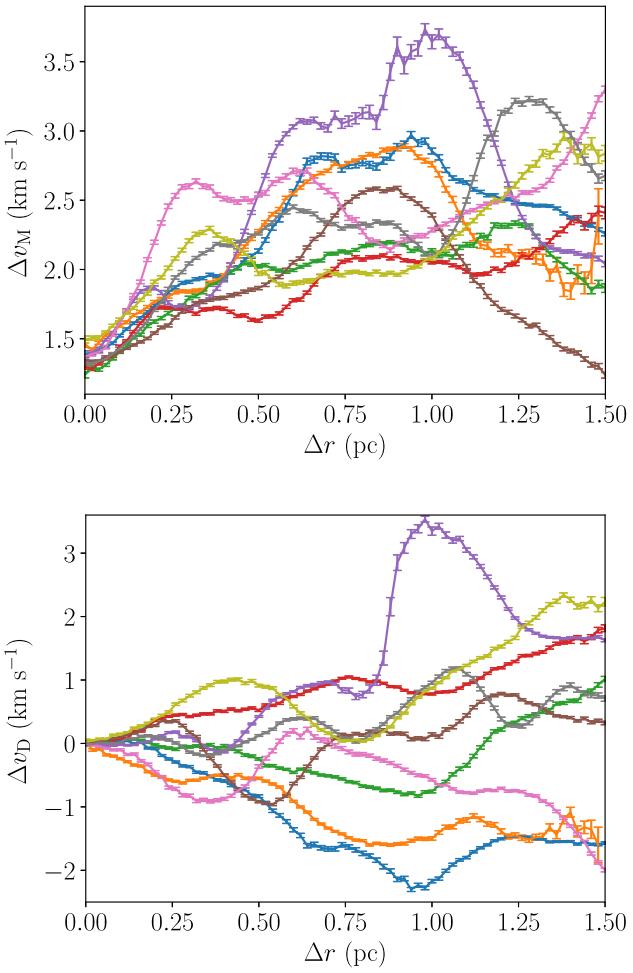

Figure 14. This figure shows the velocity structure $\Delta v_{\rm M}(\Delta r)$ (top panel) and $\Delta v_{\rm D}(\Delta r)$ (bottom panel) of nine highly substructured distributions generated by the box fractal method.

In the bottom panel, as is the case in Fig. 10, some distributions have predominantly negative $\Delta v_{\rm D}$ and some predominantly positive $\Delta v_{\rm D}$ as the box fractal method is not biased towards making either expanding or collapsing distributions.

5 INCLUDING OBSERVATIONAL UNCERTAINTIES

In this section, we test whether the method is robust when faced with imperfect data.

The velocity structure of a simulated star cluster is measured, then observational errors are applied to the data, and the velocity structure is re-calculated. The 'true' velocity structure and 'observed' velocity structure are then compared. A simulation with an unusual spatial and velocity evolution is used to make this more challenging.

The cluster is taken from Arnold et al. (2017). That paper gives all the details of the simulations, but this cluster contains $N = 1000$ stars with masses drawn from the Maschberger IMF (Maschberger 2013) using a lower limit of 0.1 $M_\odot$ and an upper limit of 50 $M_\odot$. It has been evolved for 2 Myr and has split into a binary cluster as shown in Fig. 15.

Although the results presented here concern only this cluster, the same procedure has been applied to a variety of other simulated clusters, and similar results are found.

Downloaded from https://academic.oup.com/mnras/article-abstract/483/3/3894/5251842 by University of Sheffield user on 14 May 2019

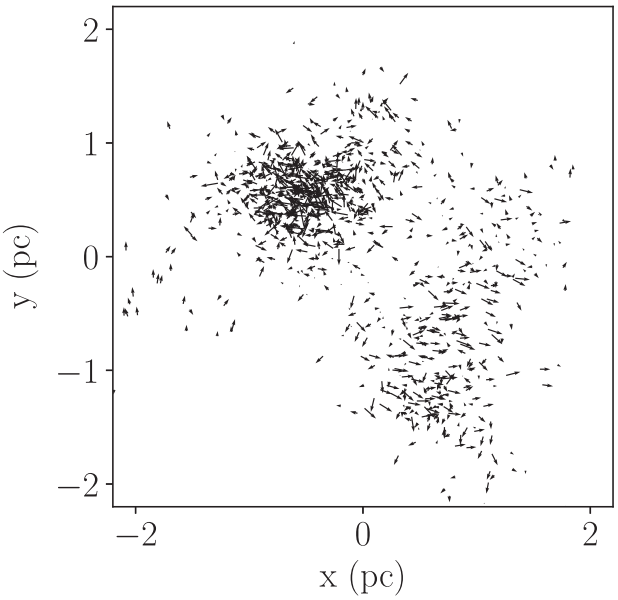

Figure 15. A cluster from a simulation with an unusual velocity evolution. Observational errors are applied to this cluster and the 'true' and 'observed' velocity structures are compared.

5.1 Velocity uncertainties

As stated in Section 2, this paper only considers errors on velocities as they are typically significantly larger than errors on positions. We also assume that all stars in the analysis are true members of the cluster. Later, we remove low-mass stars and examine the impact on the results, but do not add 'contaminants' (how important these are will vary significantly depending on the observational data set).

Observational uncertainties are simulated by replacing each star's 'true' velocity with an 'observed' velocity with an associated error. The observed velocity is drawn from a Gaussian centred on the true velocity. The width of the Gaussian used is the observational uncertainty being simulated, $\sigma_{\rm sim}$ (i.e. the true velocity usually lies within the error bar of the observed velocity). This is done for the x, y, and z components of the velocity separately, i.e. the true x velocity of a star is replaced with an observed x velocity, etc. Here, $\sigma_{\rm sim}$ values of 0, 0.4, 0.8, 1.2, and 1.6 km s^{-1} are used. The $\sigma_{\rm sim} = 0$ km s^{-1} case is the true velocity structure as there is no observational uncertainty (although it still has an uncertainty associated with stochasticity as in all previous cases).

For each $\sigma_{\rm sim}$, the observed $\Delta v_{\rm M}(\Delta r)$ and $\Delta v_{\rm D}(\Delta r)$ are calculated. These are shown in Fig. 16 where the velocity structure with $\sigma_{\rm sim} = 0$ km s^{-1} is shown by the blue line, 0.4 km s^{-1} is the orange line, 0.8 km s^{-1} is the green line, 1.2 km s^{-1} is the red line, and 1.6 km s^{-1} is the purple line.

From inspection of the top panel, it is clear that the mean $\Delta v_{\rm M}$, $\overline{\Delta v_{\rm M}}$, that is found increases with observational uncertainty from $\sim$2 km s^{-1} when there is no observational error, o $\sim$2.2 km s^{-1} when the error is $\sigma_{\rm sim} = 0.4$ km s^{-1}, and as $\sigma_{\rm sim}$ increases this trend continues.[2] The reason for this is that uncertainties in the velocities cause the velocity dispersion to be artificially inflated. As a result, the observed difference between any two velocity vectors is more likely to be larger rather than smaller than the 'true' difference.

[2]Note that this increase is not equal to $\sigma_{\rm sim}\sqrt{2}$ as may be expected.

The inflation of $\overline{\Delta v_{\rm M}}$ by observational error is not of great importance. Much of the useful information regarding the velocity structure of a cluster using the magnitude definition is contained in the shape of the $\Delta v_{\rm M}(\Delta r)$ line, not its placement on the $\Delta v_{\rm M}$-axis. Therefore, it is reasonable to analyse $\Delta v_{\rm M}(\Delta r)$ to investigate a region's velocity structure without correcting for inflation of $\overline{\Delta v_{\rm M}}$. Nevertheless, for the interested reader, the inflation of $\overline{\Delta v_{\rm M}}$ by observational error is discussed in the appendix, which also describes how this it can be corrected using Monte Carlo methods.

For the mean time, the lines are shifted such that in every case their $\overline{\Delta v_{\rm M}}$ matches that of the true velocity structure ($\sigma_{\rm sim} = 0$ km s^{-1}),[3] Fig. 17.

This figure shows a good agreement between the shape of the observed velocity structures. As the observational uncertainty increases, the observed velocity structure reproduces the true velocity structure less well, but the overall structure remains essentially recognisable even in the cases where the simulated uncertainty on each velocity component is greater than the 3D velocity dispersion of the cluster (1.53 km s^{-1}). From this, we conclude that the method deals well with observational uncertainty up to and potentially beyond the point where the errors are as large as the velocity dispersion of the region. For *Gaia,* velocity uncertainties depend largely on the apparent magnitude of the source. Table B.1 in Lindegren et al. (2018) gives median values of these uncertainties as a function of apparent magnitude for Gaia DR2. For a G-dwarf at $\sim$1 kpc, we would expect errors in proper motion of around 0.3–1 km s^{-1}.[4]

In the bottom panel of Fig. 16, we show the directional velocity structure $\Delta v_{\rm D}(\Delta r)$ (with the lines for different errors having the same colours as in the top panel). What is obvious here is that the observational errors have essentially no effect on the directional structure. This is because even with uncertainties the apparent directions of motion are usually roughly correct, and errors between pairs tend to average out rather than sum (as they did above). (Note that we assume the errors are uniform across our 'field of view', if they are not this could introduce a bias but we have not investigated this potential effect.)

5.2 Mass cutoffs

A probable bias in observations is to not observe low-mass stars as they are typically faint. (Note here that larger errors on fainter star's velocities would be included in the error propagation). We examine the effect of selection limits by removing stars of increasingly high mass from our region.

The region has 1000 stars in total which reduces to 428 stars of $>0.3\,M_{\odot}$, 207 stars of $>0.6\,M_{\odot}$, 128 stars of $>0.9\,M_{\odot}$, and only 83 stars of $>1.2\,M_{\odot}$ (these mass limits are rather arbitrary and are just chosen as examples).

Fig. 18 shows the different $\Delta v_{\rm M}(\Delta r)$ (top panel), and $\Delta v_{\rm D}(\Delta r)$ (bottom panel) plots. Different coloured lines represent different mass limits as described in the figure.

From Fig. 18, we see that the same basic velocity structure is observed at all mass limits for both $\Delta v_{\rm M}(\Delta r)$ and $\Delta v_{\rm D}(\Delta r)$. There does appear to be a sytematic increase in the amplitude of both $\Delta v_{\rm M}(\Delta r)$ and $\Delta v_{\rm D}(\Delta r)$ at high Δr and high mass cutoff. This

[3]The Monte Carlo method works well, but not perfectly. Overlaying the lines exactly allows their features to be compared more easily by eye.

[4]The random error in DR2 for G magnitudes of 15–17 is $\sim$0.06–0.2 mas yr^{-1}, however there is also a systematic error at the close angular separations we are interested in of $\sim$0.1 mas yr^{-1} (see Lindegren et al. (2018) for details).

Downloaded from https://academic.oup.com/mnras/article-abstract/483/3/3894/5251842 by University of Sheffield user on 14 May 2019

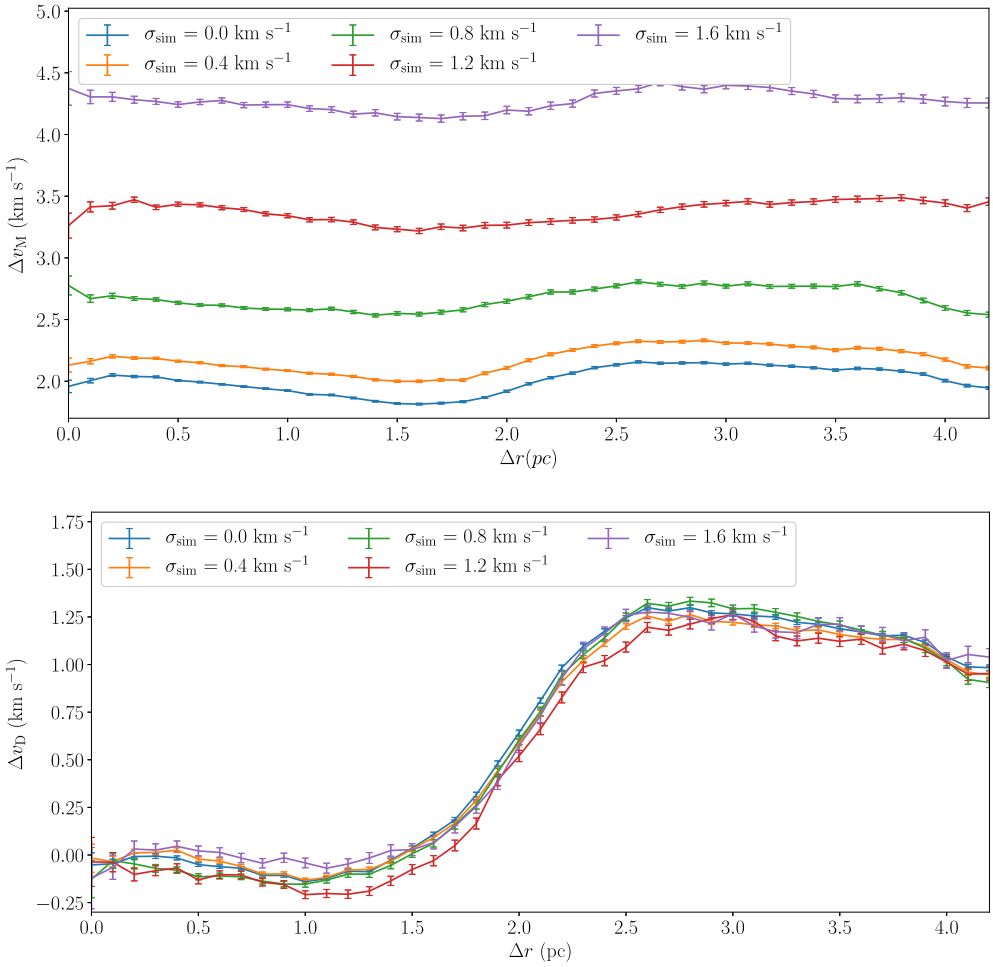

Figure 16. The velocity structure of the cluster in Fig. 15 with simulated observational uncertainties applied. The top panel shows $\Delta v_{\rm M}(\Delta r)$ and the bottom panel shows $\Delta v_{\rm D}(\Delta r)$. In both panels, a blue line is used for the true velocity structure, orange for a simulated observational uncertainty of 0.4 km s^{-1}, green for 0.8 km s^{-1}, red for 1.2 km s^{-1}, and purple for 1.6 km s^{-1}.

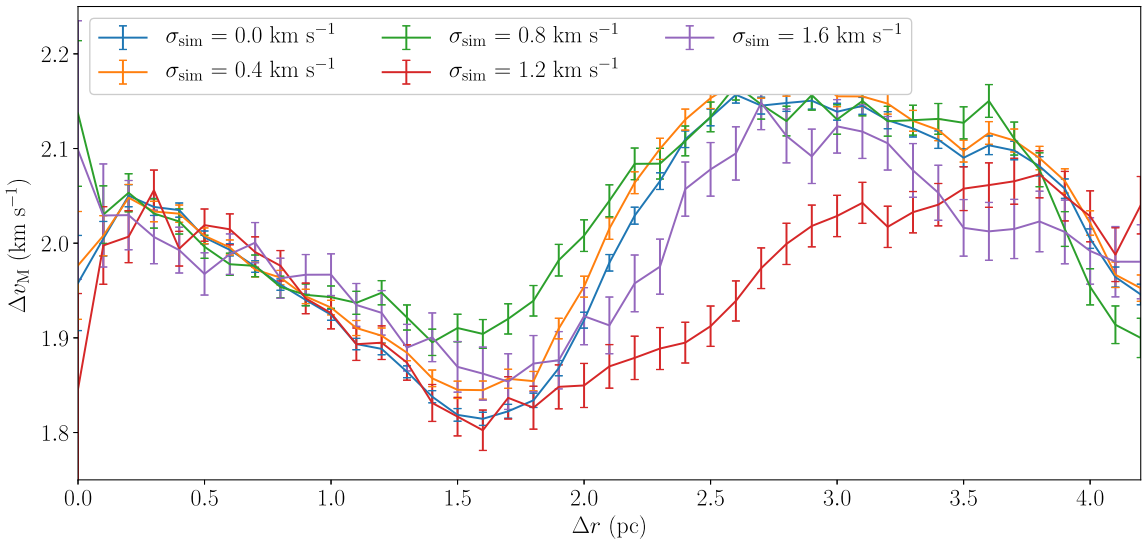

Figure 17. Top panel of Fig. 16 with each line shifted such that their $\overline{\Delta v_{\rm M}}$ matches that of the true velocity structure.

Downloaded from https://academic.oup.com/mnras/article-abstract/483/3/3894/5251842 by University of Sheffield user on 14 May 2019

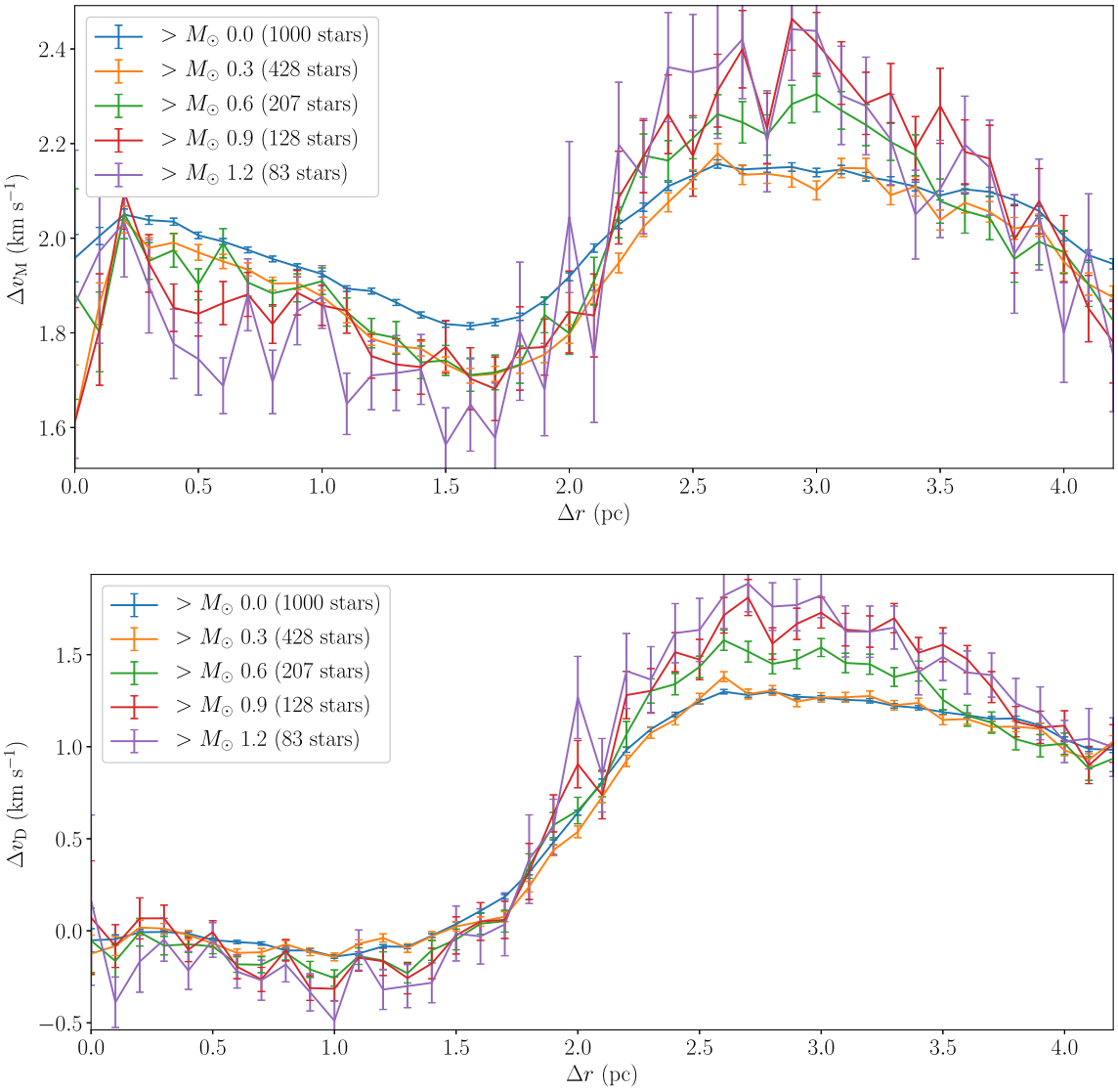

Figure 18. The velocity structure of the cluster in Fig. 15 as measured by the method using different mass cutoffs. The top panel shows $\Delta v_{\rm M}(\Delta r)$ and the bottom panel shows $\Delta v_{\rm D}(\Delta r)$. In both panels, the blue line is the result using all stars, the orange line using stars above 0.3 $M_\odot$, green uses those above 0.6 $M_\odot$, red above 0.9 $M_\odot$, and purple above 1.2 $M_\odot$.

apparent increase is not observed in other simulations from the same set. It is therefore determined to be a peculiarity of this particular simulation like the apparent 'kink' observed in Fig. 5.

The overall robustness of the measured velocity structure against mass cutoffs is encouraging, especially considering the 1.2 $M_\odot$ cutoff leaves only 83 of the cluster's original 1000 stars remaining, but it is still able to reproduce the shape of the true underlying velocity structure reasonably well.

That each of our lines for different mass limits are very similar shows that in this simulation they all trace a similar velocity 'field'. This may not be the case in reality, for example in some regions the star's spacial and velocity distributions may be a functions of mass (mass segregated regions being an obvious example).

Nevertheless, we can only measure the velocity structure of the stars which are detected, and from these tests this appears to be robust.

As the mass of the cut-off increases, the level of noise increases which is unsurprising as fewer stars survive the higher the cutoff. When there are large error bars as a result of low-*N,* the randomization approach used in Section 3 could be used to confirm which features in the observed structure are significant.

6 MULTIPLE STELLAR SYSTEMS

So far, we have assumed all stars are single. However, in observational data and more realistic simulations, many stars will be in binaries or higher-order multiples. Multiple systems, particularly those in close orbits, often have high orbital velocities. However, from the point of view of the global velocity structure of a region, a system's centre of mass velocity better describes the motion of the stars over time than their individual velocities. Here, the impact of binary systems on the velocity structure returned by the method is examined (higher order multiples are not included for the sake of simplicity).

This is done by first generating a distribution of 5000 artificial binary systems. This large number is chosen to dampen noise due

Downloaded from https://academic.oup.com/mnras/article-abstract/483/3/3894/5251842 by University of Sheffield user on 14 May 2019

to stochasticity within the distribution. As a result, fluctuations observed in the results can be confidently attributed to the impact of binary systems.

The binary systems are generated as follows. The mass of the primary star is drawn from the Maschberger IMF (Maschberger 2013). The mass ratio of the system is drawn from a uniform distribution between 0.2 and 1 (Raghavan et al. 2010) and the mass of the primary is multiplied by this factor to produce the mass of the secondary. The period, P of the system is drawn from a lognormal distribution centred on $\log P = 5.03$ with a standard deviation of 2.28 (here P is in days (d)) (Raghavan et al. 2010). From this, the semimajor axis of the system is calculated. Orbits are circular and the phase and inclination angle of the system are chosen randomly. The position and velocity of the system's centre of mass are also drawn randomly, the position from a uniform distribution within a 1 parsec $\times$ 1 parsec $\times$ 1 parsec cube, and the velocity from a Gaussian distribution with a standard deviation of 3 km s^{-1} in a random direction.

Synthetic proper motion and radial velocity measurements are then generated from this distribution. Proper motion measurements are produced by evolving the distribution forwards by 5 years (gravitational forces exerted on the systems by each other are neglected because of the shortness of this time-scale). The change in each star's position in the $x-y$ plane is used to calculate its observed proper motion. Stars's radial velocities are taken to be their instantaneous velocities in the z-direction.

In Fig. 19, we show the velocity structure of this distribution of binaries. In the left column, are the results using proper motion (2D) velocities, and in the right column are results using radial (1D) velocities velocities. The top row uses $\Delta v_{\rm M}$ for each case, and the bottom row uses $\Delta v_{\rm D}$.

In all four panels, the results using the system centre of mass velocities are shown by black lines. The centre of mass velocities more accurately describe the distribution's underlying velocity structure than the velocities of the individual stars which contain an orbital component. All four of these black lines are generally flat as expected for a random velocity field. There is a slight deviation from this at large Δr because as Δr increases fewer and fewer systems in the 1 parsec square box are sufficiently far apart to populate these bins, making them vulnerable to stochasticity (see earlier).

The other coloured lines in Fig. 19 are the velocity structure recalculated using the individual velocities of (some) stars. To model observational limitations, we remove some fraction, $f_{\rm Un}$, of the lowest-mass (hence lowest luminosity) stars. For $f_{\rm Un} = 0$ (blue lines), all primaries and companions are observed. For an unobserved fraction $f_{\rm Un} = 0.25$ (orange lines), the 25 per cent lowest-mass stars are 'unobserved' and are not included in the velocity structure calculation, and similarly for $f_{\rm Un} = 0.5$ (green lines), and $f_{\rm Un} = 0.75$ (red lines).

Note that (as described earlier) as the size of the region is 1 parsec-by-1 parsec any features on scales greater than 1 parsec should be ignored (or at least taken with extreme caution).

We also note that the results described here reflect the impact of binary stars in the worst case scenario: the binary fraction is 100 per cent, and only a single epoch of radial velocity data is used. Nine other distributions, each with 5000 binary systems, are produced and analysed as described here. Their results show the same general trends as the one presented in this paper.

We will first discuss the results using $\Delta v_{\rm M}$ (top row of Fig. 19). In both the cases, where the proper motions (left-hand panel) and the radial velocities (right-hand panel) are used, the flat shape of the centre of mass determination of $\Delta v_{\rm M}(\Delta r)$ (the black lines) is largely retained by the results using stellar velocities (coloured lines). As is to be expected, this agreement is poorer when $f_{\rm Un}$ is high (and so more stars are unobserved), and at large Δr (where bins contain fewer pairs and the impact of a small number of stars can be more important). As a result, artificial structure is visible at high $f_{\rm Un}$ and Δr. In Fig. 19, particularly in the radial velocity case, this artificial structure predominantly increases $\Delta v_{\rm M}$. In the nine other realizations of the distribution, however, there is an even spread between cases where the artificial structure increases and decreases $\Delta v_{\rm M}$.

It is clear from the figure that the results using stellar velocities are off-set to higher $\Delta v_{\rm M}$. This is due to an inflation of the 'velocity dispersion' from the extra velocity components from binary motion. The degree of the inflation is larger in the radial velocity case than the proper motion case as orbital motions, particularly in tight binaries, can add significant instantaneous component to the stellar velocity but these are somewhat 'washed out' by the time baseline of proper motion observations. As discussed in Section 5.1, the inflation of $\Delta v_{\rm M}$ has minimal impact on the interpretation of the distribution's velocity structure. Overall, the agreement between the velocity structure of the region as calculated using the centre of mass velocities, and the structure using the stellar velocities is good for all but the highest $f_{\rm Un}$ and Δr.

The bottom row of Fig. 19 shows $\Delta v_{\rm D}(\Delta r)$ using proper motions (left-hand panel) and radial velocities (right-hand panel). In both cases the directional velocity structure is extremely similar for the centres of mass (black lines), and complete or fairly complete binary samples (blue and orange lines): a flat distribution at zero $\Delta v_{\rm D}$. When half, or more, of low-mass stars are unobserved ($f_{\rm Un} = 0.5$ green line, $f_{\rm Un} = 0.75$ red line), some artificial structure appears. For most Δrs, this structure has an amplitude below 0.3 km s^{-1}, so would almost certainly be lost in the noise of real data. As in the $\Delta v_{\rm M}$ results, the artificial structure can both increase or decrease $\Delta v_{\rm D}$, and is most severe at high Δr.

For the case presented in Fig. 19, the $f_{\rm Un} = 0.5$ results using the proper motions (left panel, green line) is startlingly well behaved. This is a quirk of the binary distribution presented here; in general, there is some artificial structure in the $f_{\rm Un} = 0.5$ results. In the radial velocity results, there is more deviation, which is more typical.

It is worth reiterating that in the case of radial velocities a single epoch of observations is assumed. If there were multiple epochs, an observer could potentially estimate binary system's centre of mass velocity, even if only one star is observed. If an orbital solution cannot be found but a fluctuation in a star's radial velocity is observed, the suspected binary could be removed from the data set. This prevents contamination of the calculated velocity structure by an unknown orbital component and, as was shown in Section 5.2, the method is robust even when a high fraction of stars are not observed.

As described, there are 10 000 stars in the distribution used to produce Fig. 19 and this large N is chosen to dampen noise due to the stochasticity in the distribution (except, as discussed, at high Δr where $n_{\rm pairs}$ unavoidably becomes low). However, many observational data sets have much lower N. For comparison, the procedure described above is repeated for a distribution of 1000 stars (500 binary systems). The results are shown in Fig. 20.

The velocity structure as calculated using the system's centres of mass velocities is less flat than in Fig. 19 due to the increase in stochasticity caused by lower N. The velocity structure of the systems themselves is not of interest here however; it is the degree of agreement between it and the velocity structure calculated using the stellar velocities that is being examined.

Downloaded from https://academic.oup.com/mnras/article-abstract/483/3/3894/5251842 by University of Sheffield user on 14 May 2019

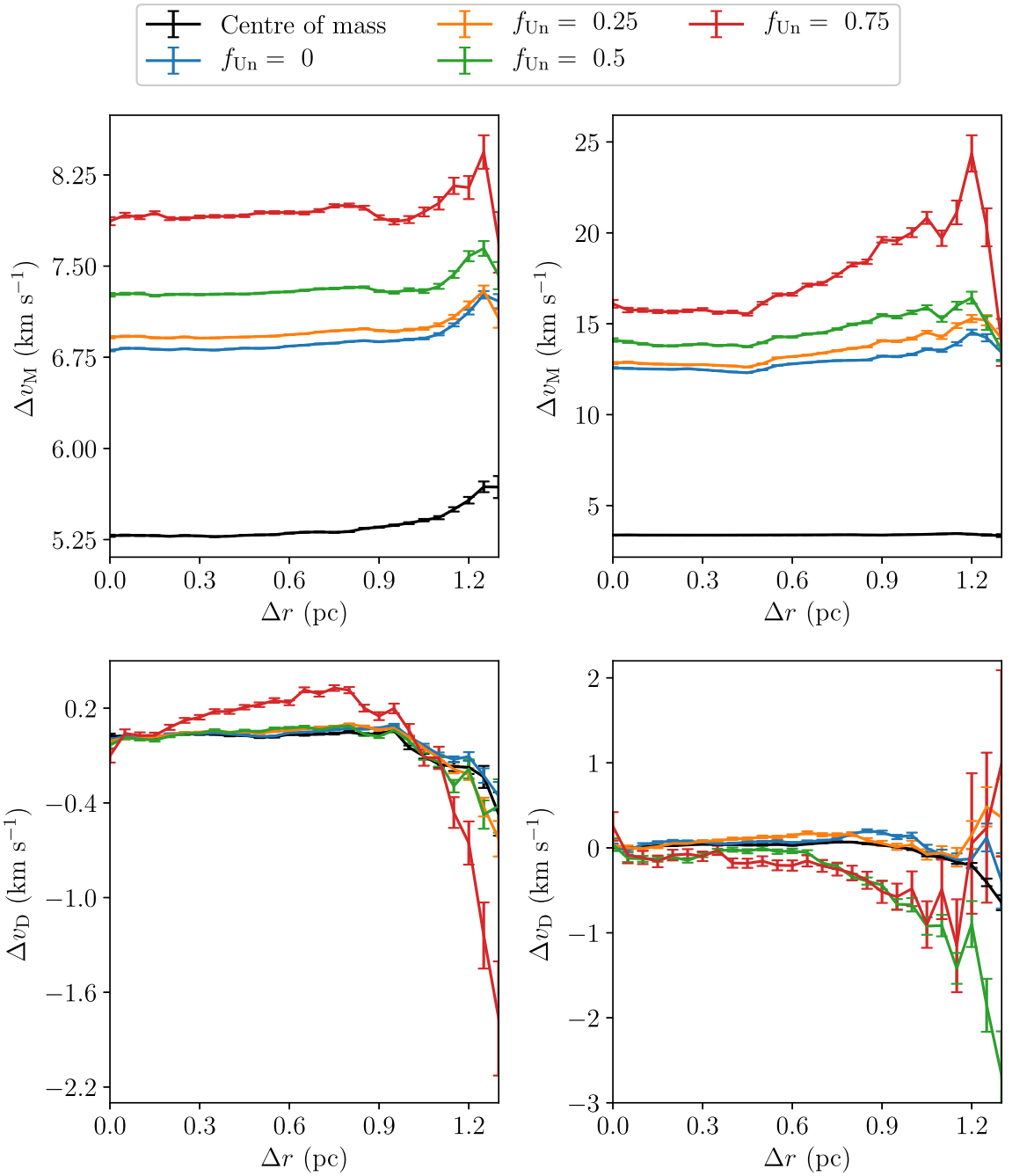

Figure 19. The velocity structure of a distribution of 5000 binary systems. The top two panels use the $\Delta v_{\rm M}$ definition and the bottom two $\Delta v_{\rm D}$. The left-hand column calculates the velocity structure using synthetic proper motion data, and the right hand one synthetic radial velocity data. In all four panels, the black lines are the velocity structure calculated using the centre of mass velocities of the binary systems. The other lines use the velocities of the individual stars. The blue lines are the velocity structure calculated when all stars in the sample are observed (the unobserved fraction $f_{\rm Un}$ is zero). The orange lines are the results when $f_{\rm Un}$ is 0.25, the green when $f_{\rm Un}$ is 0.5, and the red when $f_{\rm Un}$ is 0.75.

Inspection of Fig. 20 shows the results are noisier and have larger uncertainties than those in Fig. 19 which can be attributed to the lower N. Nevertheless, the agreement is relatively good between the results using centre of mass velocities and stellar velocities although, as was the case in Fig. 19, this becomes worse at high Δr and $f_{\rm Un}$, and there is an increase in $\Delta v_{\rm M}$ with $f_{\rm Un}$. Again, nine other distributions of 500 binary systems were generated and show the same general trends as in Fig. 20.

We now summarize the effect of binaries. Binaries 'inflate' $\Delta v_{\rm M}$ with respect to the binary centre of mass determination (exactly by how much depends on the binary population); however, the overall structure of $\Delta v_{\rm M}$ remains similar even when a significant fraction of low-mass stars are unobserved. The level and structure of $\Delta v_{\rm D}$ remains very similar, though there are deviations when the 'unobservable' fraction is very high.

What is recomforting is that the VSAT method is capable of extracting real structure from even a single epoch of radial velocity

Downloaded from https://academic.oup.com/mnras/article-abstract/483/3/3894/5251842 by University of Sheffield user on 14 May 2019

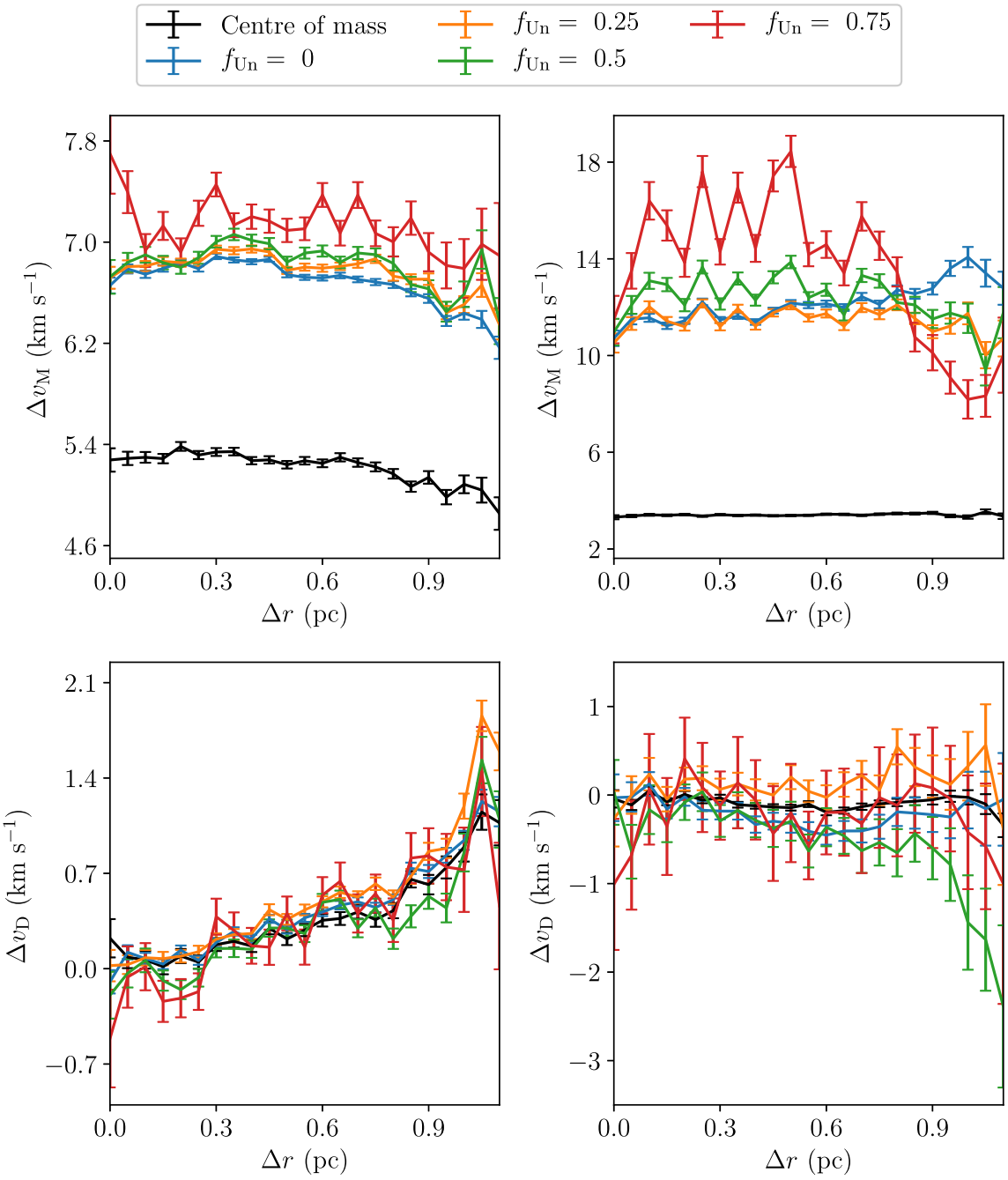

Figure 20. This figure has the same structure as Fig. 19 but it shows the velocity structure of a distribution of 500 binary systems rather than 5000. The top panels use the $\Delta v_{\rm M}$ definition and the bottom panels $\Delta v_{\rm D}$. The left column calculates the velocity structure using proper motions, and the right-hand one uses radial velocities. The black lines show the velocity structure calculated using the binary system's centre of mass velocities, and the other lines are the velocity structure as calculated using the velocities of the individual stars. The blue lines use all stars in the sample, the orange lines are the results when $f_{\rm Un}$ is 0.25, the green when $f_{\rm Un}$ is 0.5, and the red when $f_{\rm Un}$ is 0.75.

data contaminated with binary motions. Such an analysis should be treated with rather more caution than proper motion data or multi-epoch radial velocity data, but it still contains useful information.

7 CONCLUSIONS

In this paper, we present a method of examining the velocity structure of star-forming regions by plotting the physical separation of pairs of stars (Δr) against their mean velocity difference (Δv). Distributions of $\Delta v(\Delta r)$ for different regions can be directly compared to each other. Two definitions of Δv are used, the 'magnitude' definition ($\Delta v_{\rm M}$), and the 'directional' definition ($\Delta v_{\rm D}$).

This method does not require the region's centre or radius to be defined, requires no assumptions about the region's morphology, and can be applied to data in any number of dimensions in any frame of reference. The method also includes the treatment of observational errors, and is shown to be useful even for data with large errors.

Downloaded from https://academic.oup.com/mnras/article-abstract/483/3/3894/5251842 by University of Sheffield user on 14 May 2019

The output from the method requires some interpretation, and we have shown a number of examples of how to interpret more complex data. This is of particular relevance as we enter this new era of an unprecedented quantity and quality of velocity data.

Although this method was created for the purpose of investigating velocity structure in star-forming regions, it is extremely generic; there is no reason the data it is applied to must be r and v of stars. This makes it a potential tool for investigating very different data sets.

A Python program which runs the method, the Velocity Structure Analysis Tool, VSAT, can be found at https://github.com/r-j-arnold/VSAT. In the near future, we intend to publish a paper demonstrating the application of this method to observational data (Arnold et al., in preparation).

ACKNOWLEDGEMENTS

BA acknowledges PhD funding from the University of Sheffield. Thanks also to Murali Haran for useful correspondence and to Liam Grimmett and Gemma Rate for useful discussions.

REFERENCES

Aarseth S. J., Henon M., Wielen R., 1974, A&A, 37, 183
Alfaro E. J., González M., 2016, MNRAS, 456, 2900
Allison R. J., Goodwin S. P., Parker R. J., Portegies Zwart S. F., de Grijs R., Kouwenhoven M. B. N., 2009, MNRAS, 395, 1449
Arnold B., Goodwin S. P., Griffiths D. W., Parker R. J., 2017, MNRAS, 471, 2498
Cartwright A., Whitworth A. P., 2004, MNRAS, 348, 589
Da Rio N. et al., 2017, ApJ, 845, 105
Franciosini E., Sacco G. G., Jeffries R. D., Damiani F., Roccatagliata V., Fedele D., Randich S., 2018, A&A, 616, L12
Gagné J., Faherty J. K., 2018, ApJ, 862, 138
Galli P. A. B., Bertout C., Teixeira R., Ducourant C., 2013, A&A, 558, A77
Goodwin S. P., Whitworth A. P., 2004, A&A, 413, 929
Kounkel M. et al., 2018, AJ, 156, 84
Krige D. G., 1951, PhD thesis. University of Witwatersrand
Kuhn M. A., Hillenbrand L. A., Sills A., Feigelson E. D., Getman K. V., 2018, preprint (arXiv:1807.02115)
Lindegren L. et al., 2018, A&A, 616, A2
Maschberger T., 2013, MNRAS, 429, 1725
Maschberger T., Clarke C. J., 2011, MNRAS, 416, 541
Matheron G., 1963, Econ. Geol., 58, 1246
Raghavan D. et al., 2010, ApJS, 190, 1
Wright N. J., Mamajek E. E., 2018, MNRAS, 476, 381
Wright N. J., Bouy H., Drew J. E., Sarro L. M., Bertin E., Cuillandre J.-C., Barrado D., 2016, MNRAS, 460, 2593

APPENDIX: CORRECTING INFLATION

The increase in $\overline{\Delta v_{\rm M}}$ with uncertainty will now be explained in more detail. As only the magnitude definition of Δv is affected, the M subscript will be dropped to avoid overly long subscripts in this appendix.

The true velocities of stars in a region ($v_{\rm T}$) have some distribution. A cartoon, idealized picture of this is shown by a blue line in Fig. A1, where the x-axis is velocity, and the y-axis is the probability of a star having a given velocity. Due to observational uncertainties, it is impossible to perfectly measure the true velocities $v_{\rm T}$, and instead we observe velocities $v_{\rm obs}$. The effect of observational uncertainties is to smear out the true velocity distribution. The observed velocity distribution is shown by the orange line in Fig. A1 for our cartoon case. Notice that the observed velocity distribution is wider that the true velocity distribution.

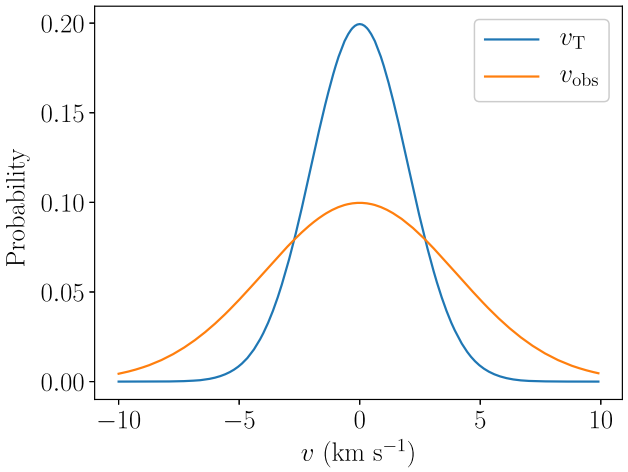

Figure A1. Cartoon depicting the broadening of the observed velocity distribution due to observational uncertainties. The x-axis shows a range of velocities and the y-axis their probability. A true velocity distribution (in blue) is broadened into the observed velocity distribution (in orange).

When the velocity difference between two stars in a region is measured this can be thought of as drawing two velocities from the velocity distribution and calculating the difference between them. If the distribution is narrow, then the range of likely velocities is small so the two velocities drawn will usually have a small difference between them, therefore $\overline{\Delta v}$ will be small. In contrast, if the distribution is wide it is more likely that any two values drawn will be very different, so $\overline{\Delta v}$ will be large. As discussed, the observed velocity distribution is wider than the true velocity distribution, so the observed mean velocity difference between pairs of stars ($\overline{\Delta v_{\rm obs}}$) is larger than the true mean velocity difference between pairs of stars ($\overline{\Delta v_{\rm T}}$). Because the width of the $v_{\rm obs}$ distribution increases with uncertainty, so does $\overline{\Delta v_{\rm obs}}$. This is why in the top panel of Fig. 16 there is a positive correlation between $\overline{\Delta v}$ and $\sigma_{\rm sim}$.

As discussed above, observational errors broaden the observed velocity distribution, so the true velocity distribution can be crudely approximated by a narrower version of the observed velocity distribution. In brief, the observed velocity distribution is narrowed by different amounts and Monte Carlo methods are used to find which width best reproduces the observed velocity distribution once observational errors are applied. Many velocities are then drawn from this best-fitting distribution, and $\overline{\Delta v}$ is calculated. This is the estimated value of $\overline{\Delta v_{\rm T}}$ given the observed velocities and the errors.

The exact method used will now be described in more detail. Diagrams shown in Fig. A2 are referred to to aid this description. For both of these plots the x-axis is velocity, and the y-axis is probability. They show how the method would be applied to some cartoon non-Gaussian velocity distribution (the black line in the left-hand panel of Fig. A2).

First a Gaussian kernel is applied to the observed velocities to produce a probability density function (pdf) of the observed velocities (red line in both panels of Fig. A2). It is assumed that the true velocities pdf is the same shape, but narrower. How much narrower is unknown, and though it can be analytically calculated if the distributions are Gaussian that will often not be the case. Instead, many different widths are tested, each model being a 'guess' at the true velocity structure. To prevent Fig. A2 becoming overcrowded, only three models are shown (blue dashed lines). In this diagram, it is

Downloaded from https://academic.oup.com/mnras/article-abstract/483/3/3894/5251842 by University of Sheffield user on 14 May 2019

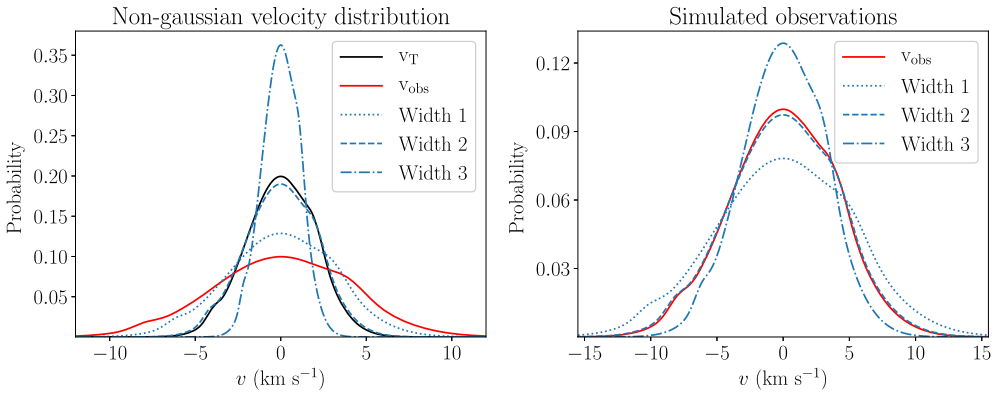

Figure A2. Diagrams aiding the explanation of how to correct for $\overline{\Delta v}$ inflation by observational uncertainties. For both the left-hand and right-hand panels, the *x*-axis is velocity and the *y*-axis is probability. The left-hand panel depicts a true velocity distribution (black line), the observed velocity distribution (red line) and three models of the true non-Gaussian velocity distribution using different widths (blue dashed lines). The right-hand panel shows the observed velocity distribution (red line), and the simulated observations assuming each of the models from the left-hand panel (blue dashed lines).

obvious that the first is much wider than the $v_{\rm T}$ distribution, the second is almost exactly right, and the third is much narrower. In reality $v_{\rm T}$ would be unknown, so it is not so easy to compare.

For each model, N velocities are drawn and observational uncertainties are applied as per the method described earlier in this section. The distributions of these simulated velocity observations are what we would expect to observe if the model were the true distribution. This is repeated many times (100 in this paper) in order to obtain reliable results. The right-hand panel of Fig. A2 shows how these simulated observational distributions compare to the actual observed distribution. If the model the velocities are drawn from is a good match for the true velocity distribution, then the simulated observations distribution will replicate the actually observed distribution well. From the left-hand panel of Fig. A2, it is evident that width 1 is too large, width 2 is approximately correct, and width 3 too narrow, and this is reflected in the right-hand panel. Clearly, the simulated observations using width 2 is the best match to the observations, and so is taken to be a good approximation of the true velocity structure.

Now that the true velocity distribution has been modelled, a large number of velocities are drawn from it and $\overline{\Delta v}$ is calculated. This $\overline{\Delta v}$ is the estimated value of $\overline{\Delta v_{\rm T}}$.

To quantify how accurate this is, the method is applied to five very different simulated regions, A, B, C, D, and E. For each, the true $\overline{\Delta v_{\rm T}}$ is calculated, then observational uncertainties are applied, and the Monte Carlo method is used to estimate $\overline{\Delta v_{\rm T}}$ from the observed velocities. This is done for observational uncertainties ($\sigma_{\rm sim}$) between 0.1 and 1.6 km s^{-1} in steps of 0.1 km s^{-1}. In each case, the difference between the true $\overline{\Delta v_{\rm T}}$ and the value of $\overline{\Delta v_{\rm T}}$ estimated using the Monte Carlo method is computed. This difference is referred to as the inaccuracy. For each of the five simulations, inaccuracy is plotted against $\sigma_{\rm sim}$, which is shown in Fig. A3.

From Fig. A3, we see a rough correlation between $\sigma_{\rm sim}$ and inaccuracy, which is expected. More importantly, we see that the inaccuracy observed is low, typically $\lesssim$0.1 km s^{-1} except for extremely high uncertainties. We therefore conclude that $\overline{\Delta v_{\rm T}}$ can be recovered from the observed velocities with reasonably high accuracy. Unfortunately, exact error limits can't be calculated because error is introduced by the assumption that the true velocity distribution has the exact same shape as the observed velocity distribution, it is only narrower. This assumption will never be perfectly true but only close, and without knowing the true velocity structure it is impossible to know how close. Therefore, the error can't be quantified.

Nevertheless, it has been shown this method can reproduce $\overline{\Delta v_{\rm T}}$ with reasonable accuracy if the errors on the velocity measurements are not too high. Also, as stated earlier, $\overline{\Delta v_{\rm T}}$ is largely irrelevant to interpretation of the velocity structure when $\Delta v_{\rm M}$ is used, it is the shape which contains the majority of the information.

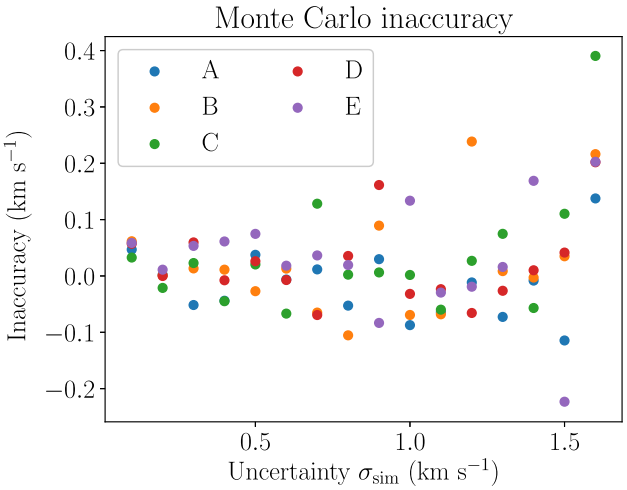

Figure A3. Plot showing the inaccuracy of the value of $\overline{\Delta v_{\rm T}}$ estimated using the Monte Carlo method. The *x*-axis is the observational uncertainty applied to the data and the *y*-axis is the inaccuracy. Different colours are used for each of the five simulations tested.

This paper has been typeset from a TEX/LATEX file prepared by the author.

Downloaded from https://academic.oup.com/mnras/article-abstract/483/3/3894/5251842 by University of Sheffield user on 14 May 2019

4.4 Comparison to similar statistics

As stated in the paper the method presented in this chapter has similarities with variograms (Matheron 1963), which are mathematically equivalent to structure functions (Simonetti et al. 1985). The difference lies in the fact the method presented here looks at the variation in the mean of the difference of some statistic (in this case velocity) at different scales, whereas structure functions look at the mean of the square of the difference. For the method presented here squaring would be counterproductive as in some cases velocity difference can be negative as well as positive, so taking the square would reduce the method's utility.

The calculation of meaningful errors for both the method presented here and for structure functions presents a mathematical challenge. The number of possible pairs from N stars (or other kind of datapoint) is proportional to N^2; so clearly the differences for all the pairs are not a collection of independent measurements. This counter to what is assumed by most common error calculation methods. As such we take a two-pronged approach to evaluating errors on this method. The first uses conventional mathematical approaches despite these issues, and the resulting uncertainties can be taken as a lower limit on the true uncertainties. The second randomly shuffles velocities between stars to remove any true structure, and re-applies the method. This is done multiple times to give an idea of the magnitude of apparent structure that may be 'measured' even when no true structure is present. Structure in the unshuffled data that exceeds these bounds is judged to be significant.

Another mathematical challenge both this method and structure functions share is reduced reliability at large scales of whatever property is being measured (whether it is time, distance, or something else entirely) where the number of pairs to take the average over becomes small. See Collier & Peterson (2001) and Emmanoulopoulos et al. (2010) for a discussion of this relating to time series data. Because of this when using the method presented in this chapter results at large separations should be treated with caution.

Chapter 5

The velocity structure of Cygnus OB2

5.1 Summary

This chapter presents the paper 'The velocity structure of Cygnus OB2' (Arnold et al. 2019; submitted). This method applies the VSAT method presented in Arnold & Goodwin (2019) to observational data of the central part of the Cygnus OB2 star forming region. The dataset is first presented in Wright et al. (2010). Using the VSAT method the velocity structure of the region is analysed. No evidence of systematic expansion or contraction is found at any scale. Velocity structure is found on scales smaller than 0.5 parsecs; on average stars closer **than** this to each other have more similar velocity vectors than stars **at larger separations**. At larger scales we find the velocity structure is consistent with a random velocity field. The implications of these results are then discussed.

5.2 Description of my contribution to this work

I performed a preliminary analysis of the dataset, which was provided by N. Wright, and removed stars that were likely not representative of the velocity structure of the region. I then applied the VSAT method to the revised dataset and analysed the results. This analysis was aided by conversations and ideas from S. Goodwin. I produced all figures in the paper aside from Fig. 1, and wrote the majority of the text aside from that in the discussion and conclusions and a small part of the methods section. Feedback was provided by S. Goodwin and N. Wright, and was used to revise the text.

5.3 The paper

The submitted version of this paper is presented below.

MNRAS 000, 1–6 (2019) Preprint 13 January 2020 Compiled using MNRAS LATEX style file v3.0

The velocity structure of Cygnus OB2

Becky Arnold,[1]★ Simon P. Goodwin[1] and Nick J. Wright[2]
[1]Department of Physics and Astronomy, University of Sheffield, Sheffield S3 7RH, UK
[2]Astrophysics Group, Keele University, Keele, Staffordshire, ST5 5BG, UK

Accepted XXX. Received YYY; in original form ZZZ

ABSTRACT
The kinematic structure of the Cygnus OB2 association is investigated. No evidence of systematic expansion or contraction is found at any scale within the region. Stars that are within ~ 0.5 parsecs of one another are found to have more similar velocities than would be expected by random chance, and so it is concluded that velocity substructure exists on these scales. At larger scales velocity substructure is not found. We hypothesise that bound substructures exist on scales of ~ 0.5 parsecs, despite the region as a whole being unbound. We further hypothesise that any velocity substructure that existed on scales > 0.5 parsecs has been erased. The results of this study are then compared to those of other kinematic studies of Cygnus OB2.

Key words: stars: kinematics and dynamics – open clusters and associations: general – stars: formation

1 INTRODUCTION

Star forming regions are the focus of a great deal of scientific interest, and for good reason. They inform our understanding of how stars are born and how their environments evolve. Their study is also vital for our comprehension of the conditions that planets form in, and the type/number of planets which may exist in the universe.

Spatial and dynamical structure are perhaps the most important aspects defining a star forming region, but can be difficult to interpret. A number of statistical methods have been developed to quantify different aspects of the spatial structure of these regions (Allison et al. 2009; Cartwright 2009; Maschberger & Clarke 2011; Buckner et al. 2019), but they don't touch upon its velocity structure. However the Velocity Structure Analysis Tool (VSAT) (Arnold & Goodwin 2019) does, and it is used in this paper to investigate the velocity structure of Cygnus OB2, which has previously had relatively little statistical kinematic analysis.

Cygnus OB2 lies at a distance of approximately 1400 parsecs (Hanson 2003; Rygl et al. 2012; Berlanas et al. 2019), and has an estimated stellar mass of order 10^4 $M_\odot$ (Drew et al. 2008; Wright et al. 2010). Estimates of the region's age vary, for example Massey et al. (1995) find an age of 1-3 Myr and Wright et al. (2015) find an age up up to 7 Myr with star formation peaking 4-5 Myr ago. Given a number of estimates it seems relatively certain that the age of the region lies somewhere between 1 and 7 Myr.

This region is chosen because it has been extensively studied, (Massey & Thompson 1991; Knödlseder 2000; Comerón et al. 2008; Kiminki et al. 2015; Roquette et al. 2017; Berlanas et al. 2018, 2019) meaning there is a large amount of observational data already available. There have also been studies focused on its spatial and kinematic structure (Wright et al. 2014, 2016; Winter et al. 2019). This is useful as it allows findings relating to the kinematic structure of the region which are achieved using different techniques to be compared to see if they are consistent.

The structure of this paper is as follows. In section 2 the methods used to collect and analyse the data are outlined. In section 3 the results of the analysis are reported and in section 4 they are discussed. Finally in section 5 the conclusions drawn from the results are summarised.

2 METHODS

2.1 Data collection

For this work we use the X-ray selected sample of Cygnus OB2 members presented by Wright & Drake (2009) for the central portion of the association. X-rays provide a largely unbiased diagnostic of youth that is effective for separating young association members from older field stars, and Wright et al. (2010) made further efforts to identify and remove foreground contaminants from the sample. Proper motions for these stars were derived by Wright et al. (2016) as part of the DANCe (Dynamical Analysis of Nearby Clusters) project (Bouy et al. 2013).

The sample includes many of the known high-mass O-type stars in Cygnus OB2 with masses up to 100 $M_\odot$, as well as low-mass stars down to 0.1 $M_\odot$. The sample is estimated to be mostly complete to ~ 0.8 $M_\odot$ (Wright et al. 2014), and can be seen in Fig. 1. In this figure each star is shown as a dot with a line. The location of the dot indicates the location of the star and the length and direction of the line indicates the star's velocity. Visual inspection of the figure shows a small number of stars with velocities far greater than most. To investigate this we conduct an exploratory analysis of the data.

★ rebeccajasmi@umass.edu

© 2019 The Authors

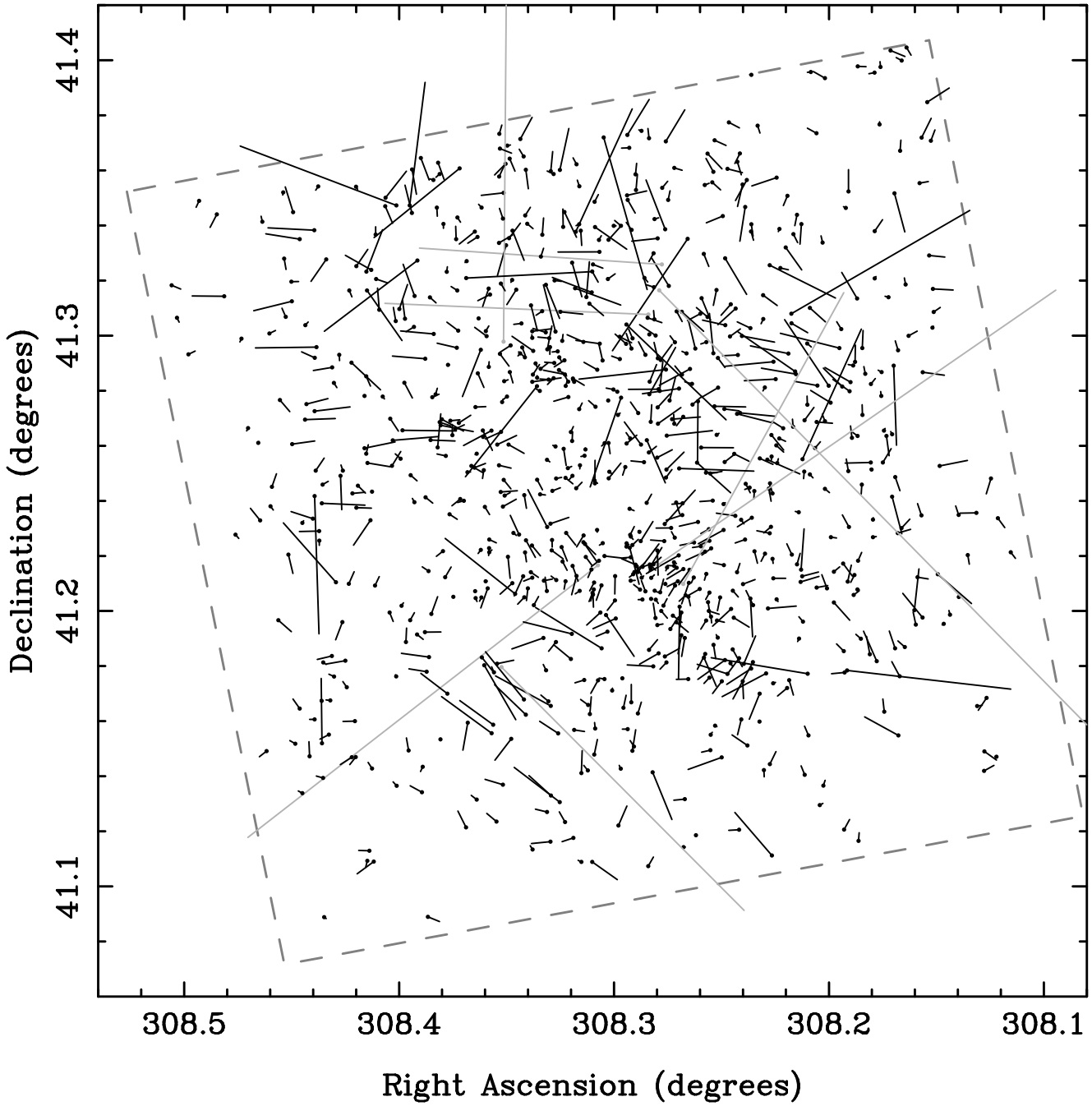

Figure 1. A plot of the data collected from the Cygnus OB2 region. The survey area of the X-ray observations of Wright & Drake (2009) is outlined by a grey dashed line. Each star is represented by a dot with a line. The position of the dot indicates the position of the star in RA (x-axis) and Dec (y-axis). The length and direction of the line coming from each dot indicates that star's velocity vector. Stars which are removed from the sample (as discussed in section 2.1) are shown by grey dots and vectors.

2.2 Exploratory analysis

Fig. 2 shows a scatter plot of the stellar velocities. As was the case for Fig. 1 it is visually apparent there are a small number of outliers. Additionally Fig. 3 shows a histogram with the stars binned by the number of standard deviations their speed is from this mean stellar speed, and from this it is clear there is a small number of stars which have speeds many standard deviations in excess of the mean stellar speed of the dataset. Note that in Fig. 3 the y-axis is logarithmic in order to make bins with few entries more easily visible.

The presence of extreme velocity outliers is also noted in Wright et al. (2016) where this dataset was first presented. That work concludes that these outliers are most likely due to:

- background/foreground stars that have been mistaken for members of Cygnus OB2
- stars ejected from Cygnus OB2 by dynamical events such as the disruption of binary systems
- stars now in the region of Cygnus OB2 but originating in nearby star clusters/associations which dispersed.

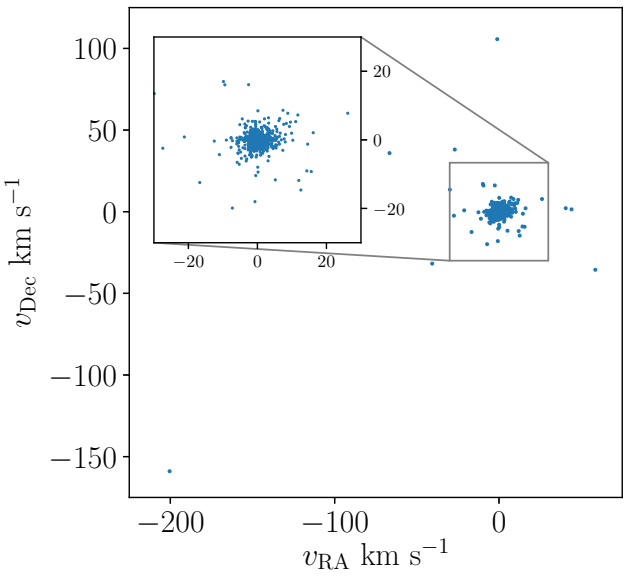

Figure 2. The RA and Dec stellar velocities plotted against one another.

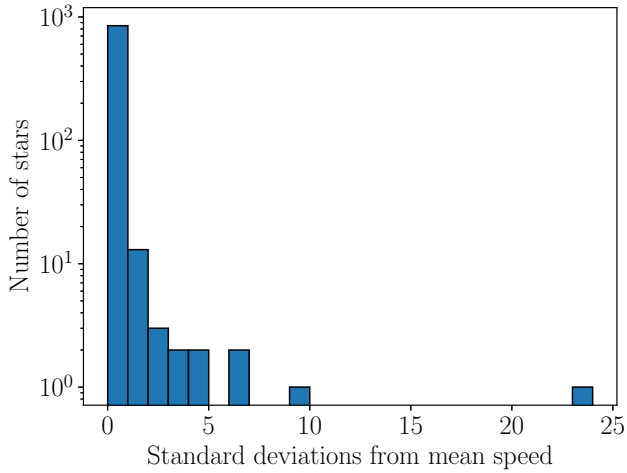

Figure 3. A histogram of the number of standard deviations stellar speeds are from the mean stellar speed in the Cygnus OB2 dataset. On the x-axis is number of standard deviations away from the mean. On the y-axis is the number of stars in each bin of the histogram. In order to ensure bins with a small number entries remain clearly visible the y-axis is logarithmic.

Regardless of their origin it is clear there is a small number of the 873 stars with very different velocities to the rest of the sample. Further, it seems unlikely that they are representative of the region's underlying velocity structure. Due to this, stars with speeds more than three standard deviations from the mean stellar speed in the dataset (a total of eight stars) are removed. This removal has very little impact on the results, and the effects it does have are discussed later. The removed stars are shown in grey in Fig. 1 and outside the grey inset in Fig. 2

In Fig. 2 velocities appear to be centrally concentrated but, particularly in the inset, there is no further obvious velocity structure apparent. To further investigate the velocity structure we plot stellar

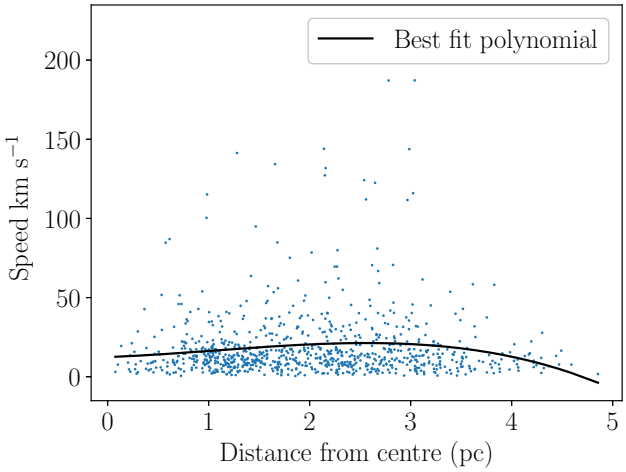

Figure 4. A scatterplot of stellar speeds plotted against their distance from the centre of the region. The polynomial that best fits this data is shown by a black line

speeds against their distances from the centre, see Fig. 4. The centre is defined here as the mean position of the stars.

There appears to be a peak in this distribution of points towards the centre of the plot but it is difficult to asses meaningfully by eye. To better understand it polynomials of increasing degrees are fitted, the adjusted R^2 coefficient is used to assess the goodness of each fit. This coefficient penalises additional degrees of freedom, which prevents overfitting. A 3rd degree polynomial is found to provide the best fit, and is shown by a black line on Fig. 4. Note that we do not argue that the data originated from this function, or even that this polynomial is a good fit. We only use it as a guide to better interpret the data. The best fitting polynomial does contain a peak which is located at 2.56 pc indicating stars with high speeds are preferentially located at moderate distances from the centre.

2.3 Data analysis

The VSAT method (Arnold & Goodwin 2019) is applied to analyse the velocity structure of the dataset in more detail. In brief the method is as follows: for every possible pair of stars this method calculates the distance between them (Δr) and their velocity difference (Δv). To clarify, here a 'pair of stars' does not necessarily refer to a binary system, but just to any two stars in the region. The pairs are then binned by Δr and within each bin the average Δv is calculated. Finally these are plotted against each other.

This method is applied twice, each time using a different definition of the velocity difference between two stars Δv. The first case is referred to as the magnitude definition, Δv_{M}, and it is defined as the magnitude of the difference between the two star's velocity vectors. Therefore for stars a and b Δv_{M} is calculated as:

$$\Delta v_{ab\mathrm{M}} = |\mathbf{v}_a - \mathbf{v}_b| \tag{1}$$

This definition is particularly useful as a raw measure of how similar/different stellar velocity vectors are.

The second way Δv is defined is as the time differential of Δr, i.e. the rate at which the distance between the stars is changing. This

is referred to as the directional definition, $\Delta v_{\rm D}$. For stars a and b this is

$$\Delta v_{ab\rm D} = \frac{(\mathbf{r}_a - \mathbf{r}_b)\cdot(\mathbf{v}_a - \mathbf{v}_b)}{\Delta r_{ab}}. \quad (2)$$

In this definition if the stars are moving away from each other Δr increases so $\Delta v_{\rm D}$ is positive, and if the stars are moving towards each other Δr decreases and $\Delta v_{\rm D}$ is negative. This definition is particularly useful for studying if regions or sub-regions are undergoing expansion/collapse. It as also useful for studying the relative motions of different substructures within a region. Both of these things are helpful in discerning the dynamical state of a region and its history.

In order to facilitate the calculation of these parameters the data is converted from RA, Dec, and proper motions into a Cartesian coordinate scheme. The Python package ASTROPY is used to perform this conversion.

3 RESULTS

3.1 Magnitude definition: $\Delta v_{\rm M}$

The VSAT method is applied to the dataset using the magnitude definition $\Delta v_{\rm M}$. The results are shown by the blue line in Fig. 5. On the x-axis of this figure is the distance between stars in parsecs, Δr, and on the y-axis is the average magnitude of the difference between stellar velocity vectors, $\Delta v_{\rm M}$, in km s^{-1}.

To demonstrate the degree of statistical noise the velocity vectors are randomly swapped between stars to remove any velocity structure. The method is re-run and the results recorded. This is done 1000 times. The area containing the central 1σ of results is shown by a shaded grey region in Fig. 5. Features in the non-randomised results (blue line) on scales smaller than the spread of these randomised results (grey area) are not significant as they are within the fluctuations in measured velocity structure due to pure stochasticity.

Inspection of Fig. 5 shows a dip at scales < 0.5 parsecs[1]. This means that stars closer to each other than this tend to have similar velocity vectors relative to the velocities across the whole region studied.

Between ~0.5 - 5.5 parsecs the measured velocity structure (blue) is almost completely flat; there is no change in the magnitude of the difference between stellar velocity vectors as a function of how far apart they are. Further, the small fluctuations from flatness that are observed are almost entirely within the 1σ bounds of those resulting from the regions where velocity structure has been removed by random shuffling (grey area). Therefore we conclude that there does not appear to be any velocity structure at these scales.

For Δr > 5.5 parsecs $\Delta v_{\rm M}$ dips again. However, the results at these large scales are noisy and have high uncertainties. This is largely due to the fact that only stars on the outermost edges of the dataset are far enough apart to have such high Δr. **Because of the morphology of the region which has lower stellar density towards its outskirts t**his means that there are fewer stellar pairs to populate these bins **at large separations**, and the results at $\Delta r \gtrsim 5.5$ parsecs are highly dependent on the exact velocity vectors of a small number of stars. Therefore although the measured 'structure' exceeds the bounds of the results with randomised velocity structures we cannot confidently determine whether velocity structure is or is not present at Δr beyond 5.5 parsecs.

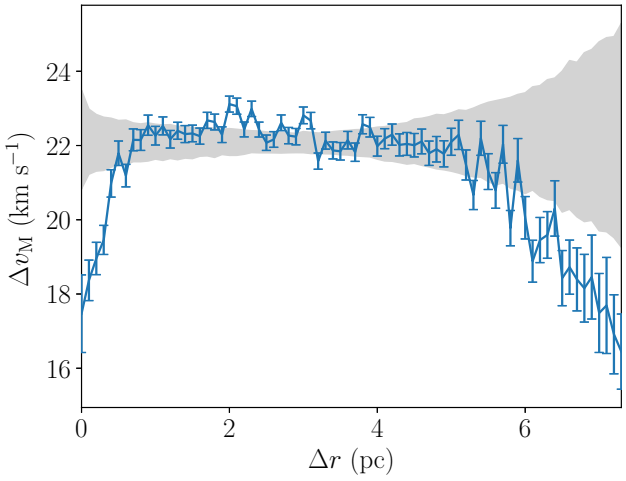

Figure 5. The velocity structure of Cygnus OB2 as determined by the VSAT method (Arnold & Goodwin 2019) (blue line). The area containing the central 1σ of the results of 1000 randomised cases is shown in grey. The x-axis shows the separation between stars in parsecs Δr, and on the y-axis is the average velocity difference of stellar pairs as defined by the magnitude definition of velocity difference, $\Delta v_{\rm M}$, in km s^{-1}.

3.2 Directional definition: $\Delta v_{\rm D}$

The VSAT method is now applied using the directional definition of the velocity difference, $\Delta v_{\rm D}$. Recall that in this definition the more rapidly stars tend to move away from each other the more positive $\Delta v_{\rm D}$ is, and the more rapidly stars tend to move towards each other the more negative it is. The results are shown by the blue line in Fig. 6[2]. As in Fig. 5 the x-axis shows distance between pairs of stars, Δr, in parsecs. The directional velocity difference $\Delta v_{\rm D}$ is given on the y-axis in km s^{-1}. As in section 3.1 velocity vectors are then randomly shuffled between stars to remove any velocity structure, and the VSAT method is re-applied. This is done 1000 times. The 1σ boundary of the results is plotted in grey on Fig. 6. This is done to give an idea of the amplitude of apparent velocity structures which in fact result from statistical noise.

The velocity structure of the region as measured using the directional definition of velocity difference does not fluctuate a great deal as a function of Δr. The blue line in Fig. 6 is largely flat, and the results are consistent with $\Delta v_{\rm D} = 0$ (no net expansion or contraction) for Δr < 3.5 parsecs. For Δr between 3.5 and 6 parsecs

[1] This feature is not visible if stars that are sigma clipped in section 2.1 are included. This is because, due to their locations, these stars feature in a disproportionately large number of low Δr pairs, and the < 0.5 parsec scale is particularly badly impacted. The sigma clipped stars have very different velocities to the rest of the dataset so their over representation causes an artificial increase in $\Delta v_{\rm M}$. This explains their impact on the < 0.5 parsec feature.

[2] These results are virtually indistinguishable from the results if the eight stars removed in section 2.1 are included. The only impact is minor changes to the exact fluctuations of the lines in Fig. 6, but the same overall trend is observed. This is as expected: if the clipped stars are truly not members of Cygnus OB2 they should have more or less random directions, so no net impact on the results of the directional definition $\Delta v_{\rm D}$.

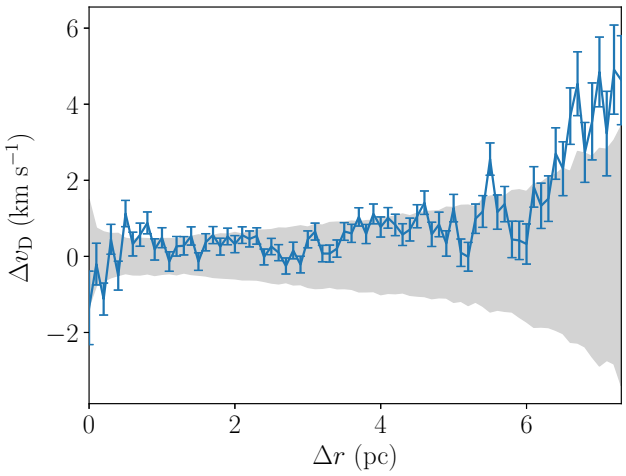

Figure 6. The velocity structure of Cygnus OB2 as determined by the VSAT method (Arnold & Goodwin 2019) (blue line). The area containing the central 1σ of the results of 1000 randomised cases is shown in grey. The x-axis shows the separation between stars in parsecs Δr, and on the y-axis is the average velocity difference of stellar pairs as defined by the directional definition of velocity difference, Δv_D, in km s^{-1}.

Δv_D is only very slightly above 0, and stays within the bounds of the randomised cases with no velocity structure.

At $\Delta r > 6$ parsecs the results show a positive correlation between Δr and Δv_D. Only stars on opposite sides of the dataset and close to its edges are far enough apart to populate these high Δr bins. Additionally, as stated, positive Δv_D indicating a stellar pair is moving apart. Therefore this result implies that stars towards the fringes of the dataset are moving outwards, i.e that the region is expanding from it edges. However, for reasons discussed in section 3.1 VSAT is not reliable beyond $\Delta r = 5.5$ parsecs for this dataset because of low number statistics. Therefore an additional test is conducted to verify whether this apparent expansion is real.

First all the stars that are present in $\Delta r > 6$ parsecs bins (we will call these fringe stars) are identified, and how many times they appear in those bins is recorded. Next the centre of the dataset is determined by taking the average position of all stars. The direction of each fringe star's velocity relative relative to the centre of the dataset if then calculated, with 0° indicating the star is moving radially outwards, 90° that it is moving tangentially, and 180° that is moving radially outwards. If fringe stars are moving systematically outwards then we expect thier mean angle to be < 90±2.90°. Note 2.90° is the expected standard deviation of the mean of a uniform distribution between 0 and 180° given the number of datapoints.

The mean angle of the fringe star's velocity directions are calculated. This mean is weighted by how many times each star appears in $\Delta r > 6$ parsecs bins, as recorded earlier. The mean is 88.00°, however this is within the expected standard deviation, 2.90°. Therefore we conclude there is no expansion from the edges of the dataset.

4 DISCUSSION

The results of our VSAT analysis of this part of Cygnus OB2 can be summarised as follows:

- there is velocity structure on scales < 0.5 parsecs;
- scales > 0.5 parsecs and < 5.5 parsecs are consistent with a random velocity field.

The grey areas on Fig. 5 and Fig. 6 show the 1 σ boundaries of the results using 1000 different realisations of randomly shuffling the velocities of stars. The only place where the actual data (the blue line) does not fall within the range of the randomised data at Δrs for which we have reliable results (i.e. < 5.5 parsecs) is on scales of < 0.5 parsecs for the magnitude definition shown in Fig. 5. Therefore, the only way in which the data departs from a randomised velocity field is that stars closer together than 0.5 parsecs have very similar velocity vectors. **As discussed we expect the method to be sensitive to velocity structures on scales < 5.5 parsecs, so the lack of any reliable 'signal' above 0.5 parsecs implies there is no velocity structure present on these scales.**

This result is possibly not particularly surprising given what we know about Cygnus OB2. A size-scale of ~ 0.5–1 parsecs is expected for bound groups of stars. It is the typical size of star clusters (see e.g. Portegies Zwart, McMillan & Gieles (2010)), the size of a typical molecular clump (Beuther et al. 2007), and is seen locally e.g. in Taurus (Gomez et al. 1993). Therefore, what we are probably seeing at < 0.5 parsec scales are many (probably fairly low-N) bound groups[3] which, because they are bound, have more similar velocity vectors than would be expected by chance as shown in Fig. 5. It is likely that some stars have become unbound from the groups since they formed due to dynamical interactions, and that these groups formed with somewhat higher N and larger size. However due to the youth of this region it is unlikely that the N and size of these groups has changed a great deal since their formation.

Note that we determine that the groups themselves must be bound because in order for unbound stars with similar velocities to remain within around 0.5 parsecs of each other for at least 3 Myr (the approximate region age) they must have a velocity dispersion of $\lesssim$ 0.17 km s^{-1}. This is implausibly low; it is more than a factor of 4 smaller than would be predicted for the velocity dispersion of molecular gas over the same size region by Larson's laws. Therefore we determine that such groups must be bound.

Given the large global 3D velocity dispersion of Cygnus OB2 of ~ 20 km s^{-1} (Wright et al. 2016) and typical age of a few Myrs (Massey et al. 1995; Wright et al. 2015) stars, or bound groups, will have moved 10s of parsecs from their birth sites. Therefore, stars we presently observe in this field of view (very roughly 10-by-10 parsecs) are unlikely to have formed within it.

That we are observing stars/groups that have moved a significant distance (possibly larger than our field of view) from where they formed means that observing a velocity field that is consistent with being random on all scales that are not bound is what we might well expect.

A large-scale random velocity field with many 'embedded' ~ 0.5 parsec bound groups is consistent with the high degree of spatial structure found by Wright et al. (2014) (they measure the Cartwright & Whitworth (2004) Q-parameter to be 0.4–0.5). It also fits the finding of Griffiths, Goodwin & Caballero-Nieves (2018) that the number of wide massive binaries in Cygnus OB2 suggests many (at least 30) different sites of massive star formation across the entire association.

It is worth noting that Winter, Clarke & Rosotti (2019) suggest a model for Cygnus OB2 as a superposition of four expanding

[3] It is not clear to us if they deserve the title 'clusters'

clusters. Their Figure 8(a) looks to the eye to be moderately similar to our Fig. 1. However, it might well lack the 0.5 parsec structures we find in the real data (as that scale was not imposed in their initial conditions and it is difficult to see how it could arise dynamically). A possible avenue for future work could be to analyse a variety of different idealised initial conditions to see which best-fit the real data.

5 CONCLUSIONS

We analyse the positions and proper motions of stars in a region of Cygnus OB2 from Wright et al. (2014) using the VSAT method presented in Arnold & Goodwin (2019).

Our main findings are:

- Stars within 0.5 parsecs of each other have significantly similar velocities.
- At all reliable scales larger than 0.5 parsecs velocities are consistent with a random distribution.
- There is no evidence of systematic expansion or collapse in this part of Cygnus OB2.

This suggests that we are observing many (presumably primordial) bound structures on scales < 0.5 parsecs ('groups' or small 'clusters'). However, any initial velocity structure on scales larger than 0.5 parsecs has been erased by stars having moved 10s of parsecs in the few Myr since they formed. Within this region we see no significant evidence for global expansion or contraction (but we note this is only the central part of Cygnus OB2).

ACKNOWLEDGEMENTS

NJW acknowledges an STFC Ernest Rutherford Fellowship (grant number ST/M005569/1). BA acknowledges PhD funding from the University of Sheffield. Many thanks also to Stuart Littlefair for useful discussions and insights.

REFERENCES

Allison R. J., Goodwin S. P., Parker R. J., Portegies Zwart S. F., de Grijs R., Kouwenhoven M. B. N., 2009, MNRAS, 395, 1449
Arnold B., Goodwin S. P., 2019, MNRAS, 483, 3894
Berlanas S. R., Herrero A., Comerón F., Simón-Díaz S., Cerviño M., Pasquali A., 2018, A&A, 620, A56
Berlanas S. R., Wright N. J., Herrero A., Drew J. E., Lennon D. J., 2019, MNRAS, 484, 1838
Beuther H., Churchwell E. B., McKee C. F., Tan J. C., 2007, in Reipurth B., Jewitt D., Keil K., eds, Protostars and Planets V. p. 165 (arXiv:astro-ph/0602012)
Bouy H., Bertin E., Moraux E., Cuillandre J. C., Bouvier J., Barrado D., Solano E., Bayo A., 2013, A&A, 554, A101
Buckner A. S. M., et al., 2019, A&A, 622, A184
Cartwright A., 2009, MNRAS, 400, 1427
Cartwright A., Whitworth A. P., 2004, MNRAS, 348, 589
Comerón F., Pasquali A., Figueras F., Torra J., 2008, A&A, 486, 453
Drew J. E., Greimel R., Irwin M. J., Sale S. E., 2008, MNRAS, 386, 1761
Gomez M., Hartmann L., Kenyon S. J., Hewett R., 1993, AJ, 105, 1927
Griffiths D. W., Goodwin S. P., Caballero-Nieves S. M., 2018, MNRAS, 476, 2493
Hanson M. M., 2003, ApJ, 597, 957
Kiminki D. C., Kobulnicky H. A., Vargas Álvarez C. A., Alexander M. J., Lundquist M. J., 2015, ApJ, 811, 85
Knödlseder J., 2000, A&A, 360, 539
Maschberger T., Clarke C. J., 2011, MNRAS, 416, 541
Massey P., Thompson A. B., 1991, ApJ, 101, 1408
Massey P., Johnson K. E., Degioia-Eastwood K., 1995, ApJ, 454, 151
Portegies Zwart S. F., McMillan S. L. W., Gieles M., 2010, ARAA, 48, 431
Roquette J., Bouvier J., Alencar S. H. P., Vaz L. P. R., Guarcello M. G., 2017, A&A, 603, A106
Rygl K. L. J., et al., 2012, A&A, 539, A79
Winter A. J., Clarke C. J., Rosotti G. P., 2019, MNRAS, 485, 1489
Wright N. J., Drake J. J., 2009, ApJS, 184, 84
Wright N. J., Drake J. J., Drew J. E., Vink J. S., 2010, ApJ, 713, 871
Wright N. J., Parker R. J., Goodwin S. P., Drake J. J., 2014, MNRAS, 438, 639
Wright N. J., Drew J. E., Mohr-Smith M., 2015, Monthly Notices of the Royal Astronomical Society, 449, 741
Wright N. J., Bouy H., Drew J. E., Sarro L. M., Bertin E., Cuillandre J.-C., Barrado D., 2016, MNRAS, 460, 2593

This paper has been typeset from a TEX/LATEX file prepared by the author.

Chapter 6

The properties of ejected stars

6.1 Summary

This chapter presents the paper ‘Dynamical evolution of star-forming regions: III. Unbound stars and predictions for Gaia’ (Schoettler et al. 2019). In this paper *N*-body simulations of star forming regions with different initial conditions are performed and the properties of stars that become unbound from the regions are studied. No high mass runaway stars (see section 1.3 of this thesis) are observed, however lower mass ”walkaway stars” (stars ejected from the cluster with velocities 5 - 30 km s^{-1}) are. Further the properties and fractions of ejected stars are found to correlate with the initial conditions of the simulated regions.

6.2 Description of my contribution to this work

In some of the simulations performed in this work multiple clusters (mainly binary clusters) form. See section 1.6 and the entirety of chapter 3 for more information on such clusters. This presents additional difficulties to the problem of identifying which stars are unbound:

- It must be determined if more than one cluster is present, and if so how many.
- If more than one cluster is present their memberships must be determined.

In the course of my work on Arnold et al. (2017) (presented in chapter 3) I developed a piece of software which algorithmically identified the number of clusters in a simulation snapshot, and determined the membership of each based on boundedness arguments. I modified this software to be more user friendly, provided it to C. Schoettler, and trained her on its use, abilities, and potential

weaknesses. By making use of this software she was able to find which stars are unbound from any cluster in simulations where multiple clusters form. This allowed the properties of unbound stars to be studied in the full set of simulations, not just those that formed single concentrated star clusters.

I also contributed to this work by reviewing multiple drafts and providing feedback.

6.3 The paper

The full published version of the paper is presented below.

Monthly Notices
of the
ROYAL ASTRONOMICAL SOCIETY

MNRAS **487,** 4615–4630 (2019)
Advance Access publication 2019 May 31

doi:10.1093/mnras/stz1487

Dynamical evolution of star-forming regions: III. Unbound stars and predictions for *Gaia*

Christina Schoettler,[1,2]★ Richard J. Parker,[1]† Becky Arnold,[1] Liam P. Grimmett,[1] Jos de Bruijne[2] and Nicholas J. Wright[3]

[1]*Department of Physics and Astronomy, The University of Sheffield, Hicks Building, Hounsfield Road, Sheffield S3 7RH, UK*
[2]*Science Support Office, Directorate of Science, European Space Research and Technology Centre (ESA/ESTEC), Keplerlaan 1, NL-2201 AZ Noordwijk, the Netherlands*
[3]*Astrophysics Group, Keele University, Keele ST5 5BG, UK*

Accepted 2019 May 22. Received 2019 May 22; in original form 2019 April 1

ABSTRACT

We use *N*-body simulations to probe the early phases of the dynamical evolution of star-forming regions and focus on mass and velocity distributions of unbound stars. In this parameter space study, we vary the initial virial ratio and degree of spatial and kinematic substructure and analyse the fraction of stars that become unbound in two different mass classes (above and below 8 $M_\odot$). We find that the fraction of unbound stars differs depending on the initial conditions. After 10 Myr, in initially highly subvirial, substructured simulations, the high-mass and lower mass unbound fractions are similar at ∼23 per cent. In initially virialized, substructured simulations, we find only ∼16 per cent of all high-mass stars are unbound, whereas ∼37 per cent of all lower mass stars are. The velocity distributions of unbound stars only show differences for extremely different initial conditions. The distributions are dominated by large numbers of lower mass stars becoming unbound just above the escape velocity of ∼3 km s^{-1} with unbound high-mass stars moving faster on average than lower mass unbound stars. We see no high-mass runaway stars (velocity > 30 km s^{-1}) from any of our initial conditions and only an occasional lower mass runaway star from initially subvirial/substructured simulations. In our simulations, we find a small number of lower mass walkaway stars (with velocity 5–30 km s^{-1}) from all of our initial conditions. These walkaway stars should be observable around many nearby star-forming regions with *Gaia*.

Key words: methods: numerical – stars: formation – stars: kinematics and dynamics – open clusters and associations: general.

1 INTRODUCTION

The majority of stars do not form in isolation but in environments where stellar densities are higher than in the Galactic field (Lada & Lada 2003; Bressert et al. 2010). Depending on the initial conditions in these star-forming regions, they either evolve into bound clusters or unbound groups. Most stars born in clusters do not remain there past an age of 10 million years (Myr) and only about 10 per cent are observed in gravitationally bound clusters at this age (Lada & Lada 2003). Young stars that are not members of bound clusters are usually observed in unbound groups of stars (i.e. associations; Blaauw 1964) before they disperse into the Galactic field.

For the last two decades, the prevailing view has been that bound star clusters are fundamental units of star formation – in that most stars form in these dense, embedded environments until gas exhaustion (Longmore et al. 2014) or residual gas expulsion conclude star formation. Gas expulsion can also lead to the cluster's dissolution (Tutukov 1978; Lada, Margulis & Dearborn 1984; Goodwin 1997; Goodwin & Bastian 2006; Longmore et al. 2014; Shukirgaliyev et al. 2018). In this scenario, associations must have formed as single or multiple clusters and expanded into their unbound state (so-called monolithic star formation; e.g. Kroupa, Aarseth & Hurley 2001; Baumgardt & Kroupa 2007). An alternative view is that depending on the initial conditions of the molecular clouds, clusters or associations are formed when smaller clustered regions with differing stellar densities assemble hierarchically. These smaller groups of stars are the result of hierarchical fragmentation of the molecular clouds. In this scenario, star formation can lead to the formation of a dense, bound star cluster but can also result in lower

★ E-mail: cschoettler1@sheffield.ac.uk
† Royal Society Dorothy Hodgkin Fellow.

© 2019 The Author(s)
Published by Oxford University Press on behalf of the Royal Astronomical Society

Downloaded from https://academic.oup.com/mnras/article-abstract/487/4/4615/5509598 by University of Sheffield user on 20 August 2019

density, unbound associations (so-called hierarchical star formation; e.g. Bonnell et al. 2011; Kruijssen 2012). Recent work has shown that associations are unlikely to be dissolved clusters, supporting the latter star formation scenario (e.g. Wright et al. 2016; Ward & Kruijssen 2018; Wright & Mamajek 2018).

One way of testing these two scenarios observationally is to determine the initial density (i.e. spatial structure) and virial ratio (i.e. velocity structure) of star-forming regions. This remains difficult as dynamical evolution can lead to significant changes to star-forming regions over a short period of time (e.g. Allison et al. 2010; Park, Goodwin & Kim 2018) such as a rapid reduction in density in regions with initially high stellar densities (e.g. Marks & Kroupa 2012; Parker 2014). Initial substructure can be erased (e.g. Goodwin & Whitworth 2004; Allison et al. 2010; Jaehnig, Da Rio & Tan 2015), the location of the most massive stars can change due to dynamical mass segregation (e.g. Allison et al. 2009; Parker et al. 2014), and primordial binary systems can be destroyed (e.g. Kroupa 1995; Marks & Kroupa 2012; Parker & Goodwin 2012; Duchêne et al. 2018). A dense phase can also have disruptive effects on protoplanetary discs and young planetary systems around stars in star-forming regions (e.g. Bonnell et al. 2001; Adams et al. 2006; Parker & Quanz 2012; Winter et al. 2018; Nicholson et al. 2019).

Our earlier work showed that information from the spatial distribution of star-forming regions can be used to distinguish the initial bound/unbound state (initial virial ratio; Parker et al. 2014; Paper I). Parker & Wright (2016; Paper II) showed that using radial velocity dispersion in combination with a spatial structure diagnostic (Q-parameter; Cartwright & Whitworth 2004) can help constrain initial conditions in star-forming regions with high local densities. In this paper, we will focus on stars that become unbound from young star-forming regions.

Observationally, unbound stars are easiest to identify when their velocities are higher than their surroundings and they have high mass and therefore high luminosity, such as OB stars. These stars have a mass of at least $8\,M_\odot$ and short lifetimes of up to a few tens Myr, with the most massive stars undergoing core-collapse supernovae after only a few Myr (Zinnecker & Yorke 2007). Most star-forming regions dissolve after only a few tens Myr but they can still outlive the massive stars located within them (Portegies Zwart, McMillan & Gieles 2010). As a consequence, OB stars should not be found outside these regions. However, there are OB stars found far outside star-forming regions moving at much higher velocities than normally expected. These OB stars have been termed runaway stars by Blaauw (1961). They show a peculiar velocity (i.e. velocity relative to a rest frame) in excess of ∼30–$40\,km\,s^{-1}$ and/or are located at large distances from any star-forming regions or the Galactic plane (e.g. Blaauw 1956, 1961; Stone 1991; Hoogerwerf, de Bruijne & de Zeeuw 2001; de Wit et al. 2005; Eldridge, Langer & Tout 2011; Drew et al. 2018). Almost all currently identified runaway stars are high-mass stars (see the recent catalogue in Tetzlaff, Neuhäuser & Hohle 2011). Low-mass runaway star detections remain rare (Poveda, Allen & Hernández-Alcántara 2005; de la Fuente Marcos & de la Fuente Marcos 2018). A lower velocity limit for runaway stars has been suggested by Eldridge et al. (2011) at $\sim 5\,km\,s^{-1}$, as stars ejected with this velocity can still travel a considerable distance in just a few Myr and end up tens of pc from any star-forming regions, satisfying distance-based runaway star definitions (e.g. de Wit et al. 2005). This subset of slower runaway stars has recently been termed walkaway stars (de Mink et al. 2014).

Runaway and walkaway stars are thought to be the result of the same two ejection mechanisms. Blaauw (1961) suggested that ejection of these stars is due to the binary supernova mechanism. This posits that in a close binary, the secondary star is ejected when the more massive primary reaches the end of its life and undergoes a core-collapse supernova. With a high enough kick velocity from the supernova, the main-sequence companion gets ejected due to binary disruption, almost always leaving an ejected singleton star. Poveda, Ruiz & Allen (1967) suggested an alternative mechanism due to dynamical interaction. In dense star-forming regions, stars interact with each other dynamically and close encounters between three or even four stars can lead to ejection of one or two of them. When a single, massive star interacts with a binary where the secondary is a lower mass star, the single star can replace this secondary binary star, which is then ejected from the star cluster at a similar maximum velocity than in the binary supernova mechanism (Gvaramadze, Gualandris & Portegies Zwart 2009).

In this paper, we use pure *N*-body simulations with differing initial conditions to investigate if the number and velocity distributions of unbound stars can allow us to place constraints on the initial density and velocity structure in star-forming regions. We aim to make predictions for observations of fast unbound stars from young star-forming regions that can be probed with *Gaia* Data Release 2 (DR2) (Gaia Collaboration 2018). DR2 contains five-parameter astrometry (position, parallax, and proper motion) for over 1.3 billion sources down to an apparent G-magnitude limit of $G \approx 21$, whereas radial velocity information is only available for brighter sources (∼7.2 million; Gaia Collaboration 2018). Our simulations provide us with 6D-parameter space results (position and velocity), but we focus on the 2D-plane and 2D-velocity, i.e. tangential velocity, that calculated from proper motion and distance (or parallax) in observations.

This paper is organized as follows. In Section 2, we present the initial conditions used for the *N*-body simulations and our definition of unbound stars. Section 3 is dedicated to the results with a discussion of these results in Section 4, followed by our conclusions in Section 5.

2 METHODS

2.1 Initial conditions

Our simulated star-forming regions are set up with 1000 systems per simulation distributed across an initial radius of 1 pc. All systems are initially single stars (no primordial binaries) and their masses are randomly sampled for every single simulation from the Maschberger (2013) initial mass function (IMF). This form of the IMF combines the Salpeter (1955) power-law slope for stars with masses above $1\,M_\odot$ with a Chabrier (2005) lognormal IMF approximation at the lower mass end. The Maschberger IMF is described by a probability density function with three parameters $\alpha = 2.3$ (power-law exponent for higher mass stars), $\beta = 1.4$ (describing the IMF slope of lower mass stars), and $\mu = 0.2$ (average stellar mass; Maschberger 2013):

$$p(m) \propto \frac{\left(\frac{m}{\mu}\right)^{-\alpha}}{\left(1+\left(\frac{m}{\mu}\right)^{1-\alpha}\right)^{\beta}}. \quad (1)$$

We sample stellar masses m between $0.1\,M_\odot$ (we do not include brown dwarfs) and $50\,M_\odot$, resulting in total masses between ∼500 and $700\,M_\odot$ for each of our star-forming regions.

Downloaded from https://academic.oup.com/mnras/article-abstract/487/4/4615/5509598 by University of Sheffield user on 20 August 2019

The spatial structure is set up following the method described in Goodwin & Whitworth (2004). It uses fractal distributions to define the observed substructure in young star-forming regions using a single parameter, the fractal dimension D. Starting with a cube with side $N_{\rm div} = 2$, a parent particle is placed at the centre. This first parent cube is subdivided into equal-sized $N_{\rm div}^3$ subcubes with a first-generation descendant in each centre. Depending on the survival probability $N_{\rm div}^{(D-3)}$ that is set by the fractal dimension D, these descendants can become parents themselves. For a low fractal dimension fewer descendants become parents, whereas more descendants survive when using a high fractal dimension. Descendants that do not survive are deleted along with their parent. The positions of the surviving particles are adjusted by adding a small amount of noise. This process continues until more stars than required are generated within the original cube. We cut a sphere from this cube and reduce the remaining stars down to the required number by random deletion.

We use a set of four different fractal dimensions for our simulations to investigate a wide parameter space. Starting with highly substructured star-forming regions ($D = 1.6$), we then gradually reduce the level of substructure ($D = 2.0$ and $D = 2.6$) finishing with a roughly uniform, smooth sphere ($D = 3.0$).

Like the spatial structure, the velocity structure in our simulations is also set up to mimic observed star formation environments. Molecular gas clouds show turbulence that can be passed down to the stars that form from them. The velocity dispersion increases with the size of the clouds. In molecular clouds, large velocity dispersions can occur on large scales, whereas on small scales there are smaller dispersions, i.e. similar velocities (Larson 1981). Star formation occurs in filamentary structures within these gas clouds, where the velocity dispersion is low (André et al. 2014). To represent this velocity structure in our simulations, we follow Goodwin & Whitworth (2004), which results in close stars with similar velocities and distant stars with different velocities. The process starts by assigning a random velocity to the parents. The next generation inherits this velocity, which is in turn adjusted by a random component that gets smaller with every following generation. The velocities of the stars are finally scaled to five different global virial ratios. The global virial ratio $\alpha_{\rm vir}$ describes the ratio of total kinetic energy T of all stars to the modulus of the total potential energy Ω of all stars, $\alpha_{\rm vir} = T/|\Omega|$. A star-forming region in virial equilibrium has a global virial ratio $\alpha_{\rm vir} = 0.5$, with subvirial regions at values below and supervirial ones above.

In our parameter space, we investigate star-forming regions initially in virial equilibrium as well as two regions that are initially subvirial ($\alpha_{\rm vir} = 0.1$ and $\alpha_{\rm vir} = 0.3$) and two supervirial ($\alpha_{\rm vir} = 1.0$ and $\alpha_{\rm vir} = 1.5$) initial settings. These global virial ratios describe the bulk motion of the stars as a whole. On local scales, stars have similar, correlated velocities, meaning star-forming regions can be locally subvirial even if they are not subvirial on a global scale. This can lead to local, but not global collapse during the early dynamical evolution of the star-forming region (Allison et al. 2010; Parker & Wright 2016).

We use the N-body integrator `kira` from the `Starlab` package (Portegies Zwart et al. 1999, 2001) to evolve our star-forming regions over a defined time period. The integrator uses an input N-body system defined by our initial conditions and evolves it overtime giving output at different snapshots. The motion of the stars in the simulations is followed using a fourth-order, block-time-step Hermite scheme (Makino & Aarseth 1992).

With four different initial fractal dimensions and five different initial virial ratios, we run 20 simulations of each of the 20 combinations for a time period of 10 Myr to cover the early phases of the evolution of a star-forming region. The only changes within the simulations sharing the same initial conditions are the random number seed used to initiate the creation of the fractal (i.e. initial positions and velocities of stars) and the sampling of stellar masses from the IMF. For each set of initial conditions, we combine the results of all 20 simulations, thus creating a larger data set for analysis. Our star-forming regions do not have a gas potential and there is no external/tidal field applied. The stars do not undergo stellar evolution and are not in primordial binaries or initially mass segregated. This allows us to identify the effects of different initial spatial and velocity substructure on the unbound population from young star-forming regions. In future work, we will include both stellar evolution and primordial binaries to quantify the effect each has on stars becoming unbound from these regions.

2.2 Unbound stars and fractions by mass class

We consider a star i to be unbound once it has positive total energy (i.e. its kinetic energy T_i is larger than the modulus of its potential energy Ω_i). Its kinetic energy is given by

$$T_i = \frac{1}{2} m_i |\boldsymbol{v}_i - \boldsymbol{v}_{\rm cr}|^2, \tag{2}$$

where m_i is the mass of star i and $\boldsymbol{v}_i$ and $\boldsymbol{v}_{\rm cr}$ are the velocity vectors of this star and of the centre of the region, respectively. The potential energy of the star i is given by the sum of the potential energy between star i and every other star j:

$$\Omega_i = -\sum_{i \neq j} \frac{G m_i m_j}{r_{ij}}, \tag{3}$$

where G is the gravitational constant, m_i and m_j are the stellar masses of i and j, respectively, and r_{ij} is the distance between them. After identifying all unbound stars in each snapshot, we divide them up into two mass classes [low/intermediate-mass ($<8\,{\rm M}_\odot$) and high-mass ($\geq 8\,{\rm M}_\odot$) stars]. We then calculate unbound fractions by normalizing the number of unbound stars (UB) by the total number of stars (TOT) in that specific mass class (MC):

$$\text{Unbound fraction} = \frac{N_{\rm MC,UB}}{N_{\rm MC,TOT}}. \tag{4}$$

We estimate the standard error of the mean (SE) as a representation of the uncertainty connected to the unbound fractions, where s is the sample standard deviation and n is the number of simulations:

$$\text{SE} = \frac{s}{\sqrt{n}}. \tag{5}$$

The uncertainty is caused by the stochastic nature of the underlying dynamical evolution (Allison et al. 2010; Parker et al. 2014). In our parameter space study, this different evolution is evident in the different unbound fractions from statistically identical, individual simulations as shown in Fig. 1. This figure illustrates how different the unbound fractions can be for 10 simulations with the same initial conditions [initially subvirial ($\alpha_{\rm vir} = 0.3$) and high levels of substructure ($D = 1.6$)]. The different lines represent the fractions of unbound stars as a function of time and in this example they can increase over the simulation time to values between ∼18 and 48 per cent after 10 Myr.

Downloaded from https://academic.oup.com/mnras/article-abstract/487/4/4615/5509598 by University of Sheffield user on 20 August 2019

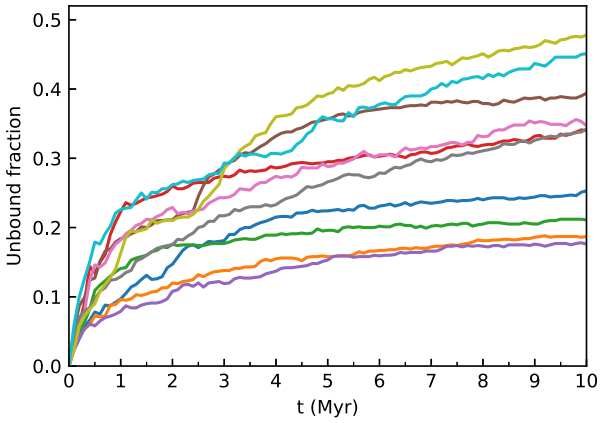

Figure 1. Unbound fractions from 10 simulations (initially subvirial $\alpha_{\rm vir} = 0.3$, with high level of initial substructure $D = 1.6$) showing the spread of the unbound fractions between statistically identical simulations.

3 RESULTS

For the following analysis of velocities, we focus on 2D-velocities to allow us to make predictions for proper motion observations, such as from the recent *Gaia* DR2 (Gaia Collaboration 2018). In observations, we have a fixed 2D-plane, whereas the choice of 2D-plane from simulations is arbitrary. The 2D-velocity results shown in this section represent the tangential velocity in the *xy*-plane (i.e. calculated as the motion across the sky would be in observations), however, any other choice of 2D-plane gives us the same results after considering statistical noise.

3.1 Cumulative 2D-velocity distributions of all stars

We first focus on the cumulative distributions of the 2D-velocities and analyse how these evolve over the time period covered by our simulations. For each set of initial conditions, the cumulative distributions contain all stars from 20 simulations. In Fig. 2, we see the evolution of the cumulative distributions of the 2D-velocity at four different times from the left-hand to the right-hand column (0, 1, 5, and 10 Myr). From the top row to the bottom, we see that the four different fractal dimensions at 0 Myr show almost identical cumulative velocity distributions for all five initial virial ratios. This is to be expected as the virial ratio acts as a scaling factor for the initial velocities.

During the first 1 Myr, star-forming regions that are initially highly to moderately substructured ($D \leq 2.0$) collapse and undergo violent relaxation (e.g. Lynden-Bell 1967; van Albada 1982; Funato, Makino & Ebisuzaki 1992; McMillan, Vesperini & Portegies Zwart 2007; Moeckel & Bonnell 2009; Allison et al. 2010; Spera & Capuzzo-Dolcetta 2017) with subvirial regions ($\alpha_{\rm vir} < 0.5$) collapsing rapidly to form bound, spherical clusters (Parker et al. 2014). Some of the initially virialized regions ($\alpha_{\rm vir} = 0.5$) undergo a local collapse in regions of high substructure. Even though they are initially virialized on a global scale, they can be subvirial locally resulting in a localized collapse. Star-forming regions with little or no initial substructure ($D \geq 2.6$) collapse only when they are also initially subvirial.

At 1 Myr (second column), the velocity distributions of different initial virial ratios show similar velocities for identical levels of initial substructure. Initially, highly subvirial regions ($\alpha_{\rm vir} = 0.1$) that are slowest at the start of the simulations attain similar velocities to initially virialized and supervirial regions when $D \leq 2.0$ or higher velocities when $D \geq 2.6$. Violent relaxation leads to an increase in velocity, which is highest in highly subvirial, substructured initial conditions.

After 5 and 10 Myr (third and fourth column), in initially more substructured regions ($D \leq 2.0$) the evolution of the cumulative distributions follows a similar pattern. The bound, initially subvirial, or virialized regions ($\alpha_{\rm vir} \leq 0.5$) have very similar velocity distributions as the initially subvirial regions approach virial equilibrium after violent relaxation. Initially, supervirial regions ($\alpha_{\rm vir} > 0.5$) remain unbound and at higher average velocities. The difference between the subvirial/virial and supervirial distributions becomes clearer the older the simulated regions get, as the initially subvirial/virialized regions slow down compared to the initially supervirial ones.

Star-forming regions with less substructure initially ($D \geq 2.6$) do not show the clear separation of velocity distributions between subvirial/virial and supervirial initial ratios. Only initially highly supervirial regions ($\alpha_{\rm vir} = 1.5$) have a velocity distribution at later times that can be distinguished from those with lower virial ratios. The initially smooth, sphere-like regions ($D = 3.0$) still show a grouping together of the velocity distributions after 5 Myr. The two initially supervirial distributions ($\alpha_{\rm vir} = 1.0$ and 1.5) are located either side of the initially subvirial and virialized ones. Despite both being supervirial, they exhibit considerably different velocity distributions. Moderately supervirial regions ($\alpha_{\rm vir} = 1.0$) have the slowest, whereas highly supervirial regions ($\alpha_{\rm vir} = 1.5$) have the fastest cumulative 2D-velocities. This behaviour continues for the remaining 5 Myr and at the end of our simulations the moderately supervirial cases are still indistinguishable from those of initially subvirial/virialized ($\alpha_{\rm vir} \leq 0.5$) cases.

3.1.1 *Long-term evolution of initially smooth star-forming regions*

For these initially smooth star-forming regions ($D = 3.0$), we follow the evolution of their cumulative distributions for a longer time period. We evaluate if they evolve differently or just more slowly than initially more substructured star-forming regions. The evolution of these smooth regions is shown at 10, 25, 50, and 100 Myr in Fig. 3.

The cumulative distributions for initially subvirial and virialized regions ($\alpha_{\rm vir} \leq 0.5$) continue to be similar as they are in a state of virial equilibrium. The velocity distribution for the moderately supervirial regions ($\alpha_{\rm vir} = 1.0$, red) starts to become distinguishable from the initially subvirial/virialized regions after 50 Myr, as these regions slow down compared to the moderately supervirial one.

But even after 100 Myr, the velocities of moderately supervirial regions are still much closer to those of initially subvirial/virial star-forming regions than the highly supervirial scenario. Initially smooth, supervirial star-forming regions appear to evolve in a similar fashion than the more substructured regions but on a much longer time-scale. The long-term evolution of the cumulative distributions shows that the average velocities decrease at later times for initially subvirial/virialized regions, as the global gravitational field of the bound clusters causes stars to decelerate.

3.2 Unbound fractions of stars from initially subvirial and virialized regions

In this section, we turn to unbound fractions for initially subvirial and virialized star-forming regions ($\alpha_{\rm vir} \leq 0.5$). We exclude the two supervirial scenarios as in these globally unbound, expanding

Downloaded from https://academic.oup.com/mnras/article-abstract/487/4/4615/5509598 by University of Sheffield user on 20 August 2019

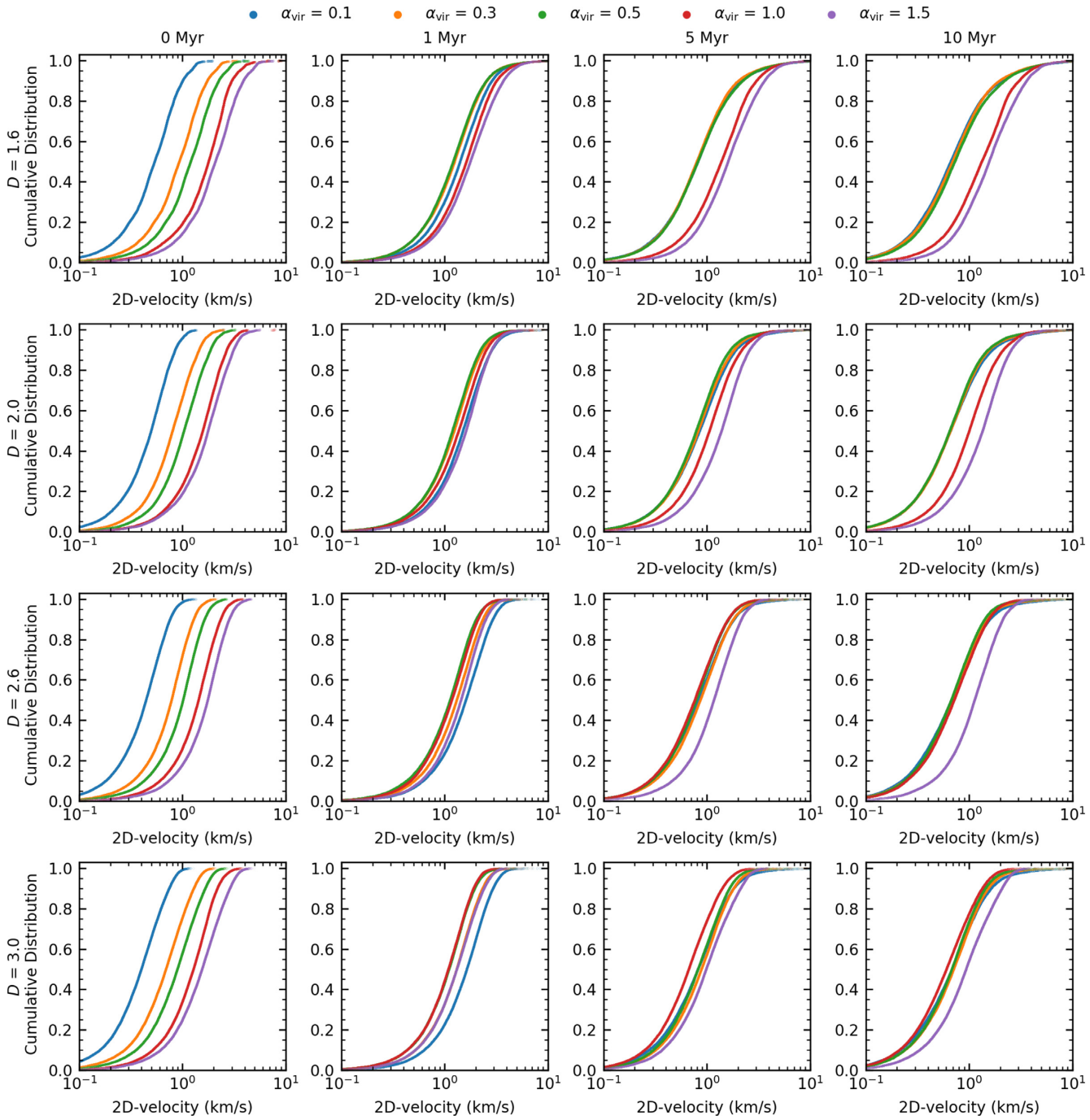

Figure 2. Cumulative 2D-velocity distributions at four different simulation times (in columns: 0, 1, 5, 10 Myr) and for the different initial condition sets. Each row represents a different fractal dimension from $D = 1.6$ (top row) to $D = 3.0$ (bottom row). The five different initial virial ratios [$\alpha_{vir} = 0.1$ (blue), $\alpha_{vir} = 0.3$ (orange), $\alpha_{vir} = 0.5$ (green), $\alpha_{vir} = 1.0$ (red), and $\alpha_{vir} = 1.5$ (purple)] are shown in each panel for each fractal dimension and time.

regions most stars are born unbound. In our simulations, we do not have any stellar evolution, so stars can only become unbound due to dynamical interactions with other stars (Poveda et al. 1967) and not from supernova kicks (Blaauw 1961). In the absence of an external tidal field, lower mass stars mainly become unbound due to effects of two-body relaxation (Binney & Tremaine 2008), whereas high-mass stars require dynamical interactions with other high-mass stars in binaries or higher order multiple systems (e.g. trapezium-like) to become unbound (Allison & Goodwin 2011; Parker et al. 2016).

3.2.1 Effects of different levels of substructure in regions with the same initial virial ratio

In Fig. 4, unbound fractions for star-forming regions with an initially highly subvirial ratio ($\alpha_{vir} = 0.1$) are shown in the first column. With high levels of initial substructure ($D = 1.6$, first row) stars in both mass classes show similar unbound fractions from 5 Myr to the end of the simulations. These regions, regardless of initial degree of substructure, will undergo rapid collapse and violent relaxation. While low/intermediate-mass stars become unbound early in the

Downloaded from https://academic.oup.com/mnras/article-abstract/487/4/4615/5509598 by University of Sheffield user on 20 August 2019

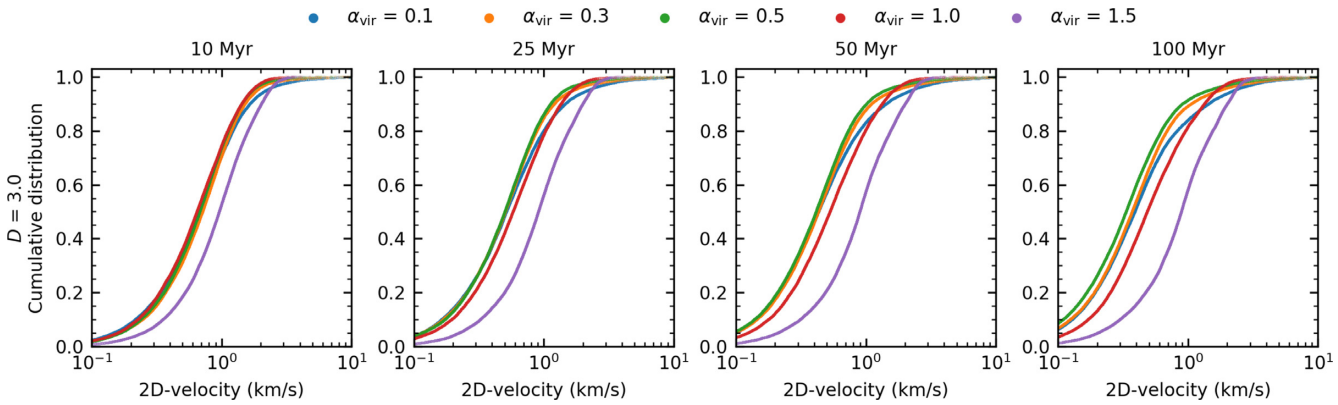

Figure 3. Long-term evolution of the cumulative 2D-velocity distributions at four different simulation times (10, 25, 50, and 100 Myr) for the five different initial virial ratios [$\alpha_{vir} = 0.1$ (blue), $\alpha_{vir} = 0.3$ (orange), $\alpha_{vir} = 0.5$ (green), $\alpha_{vir} = 1.0$ (red), and $\alpha_{vir} = 1.5$ (purple)] and constant fractal dimension ($D = 3.0$).

simulations, high-mass stars show a more gradual increase and match the lower mass unbound fraction at ∼5 Myr. The lower mass unbound fraction decreases with less initial substructure and settles on the same level of ∼20 per cent for more moderate amounts of initial substructure ($D = 2.0$–3.0) after 10 Myr. At the end of our simulations, the high-mass unbound fractions in the four initial substructure scenarios reach final values between 22 ± 3 per cent and 28 ± 4 per cent.

We see a delay in high-mass stars becoming unbound that increases the lower the level of initial substructure (i.e. higher fractal dimension D) in initially highly subvirial regions ($\alpha_{vir} = 0.1$, first column). In these simulations, the degree of collapse reduces with lower amounts of initial substructure, resulting in a longer formation time for multiple star systems that can eject massive stars. The low/intermediate-mass stars also show a delay in stars becoming unbound for $D = 2.6$–3.0. The delay is most obvious in regions with no initial substructure ($D = 3.0$, bottom row). On average, only seven stars (all are low/intermediate-mass) per simulation become unbound in the first ∼0.5 Myr. The lack of initial substructure combined with the low initial virial ratio appears to result in a 'balanced' collapse that keeps virtually all stars in a bound configuration for a short period of time (∼0.5 Myr).

In initially moderately subvirial simulations ($\alpha_{vir} = 0.3$, second column), the star-forming regions undergo an initial collapse but the degree of collapse is lower when compared to the highly subvirial simulations. We decrease the level of initial substructure and see a significant decrease in the low/intermediate-mass unbound fraction for every change in fractal dimension. After 10 Myr, the high-mass unbound fractions only slightly decrease (from 20 ± 4 per cent to 19 ± 3 per cent) for regions with initially high or moderate levels of substructure ($D \leq 2.0$). Further decreasing the initial substructure reduces the high-mass unbound fraction to 16 ± 2 per cent ($D = 2.6$) and 12 ± 3 per cent ($D = 3.0$). The high-mass unbound fractions are only different for simulations with higher ($D \leq 2.0$) and no initial substructure ($D = 3.0$).

In regions with initial fractal dimensions $D = 2.0$-3.0, high-mass stars do not become unbound early in the simulations. The collapse happens fastest in initially highly substructured star-forming regions ($D = 1.6$) and high-mass stars can become unbound much earlier than in less substructured star-forming regions. The lower the level of initial substructure, the longer it takes to form dynamical multiples that can eject high-mass stars (Allison & Goodwin 2011). Our simulations suggest that it can take over 3 Myr longer for high-mass stars to become unbound when there is a lack of initial substructure in moderately subvirial initial conditions (lower, middle panels).

In all simulations that are initially virialized ($\alpha_{vir} = 0.5$, third column), regardless of substructure, the unbound fraction of low/intermediate-mass stars is at least double the fraction of unbound high-mass stars after 10 Myr, which reaches 16 ± 3 per cent in initially highly substructured regions ($D = 1.6$). In these star-forming regions, 37 ± 3 per cent of all low/intermediate-mass stars become unbound at the end of our simulations.

Initially virialized, highly substructured star-forming regions can collapse locally and binary clusters can form (Arnold et al. 2017). Binary clusters are a pairing of star clusters that are physically close to each other in space (Rozhavskii, Kuz'mina & Vasilevskii 1976; Pietrzynski & Udalski 2000; de La Fuente Marcos & de La Fuente Marcos 2009; Priyatikanto et al. 2016; Zhong et al. 2019). They can be a result of the dynamical evolution of young star-forming regions as shown by Arnold et al. (2017). We see these binary clusters at the end of more than half of the 20 simulations and they appear to have an effect on the unbound fractions. The presence of binary clusters lowers the subcluster potential energy, effectively creating two smaller clusters with smaller potential wells. In consequence, stars require lower kinetic energy to become unbound. This increases the low/intermediate-mass unbound fraction, but does not affect the high-mass unbound fraction in the same way. Due to the form of the IMF, there is a much smaller number of high-mass stars present in our simulations. During the localized collapse into binary clusters, these high-mass stars can move to different local regions, reducing the likelihood of creating dynamical multiple systems that can eject high-mass stars from our regions.

We do find a higher unbound fraction for high-mass stars than low/intermediate-mass stars in several simulations with initially virialized, highly substructured conditions ($\alpha_{vir} = 0.5$, $D = 1.6$) that do not result in the creation of binary clusters. In individual simulations where binary clusters are present, we see a higher than average fraction (∼30 per cent compared to the average value of ∼16 per cent) of unbound high-mass stars when the low/intermediate-mass unbound fraction is high as well (∼40–70 per cent) or when the absolute number of high-mass stars is high to begin with (i.e. nine or more high-mass stars per simulation). This increases the chances of forming high-mass dynamical multiple systems, which would lead to more ejections.

Lower levels of initial substructure or smooth regions ($D = 2.0$–3.0) that are initially virialized ($\alpha_{vir} = 0.5$) do not form binary

Downloaded from https://academic.oup.com/mnras/article-abstract/487/4/4615/5509598 by University of Sheffield user on 20 August 2019

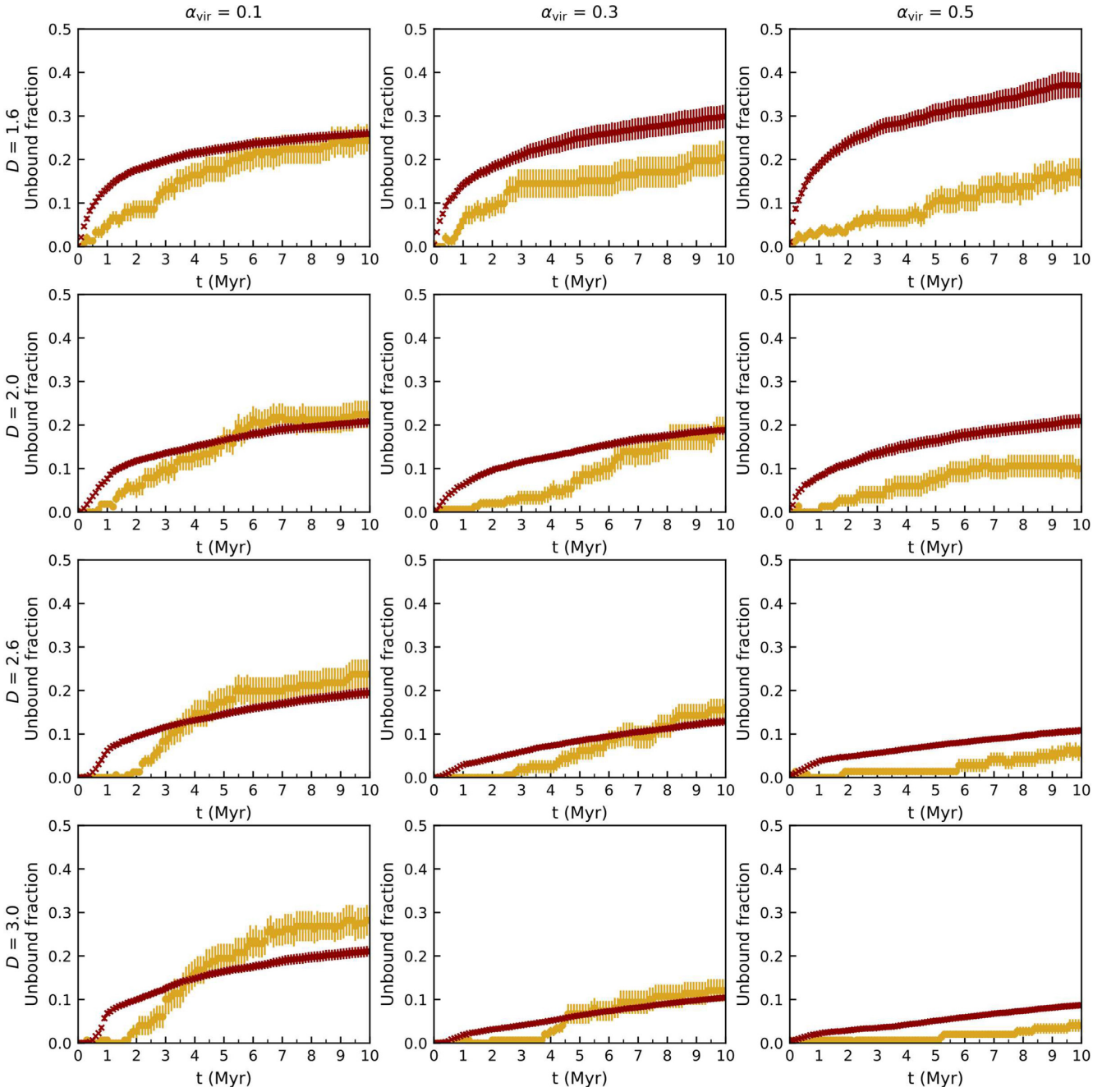

Figure 4. Unbound fractions by mass class for initially subvirial and virialized star-forming regions ($\alpha_{vir} \leq 0.5$). Each row represents a different fractal dimension starting from $D = 1.6$ (top row) to $D = 3.0$ (bottom row). The columns show the three subvirial and virial initial ratios. The red points represent the unbound fraction of low/intermediate-mass stars ($<8\,M_{\odot}$) over the simulation time, whereas the yellow points represent the unbound fraction of high-mass stars ($>8\,M_{\odot}$). The uncertainties of the fractions are calculated using the standard error of the mean (equation 5).

clusters (Arnold et al. 2017). In our simulations, this considerably reduces the unbound fractions. Star-forming regions that are initially in virial equilibrium and smooth ($D = 3.0$) undergo very little dynamical evolution and most of the stars (~87 per cent) remain bound throughout the simulations.

3.2.2 Effects of different initial virial ratios in regions with the same levels of substructure

For star-forming regions with a high degree of initial substructure ($D = 1.6$, first row in Fig. 4), increasing the initial virial ratio has the opposite effect on the unbound fractions in the two mass classes. The increase in initial kinetic energy (higher virial ratio) in the regions decreases the fraction of unbound high-mass stars, whereas it increases the fraction of low/intermediate-mass unbound stars. While an initially highly subvirial region ($\alpha_{vir} = 0.1$) has the same unbound fraction after 10 Myr in both mass classes, the more virialized a highly substructured region is initially the higher its unbound fraction of low/intermediate-mass stars and the lower its high-mass unbound fraction. The low/intermediate-mass unbound fraction is highest in initially virialized regions due to the presence of binary clusters.

Downloaded from https://academic.oup.com/mnras/article-abstract/487/4/4615/5509598 by University of Sheffield user on 20 August 2019

In regions with a lower level of initial substructure ($D = 2.0$, second row), differences in initial virial ratio have no effect on the low/intermediate-mass unbound fractions, which are virtually the same for all three initial virial ratio scenarios (values between 19 ± 1 per cent and 21 ± 2 per cent) at 10 Myr. The high-mass unbound fraction is highest in the initially most subvirial regions ($\alpha_{\rm vir} = 0.1$). The degree of collapse is highest here and unstable multiple star systems can form quickly. After about 6 Myr, the high-mass unbound fraction reaches 21 ± 3 per cent and starts to level out (22 ± 3 per cent at 10 Myr), suggesting that unstable multiple star systems are no longer present or do not lead to any further high-mass star ejections. The initially more moderate, subvirial ($\alpha_{\rm vir} = 0.3$) simulations have a similar high-mass unbound fraction than the virialized case in the first ~6 Myr of the simulations (10 ± 2 per cent versus 9 ± 2 per cent). The difference in initial virial ratio ($\alpha_{\rm vir} = 0.3$ versus 0.5) appears to have no effect on the early evolution of these simulated regions. Later in the simulation, the initially moderately subvirial ($\alpha_{\rm vir} = 0.3$) regions continue to eject high-mass stars and reach an unbound fraction of 19 ± 3 per cent after 10 Myr, which is a similar value than in the highly subvirial case ($\alpha_{\rm vir} = 0.1$), whereas the high-mass unbound fraction in initially virialized regions levels out after ~7 Myr and remains at 10 ± 2 per cent to the end of the simulations at 10 Myr.

At low levels of or no initial substructure ($D = 2.6$ and 3.0, third and fourth row), the low/intermediate-mass unbound fractions are highest when the regions are initially highly subvirial ($\alpha_{\rm vir} = 0.1$) as these regions collapse initially. Even though the moderately subvirial ($\alpha_{\rm vir} = 0.3$) regions initially collapse, this does not result in a higher low/intermediate unbound fraction than in the initially virialized regions that do not undergo collapse. When there is little or no initial substructure, star-forming regions will only collapse when the initial virial ratio is subvirial. The collapse increases the likelihood that unstable multiple systems form, which facilitates the ejection of high-mass stars. With higher initial virial ratios, these multiple systems take longer to form or do not form at all. As a result, high-mass stars take longer to become unbound and the final unbound fractions at 10 Myr are lower the more virialized and smooth the regions are initially.

3.3 2D-velocity of unbound stars from initially subvirial and virialized star-forming regions

3.3.1 Cumulative 2D-velocity distributions

In Fig. 5, we show the 2D-velocity cumulative distributions for unbound stars from initially subvirial/virialized regions ($\alpha_{\rm vir} \leq 0.5$) with a high level of initial substructure ($D = 1.6$) at 10 Myr. As we have seen for all (bound and unbound) stars in Fig. 2, the cumulative distributions in initially subvirial/virialized simulations are very similar for all four initial fractal dimensions. The cumulative distributions of unbound stars in Fig. 5 show a similar picture of very similar distributions for a fractal dimension of $D = 1.6$ (initially highly substructured regions). Even for these initially substructured regions where we see a more dynamic early evolution (i.e. violent relaxation and initial collapse), it is difficult to distinguish between different initial virial ratios at the end of the simulations.

Allison (2012) analysed the spatial and velocity distributions of very different initial conditions after 4 Myr with a smaller, but similar, set of initial conditions. He found that the cumulative velocity distributions differ between the initial conditions and that the initially moderately subvirial, substructured simulations result in higher velocity unbound stars compared with initially virialized simulations with a low level of substructure. Fig. 6 illustrates the cumulative velocity distributions of very different initial conditions after 10 Myr: initially highly substructured and highly subvirial simulations ($D = 1.6$; $\alpha_{\rm vir} = 0.1$; blue) compared to simulations with a low level of substructure that are initially virialized ($D = 2.6$; $\alpha_{\rm vir} = 0.5$; green). We also find that unbound stars from substructured, subvirial regions are moving at higher 2D-velocities (after 10 Myr), however, the differences between the distributions are not quite as large as in Allison (2012). This highlights that cumulative velocity distributions can only distinguish between vastly different initial spatial and velocity conditions.

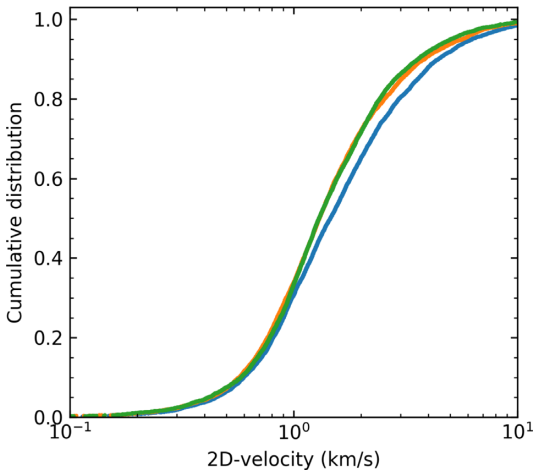

Figure 5. Cumulative distributions for unbound stars showing the 2D-velocities at 10 Myr with initial fractal dimension $D = 1.6$ for initially subvirial and virialized clusters. The distributions for $\alpha_{\rm vir} = 0.1$ (blue), $\alpha_{\rm vir} = 0.3$ (orange), and $\alpha_{\rm vir} = 0.5$ (green) are shown zoomed-in to the central part of the curve, highlighting that for these initial conditions, the velocities of the unbound stars do not differ much between different virial ratios for the same degree of initial spatial and kinematic substructure.

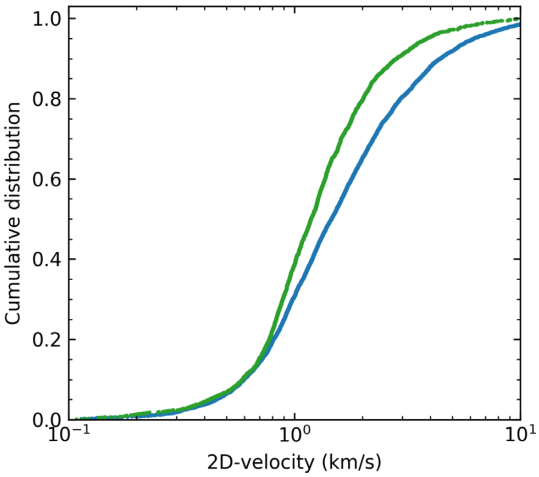

Figure 6. Cumulative distributions for unbound stars showing the 2D-velocities at 10 Myr for an initially highly substructured and subvirial region with $D = 1.6$ and $\alpha_{\rm vir} = 0.1$ (blue) and an initially almost smooth and virialized region with $D = 2.6$ and $\alpha_{\rm vir} = 0.5$ (green). The comparison illustrates that the more substructured and subvirial a star-forming region is initially, the faster the unbound stars escape.

Downloaded from https://academic.oup.com/mnras/article-abstract/487/4/4615/5509598 by University of Sheffield user on 20 August 2019

3.3.2 *Violin plots of 2D-velocity distributions*

Violin plots are a data visualization technique that combines a box plot with a density trace or a kernel density estimate (Hintze & Nelson 1998). Like box plots, violin plots also show the median and interquartile range for a variable, as well as any asymmetries and outlier data. They can be useful when comparing distributions of a variable (2D-velocity) over different categories (initial conditions for star-forming regions). Unlike box plots, violin plots include all data from the underlying distribution and give information about the shape of the distribution. They show all peaks and the position of those peaks, their amplitude, and give insight into any presence of clustering in the data. The outer shape represents all data, with the widest parts corresponding to the value (i.e. 2D-velocity) with the highest probability of occurring in the population (Hintze & Nelson 1998), which can be also interpreted as the most common 2D-velocity in our case.

Fig. 7 shows the 2D-velocity distributions on a log scale for all initially subvirial and virialized regions (left to right) and all four fractal dimensions (decreasing degree of initial substructure – top to bottom) after 10 Myr. The plots include all unbound stars from 20 simulations combined and represent an average. The wider each of the violin plots is at any point, the more stars are likely to have this 2D-velocity. For each fractal dimension (in each row), the width of the violin plot is scaled by the total number of unbound stars for this initial virial ratio. For two violin plots with the same total number of unbound stars, the widest part will have the same width. However, the absolute number of stars with this velocity can be different, e.g. for fractal dimension $D = 2.0$ (second row) the blue ($\alpha_{\rm vir} = 0.1$) and green ($\alpha_{\rm vir} = 0.5$) violin plots both contain a total of ∼4100 unbound stars from 20 simulations each, resulting in the widest part of their violin plots having the same width in Fig. 7. Due to difference in the distributions, there are ∼80 more stars at the most common velocity for the initially virialized (green) violin plot.

The thick vertical bar in the centre represents the interquartile range with the white dot representing the median. The thin long vertical line represents the 95 confidence interval. We use a bandwidth following the Silverman (1986) reference rule to smooth our data for the violin plots.[1] The violin plots are cut at the low-velocity end and only show the actual data points there, instead of the tails of the underlying Gaussian kernel density estimate. This allows us to identify the lowest actual 2D-velocity directly from the plot and avoids the appearance of negative 2D-velocities.

Initially, highly substructured regions ($D = 1.6$; Fig. 7 first row) have a large number of unbound stars for all three initial virial ratios. The fastest stars are ejected from initially highly subvirial regions ($\alpha_{\rm vir} = 0.1$, blue) with the peak velocity reaching ∼70 km s^{-1}. These regions have fewer unbound stars (∼260 per simulation) in total and fewer stars at similar velocities with a wider spread of velocities around ∼1 km s^{-1} compared to the two higher virial ratio scenarios. Despite these differences, the median velocity is similar (∼1.5 km s^{-1}) to the other two scenarios (∼1.3 km s^{-1} – both for $\alpha_{\rm vir} = 0.3$ and 0.5). A large number of unbound stars from highly substructured, moderately subvirial regions ($\alpha_{\rm vir} = 0.3$, orange) move at a similar 2D-velocity of ∼1 km s^{-1} after 10 Myr, creating noticeable arms in the violin plots. The total number of unbound stars increases to ∼300 per simulation. The arms become most pronounced in the initially virialized case ($\alpha_{\rm vir} = 0.5$, green) with ∼370 unbound stars per simulation. Despite the increase in the total number of unbound stars, the most common velocity remains around ∼1 km s^{-1}. The higher the initial virial ratio in initially highly substructured regions, the more likely it is that unbound stars are moving with more similar velocities, whereas unbound stars are more evenly spread over different velocities in initially more subvirial regions.

With a lower level of initial substructure ($D = 2.0$, second row), the shape of the distributions changes for all three initial virial ratios. The shape of the velocity distributions of the two initially subvirial scenarios ($\alpha_{\rm vir} < 0.5$) is now almost identical. The violin plot for highly subvirial regions is wider than the moderately subvirial scenario, meaning more stars become unbound (20 more stars per simulation). We see the pronounced arms in the violin plots now also for highly subvirial regions with less spread in the 2D-velocities. The fastest stars from the two subvirial regions now only reach ∼30 km s^{-1} and their median velocities are almost identical (∼1.3 km s^{-1}). In initially virialized regions ($\alpha_{\rm vir} = 0.5$, green), the arms in the 2D-velocity become even more pronounced at ∼1 km s^{-1}. The maximum velocity is lower (∼13 km s^{-1}) than in the subvirial cases (∼30 km s^{-1}), however, the median velocity remains similar (∼1.2 km s^{-1}).

In regions with little or no initial substructure ($D \geq 2.6$, third and fourth row), initially highly subvirial regions ($\alpha_{\rm vir} = 0.1$) show a similar violin shape to the more substructured regions ($D = 2.0$) and also have a similar number of unbound stars (∼200–210 per simulation). The sizes of the violins shrink considerably (i.e. fewer unbound stars) for initially moderately subvirial ($\alpha_{\rm vir} = 0.3$) and virialized ($\alpha_{\rm vir} = 0.5$) regions and we see ∼90–130 unbound stars per simulation. This indicates a much less dynamical early evolution with the number of unbound stars only ∼30 per cent of what they are in simulations with the highest level of initial substructure. Despite this, the violins retain their overall familiar shape of having arms around the most common velocity of ∼1 km s^{-1} and a median velocity (∼1.2–1.3 km s^{-1}), which is similar to all other initial conditions.

Our unbound definition is based on stars reaching the escape velocity (total positive energy) from the star-forming regions, which is ∼3 km s^{-1} in our simulated regions. In Fig. 7, we see that the minimum 2D-velocity of unbound stars can be as low as ∼0.03 km s^{-1} after 10 Myr. Once unbound stars leave the denser parts of a star-forming region, they interact with fewer or no other stars and slow down gradually. However, the apparent slowdown in our simulations by up to two orders of magnitude is likely due to projection effects. Fig. 8 shows violin plots for two, very different initial conditions (blue – initially highly subvirial, substructured, and green – initially virialized, no substructure) at three different times during the simulations. Already after 1 Myr, a low-velocity tail forms in 2D-space that extends to velocities an order of magnitude lower than the escape velocity. In full 3D-velocity space in Fig. 9, we see that after 1 Myr the lowest velocities are only 1–2 km s^{-1} lower than the escape velocity. This suggests that unbound stars slow down, however, not to the extent suggested by the 2D-velocities.

This 2D-projection effect could affect cluster membership identification when observing proper motion (or 1D-radial velocity) in isolation. Depending on relative position to the cluster, these 'slow' unbound stars could be identified as not having originated from the cluster at all due to being too far away or still bound due to their central location in the star-forming region. However, our simulations suggest that only ∼1 per cent of these unbound stars with low 2D-velocities are located in the central parts of star-forming regions after 10 Myr. This limits the extent of mistakenly assigning membership

[1] https://seaborn.pydata.org/generated/seaborn.violinplot.html

Downloaded from https://academic.oup.com/mnras/article-abstract/487/4/4615/5509598 by University of Sheffield user on 20 August 2019

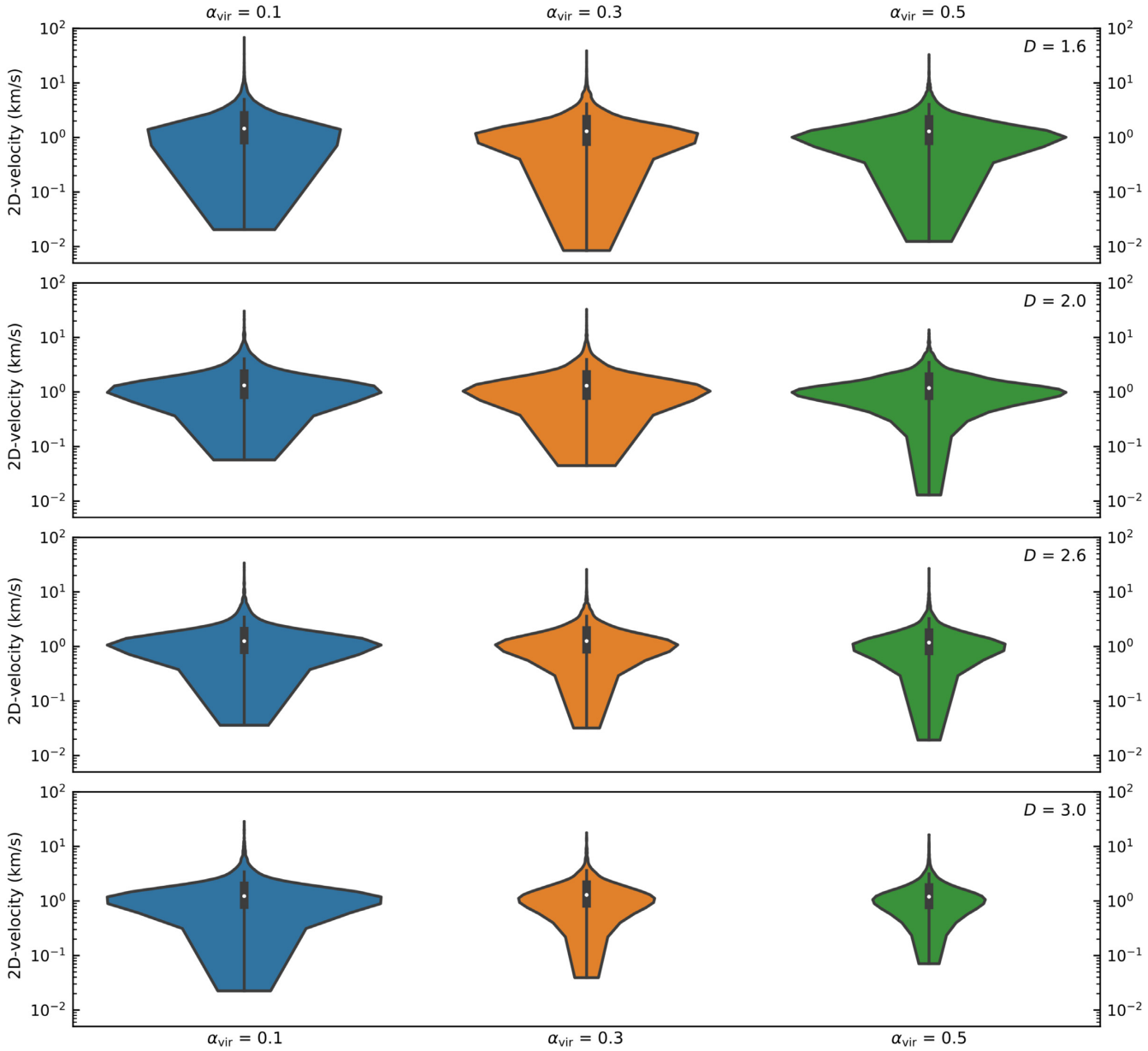

Figure 7. Violin plots showing the 2D-velocity distributions of unbound stars at 10 Myr from all initially subvirial and virialized regions [$\alpha_{vir} = 0.1$ (blue), $\alpha_{vir} = 0.3$ (orange)] and virialized [$\alpha_{vir} = 0.5$ (green)]. The violins are scaled by count; the wider the violins are at any point the more stars in our regions have this 2D-velocity. The larger the violins overall, the more stars have become unbound during the simulation time. The thick vertical bar in the centre shows the interquartile range with the white dot representing the median. The long vertical line represents the 95 per cent confidence interval.

to 'slow' unbound stars, when only proper motion information is available.

In Fig. 10, we use split violin plots to show the 2D-velocities separately for the two mass classes. The plots are now scaled to the same width as we have at most ∼40 unbound high-mass stars compared with over 7000 lower-mass unbound stars from a set of 20 simulations. The widest part of each half still represents the 2D-velocity with the highest probability of occurring. The dashed lines represent the median and the interquartile range, the 95 per cent confidence interval is no longer identified on the plots. The violin plots are again cut at the low-velocity end and only show the actual data points, instead of the tails of the underlying Gaussian kernel density estimate. This allows us to identify the lowest actual 2D-velocity directly from the plot and avoids the appearance of negative 2D-velocities.

In Fig. 10, we see that the shape of the low/intermediate-mass violins is nearly identical to the shape of the total population of unbound stars in Fig. 7 as most unbound stars are lower mass. Due to the low number of unbound high-mass stars, the velocity distributions of unbound high-mass stars can have a jagged outline depending on the bandwidth used. We use the same bandwidth setting (following Silverman 1986) as in Fig. 7 resulting in the right half (unbound high-mass stars) of our split violin plots in Fig. 10 appearing as a smooth distribution despite the small sample size. A small sample size can make conclusions from violin plots unreliable and we limit our interpretation of them to

Downloaded from https://academic.oup.com/mnras/article-abstract/487/4/4615/5509598 by University of Sheffield user on 20 August 2019

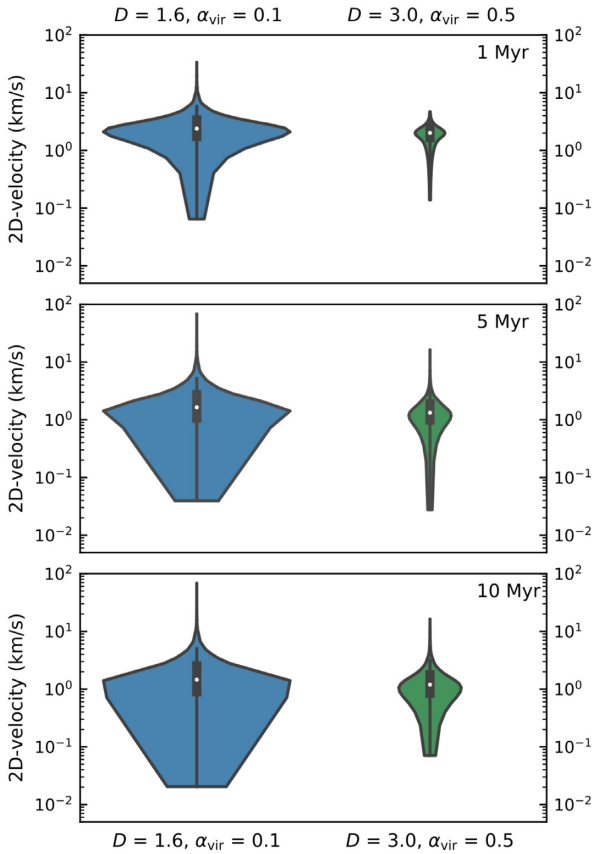

Figure 8. Violin plots showing 2D-velocity (*xy*-plane) distributions of unbound stars at three simulation times for two selected initial conditions [initially subvirial, substructured (blue) and initially virialized with no substructure (green)].

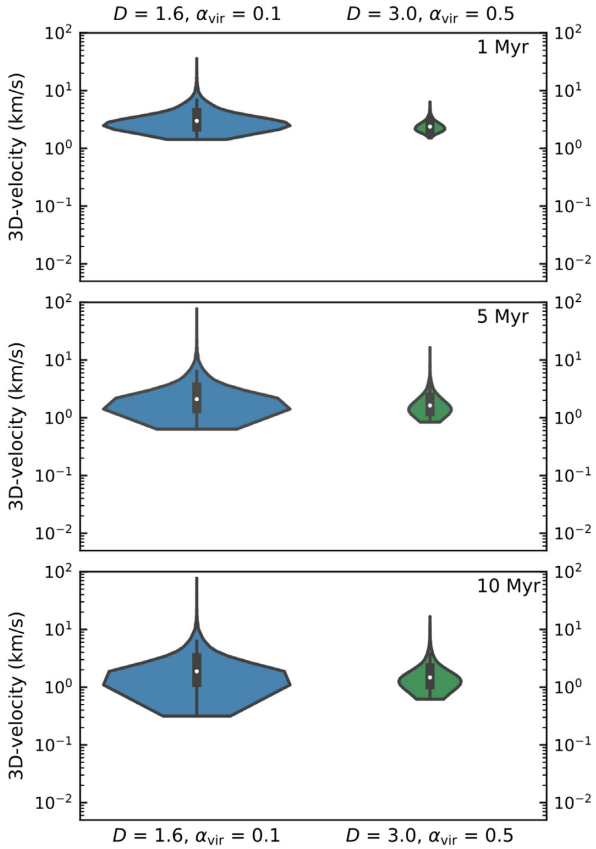

Figure 9. Violin plots showing 3D-velocity distributions of unbound stars at three simulation times for two selected initial conditions [initially subvirial, substructured (blue) and initially virialized with no substructure (green)].

general differences in median, minimum, and maximum velocity between the two mass classes. To gain more insight into the velocity distributions of unbound high-mass stars using violin plots would require an increase in the sample size, i.e. a much higher number of simulations.

For all initial condition scenarios at 10 Myr, high-mass unbound stars have a higher median (and interquartile range) than the low/intermediate-mass stars and also a much higher minimum 2D-velocity. The mechanism for high-mass stars to become unbound is different to that of low/intermediate-mass stars. High-mass stars will only become unbound from our star-forming regions after a dynamical interaction with other massive stars in multiples. These dynamical interactions make unbound high-mass stars move faster on average, however, the fastest stars are in fact from the low-mass end. The differences in 2D-velocities between the mass classes are present in all initial condition combinations, so is not affected by the initial spatial or velocity structure in the star-forming regions.

3.4 Runaway and walkaway stars

Finally, we analyse how effective star-forming regions with different initial conditions are at ejecting runaway and walkaway stars. We only use 2D-velocity and the lower boundary value of 30 km s^{-1} (e.g. Blaauw 1956; Stone 1991; de Wit et al. 2005; Eldridge et al. 2011) for our runaway definition and velocities between 5 and 30 km s^{-1} for walkaways (Eldridge et al. 2011; de Mink et al. 2014).

Fig. 11 shows all stars from 20 simulations per initial condition moving with a 2D-velocity (*xy*-plane) above 30 km s^{-1}. All of them are from the low end of the mass spectrum, not a single runaway star is more massive than 0.5 M$_\odot$. We have the highest number of runaway stars from initially highly substructured, subvirial regions ($\alpha_{\rm vir} = 0.1$, $D = 1.6$) regardless of the choice of 2D-plane. Only the fastest one is present in all three 2D-planes and is moving with a 2D-velocity between 50 and 70 km s^{-1} depending on the choice of plane. The other two runaways have lower velocities between 30 and 40 km s^{-1}. With at most three ejected runaways from a set of 20 simulations, we see that regardless of the initial velocity or spatial structure, runaway stars are rare from our chosen initial conditions.

Going to walkaway velocities (5–30 km s^{-1}) produces a few high-mass walkaways and a large number of low-mass walkaways across all initial conditions. Fig. 12 shows all walkaways from the 20 simulations across each initial condition set. The more violent the early evolution of a star-forming region is, the higher the number of walkaway stars. In the most violently evolving initial condition set-up – initially highly substructured ($D = 1.6$) and highly subvirial ($\alpha_{\rm vir} = 0.1$), we have on average ∼0.5 high-mass walkaways per simulation and ∼20 low/intermediate-mass walkaways per simulation.

The lower the initial level of substructure (larger fractal dimension D), the lower the overall number of walkaway stars, with initially more subvirial regions (Fig. 12 top row) producing more

Downloaded from https://academic.oup.com/mnras/article-abstract/487/4/4615/5509598 by University of Sheffield user on 20 August 2019

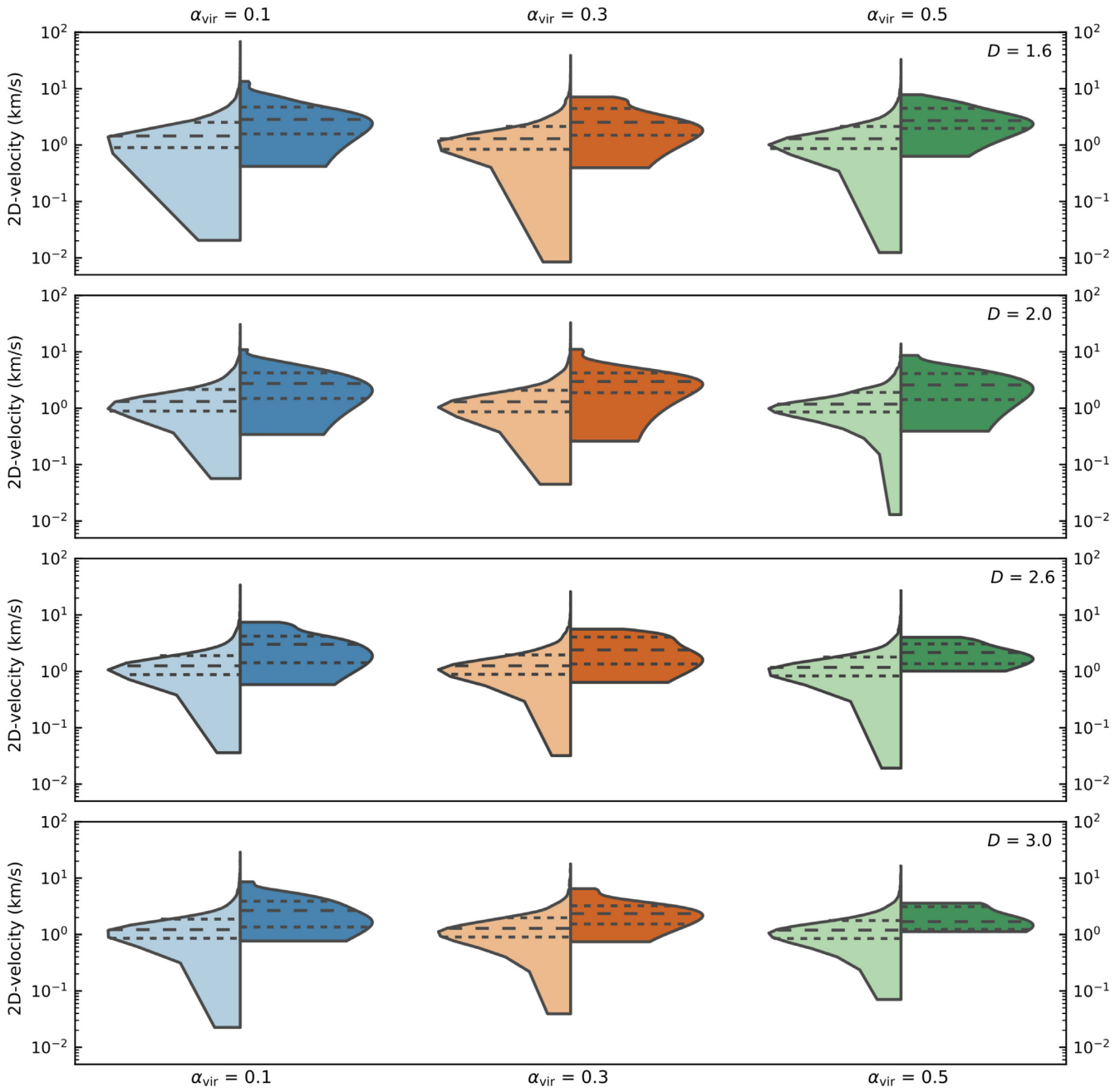

Figure 10. Violin plots showing the 2D-velocity distributions of unbound stars at 10 Myr split by mass class [low/intermediate-mass – left half, high-mass – right half) from all initially subvirial and virialized clusters ($\alpha_{vir} = 0.1$ (blue), $\alpha_{vir} = 0.3$ (orange)] and virialized [$\alpha_{vir} = 0.5$ (green)]. All plots are scaled to have the same width as there is only a very small number of unbound high-mass stars. The widest part of the each violin half represents the 2D-velocity with the highest probability. The dashed lines represent the median and the interquartile range; the 95 per cent confidence interval is no longer shown.

walkaway stars, which are also ejected earlier in the simulations. We see a number of temporary walkaways that appear as walkaways only for a few snapshots. These are stars ejected just at the minimum walkaway velocity. After ejection, they slow down and disappear from our plots once they drop below 5 km s^{-1} (minimum walkaway velocity), however, this does not mean that they have been recaptured by the star-forming region. Initially virialized star-forming regions with no substructure ($\alpha_{vir} = 0.5$, $D = 3.0$ – bottom right-hand panel) produce on average only two low/intermediate-mass walkaways per simulation. This is an order of magnitude fewer walkaway stars than in the initial condition scenario [initially highly substructured ($D = 1.6$), highly subvirial ($\alpha_{vir} = 0.1$) – top left-hand panel] that produces the largest number of walkaway stars.

4 DISCUSSION

We summarize the results of our *N*-body simulations as follows. Cumulative velocity distributions of star-forming regions with different initial conditions have limited usefulness in clearly distinguishing between different initial spatial and velocity structure.

Downloaded from https://academic.oup.com/mnras/article-abstract/487/4/4615/5509598 by University of Sheffield user on 20 August 2019

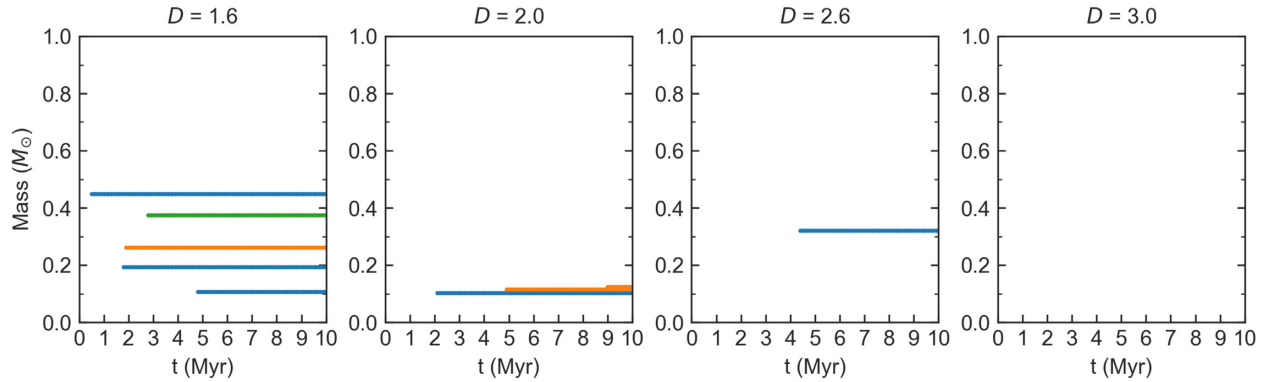

Figure 11. Runaway stars (2D-velocity $> 30\,\mathrm{km\,s^{-1}}$) by mass over the simulation time for the four fractal dimensions and the three different initial virial ratios: subvirial [$\alpha_{\mathrm{vir}} = 0.1$ (blue) and $\alpha_{\mathrm{vir}} = 0.3$ (orange)] and virialized [$\alpha_{\mathrm{vir}} = 0.5$ (green)]. The y-axis is limited to $1\,\mathrm{M}_\odot$, as all of our runaway stars have very low mass.

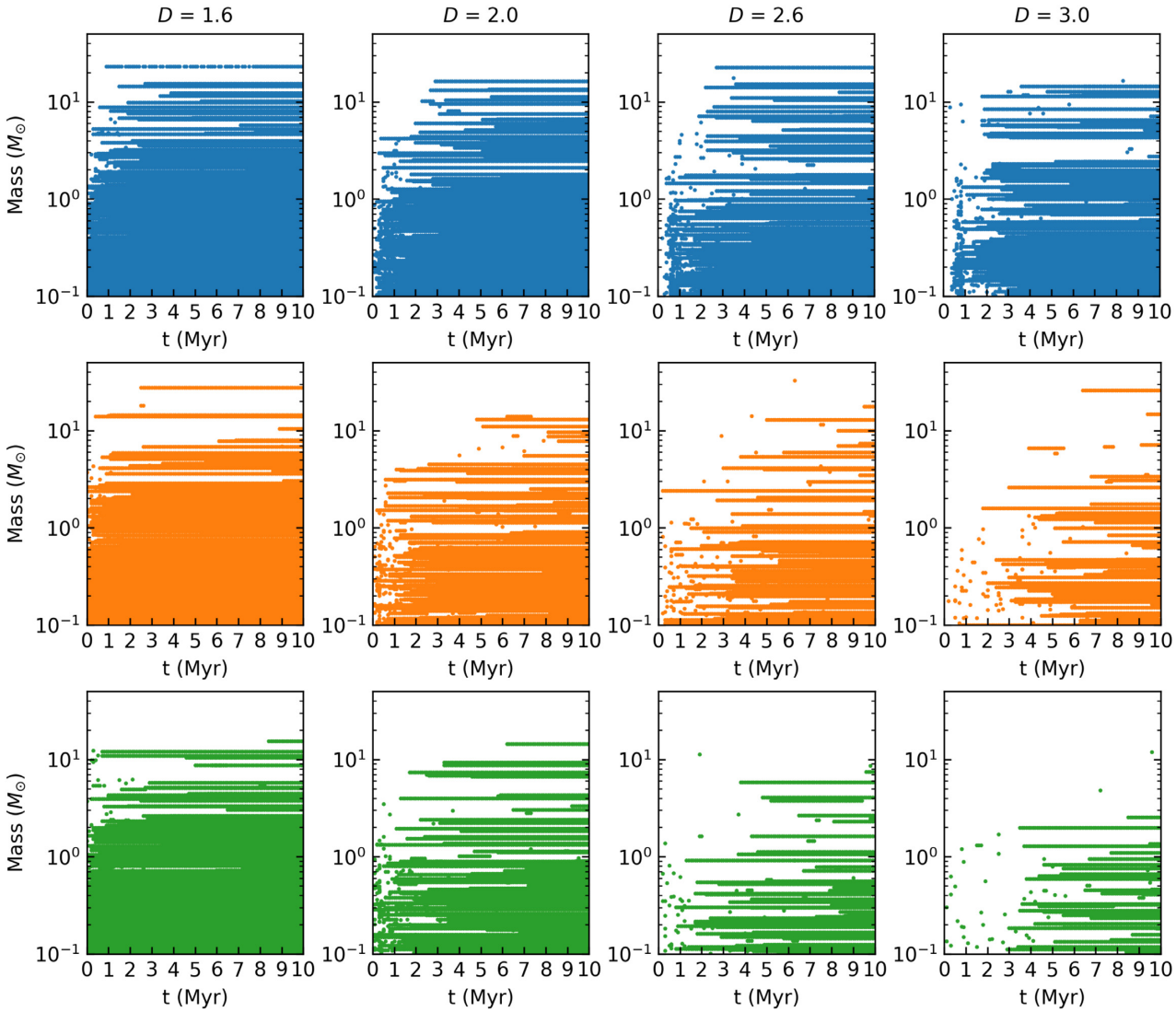

Figure 12. Walkaway stars (2D-velocity: 5–$30\,\mathrm{km\,s^{-1}}$) by mass (using a log scale) over the simulation time for the four fractal dimensions and the three different initial virial ratios: subvirial [$\alpha_{\mathrm{vir}} = 0.1$ (blue, top row) and $\alpha_{\mathrm{vir}} = 0.3$ (orange, middle row)] and virialized [$\alpha_{\mathrm{vir}} = 0.5$ (green, bottom row)]. A few stars (the single points) are only identified as walkaways for a few snapshots; this is due to them being ejected close to the lower walkaway velocity boundary and slowing down to fall below the boundary shortly after ejection.

Downloaded from https://academic.oup.com/mnras/article-abstract/487/4/4615/5509598 by University of Sheffield user on 20 August 2019

When comparing the long-term evolution of regions with different levels of initial substructure, regions with high levels of initial substructure evolve very quickly kinematically, with supervirial regions (unbound by definition) showing the fastest 2D-velocities. The cumulative velocity distributions of unbound stars from initially subvirial and virialized simulations are difficult to distinguish after 10 Myr and only show differences for extremely different initial conditions (see Fig. 6).

The unbound fraction differs considerably for different combinations of initial spatial and velocity structure. This suggests that the unbound population around young, bound star clusters could possibly be used to draw conclusions about the initial conditions. Around initially smooth ($D = 3.0$), virialized ($\alpha_{\rm vir} = 0.5$) star-forming regions, we find a low number of ejected stars (slow walkaways, but no runaways) and virtually no unbound high-mass stars after 10 Myr. Around initially substructured, subvirial regions that have undergone violent relaxation, we find a large number of unbound low/intermediate-mass stars. We also find a few high-mass ejected stars (at walkaway velocities) and one low-mass runaway star in 3 of the 20 simulations. The unbound fractions are possibly influenced by our choice of initial density as higher densities increase the likelihood of encountering and interacting with other stars.

Initial densities can differ greatly from those currently observed due to the amount of dynamical evolution that a region undergoes. The level of spatial substructure in a region can constrain the dynamical evolution of regions with different initial densities – the higher the initial density, the quicker substructure is erased (Parker 2014). Our simulated star-forming regions have been set up with a high, median local initial density (10^3–10^4 $M_\odot$ pc^{-3}).

After about 1 Myr, regions with initial spatial substructure have evolved into smooth, centrally concentrated regions, whose densities can be directly compared to observed star-forming regions. The density in our simulations after a few Myr is 10^1–10^3 $M_\odot$ pc^{-3} (Parker 2014) comparable to many nearby star-forming regions where observed present-day densities do not exceed $\sim$400 $M_\odot$ pc^{-3} (e.g. Marks & Kroupa 2012).

High-mass stars are less likely to become unbound than low/intermediate-mass stars if a region is not initially very subvirial. When they do escape from their birth environment they do so at higher average velocity and often become walkaway stars (>5 km s^{-1}). With our chosen initial conditions, high-mass stars do not reach the velocity regime of runaway stars. Only the evolution of star-forming regions that are initially subvirial ($\alpha_{\rm vir} < 0.5$) and/or substructured ($D \leq 2.0$) is dynamic enough to produce any runaway stars, all of which are low mass. This is in apparent contrast to observations, where due to observational bias, predominantly high-mass runaways are found (Tetzlaff et al. 2011) as they are more luminous and easier to observe. Historically, the definition of runaway stars is based on OB stars (Blaauw 1961), following Tetzlaff et al. (2011), we suggest to extend this definition to lower mass stars. Lower mass stars appear to reach runaway velocities more often than higher mass stars and these could be found around many young star-forming regions when testing our predictions with *Gaia* DR2 (Gaia Collaboration 2018).

Using data from *Gaia* DR1 (Gaia Collaboration 2016), Wareing et al. (2018) report that two of the most massive stars (HD46223 and HD46106) in NGC2244 are moving away from each other and from the centre of this young cluster at a larger velocity than the other cluster stars. They suggest that HD46223 has been ejected from the cluster, possibly due to dynamical interactions with other massive stars in the centre. The inferred velocity of 1.38 km s^{-1} from its proper motion (Wareing et al. 2018) is far below the lower velocity boundary for walkway stars and it is unclear if this star is actually unbound. Our simulated star-forming regions (1000 single stars) have an escape velocity of $\sim$3 km s^{-1}. NGC2244 is estimated to have $\sim$2000 members (Wang et al. 2008) suggesting that HD46223 might not have reached escape velocity and might still be bound to the cluster despite its apparent ejection. In our simulations, we also see massive stars moving outwards after dynamical interactions at velocities higher than their surroundings. If they are moving more slowly than the escape velocity, they will remain bound to the cluster, slow down, and eventually return in direction of the cluster centre.

Violin plots show that the velocity distributions do indeed differ between initial conditions, particularly when the regions are initially highly substructured. These distributions also indicate that the vast majority of low/intermediate-mass stars become unbound at just around the escape velocity. We show that 2D-velocity information appears to be an underestimate of the full 3D-velocity for a proportion of unbound stars. This can have implications for membership determination of young star-forming regions, where full velocity parameter space information is not available. The *Gaia* DR2 data set (Gaia Collaboration 2018) contains a much larger number of stars only with proper motion data, missing information about the radial velocity for many fainter stars. If the 2D-velocity is indeed an underestimate of the full space velocity for some stars, we might mistakenly assign a cluster membership to stars with slow proper motions or not be able to trace back stars to their birth cluster.

Escaping, ejected, or unbound stars from simulations have been studied previously (e.g. Fujii & Portegies Zwart 2011; Weidner, Bonnell & Moeckel 2011; Allison 2012; Moyano Loyola & Hurley 2013; Oh & Kroupa 2016; Wang, Kroupa & Jerabkova 2019). Allison (2012) found a similar connection between unbound stars (i.e. number, velocity, spatial distribution) and the initial substructure and virial ratio with a more limited set of initial conditions. Other studies (Weidner et al. 2011; Oh & Kroupa 2016) used Plummer spheres (Plummer 1911) to set up the initial spatial distribution of the clusters and included primordial binaries. The conclusion from these studies was that the number and mass fraction of unbound stars depend strongly on the initial cluster radius or initial density and to a lesser extent on the parameters of the primordial binaries (Weidner et al. 2011; Oh & Kroupa 2016) or the initial virial ratio (Weidner et al. 2011). With their inclusion of primordial binaries, the results of these studies are not directly comparable to ours.

Our results show that differences in the initial spatial and kinematic substructure can have a considerable effect on the fraction, the velocity, and the masses of unbound stars. Due to the lack of stellar evolution in our short simulation time of 10 Myr, we miss the effects of supernova kicks causing stars to become unbound due to the binary supernova ejection mechanism (Blaauw 1961). In our simulations, binaries will only form dynamically (i.e. are not present from the beginning of our simulations) and we may therefore be underestimating the impact of the dynamic ejection mechanism (Poveda et al. 1967) as we only find a few lower mass runaway stars. Moyano Loyola & Hurley (2013) showed that a higher fraction of primordial binaries increases the number of higher velocity (20–100 km s^{-1}) stars.

5 CONCLUSIONS

In this paper, we present *N*-body simulations of star-forming regions set up with a range of different initial spatial and velocity structures. We investigate if the dynamical evolution results in differences in

Downloaded from https://academic.oup.com/mnras/article-abstract/487/4/4615/5509598 by University of Sheffield user on 20 August 2019

the unbound population after 10 Myr. The conclusions from our simulations are summarized as follows:

(i) Cumulative 2D-velocity distributions of all stars in simulated star-forming regions cannot provide strong insights into the long-term evolution of star-forming regions with differing initial spatial and velocity structure. When focusing on unbound stars, clear differences in the cumulative distributions are only found when comparing vastly different initial conditions.

(ii) Unbound fractions of stars of different masses show clear differences between the initial conditions and could prove useful to distinguish between initial spatial and velocity structures. Only when a region is initially very subvirial can we expect to find a higher fraction of unbound high-mass stars than low/intermediate-mass stars in the vicinity of the region.

(iii) If high-mass stars manage to escape their birth region, they are likely to reach at least walkaway velocities. However, based on our simulations, not every young star-forming region will create a high-mass runaway or walkaway star.

(iv) Most low/intermediate-mass stars leave the regions at velocities just above the escape velocity. However, the fastest stars from our simulations are also low/intermediate-mass stars. We see a number of low/intermediate-mass walkaway stars from every initial condition set. This number increases for regions that evolve more dynamically (more initial substructure and lower virial ratio). As a result, we should find at least a small number of these stars around virtually every young and high-density star-forming region. The fact that most observed fast stars are still high mass is very likely due to observational bias/limitations. This changes with *Gaia* DR2 where five-parameter space astrometry for stars down to subsolar mass is already available for star-forming regions nearby (Gaia Collaboration 2018). We will use these data to search for walkaway and runaway stars from young star-forming regions in a future paper.

ACKNOWLEDGEMENTS

CS acknowledges PhD funding from the STFC Centre for Doctoral Training in Data Intensive Science and thanks ESTEC/ESA in Noordwijk, in particular the *Gaia* team, for hosting her as a visiting researcher for 6 months. RJP acknowledges support from the Royal Society in the form of a Dorothy Hodgkin Fellowship.

REFERENCES

Adams F. C., Proszkow E. M., Fatuzzo M., Myers P. C., 2006, ApJ, 641, 504
Allison R. J., 2012, MNRAS, 421, 3338
Allison R. J., Goodwin S. P., 2011, MNRAS, 415, 1967
Allison R. J., Goodwin S. P., Parker R. J., Portegies Zwart S. F., de Grijs R., Kouwenhoven M. B. N., 2009, MNRAS, 395, 1449
Allison R. J., Goodwin S. P., Parker R. J., Portegies Zwart S. F., de Grijs R., 2010, MNRAS, 407, 1098
André P., Di Francesco J., Ward-Thompson D., Inutsuka S. I., Pudritz R. E., Pineda J. E., 2014, in Beuther H., Klessen R. S., Dullemond C. P., Henning T., eds, Protostars and Planets VI. Univ. Arizona Press, Tucson, AZ, p. 27
Arnold B., Goodwin S. P., Griffiths D. W., Parker R. J., 2017, MNRAS, 471, 2498
Baumgardt H., Kroupa P., 2007, MNRAS, 380, 1589
Binney J., Tremaine S., 2008, Galactic Dynamics, 2nd edn. Princeton Univ. Press, Princeton, NJ
Blaauw A., 1956, PASP, 68, 495
Blaauw A., 1961, Bull. Astron. Inst. Neth., 15, 265
Blaauw A., 1964, ARA&A, 2, 213
Bonnell I. A., Smith K. W., Davies M. B., Horne K., 2001, MNRAS, 322, 859
Bonnell I. A., Smith R. J., Clark P. C., Bate M. R., 2011, MNRAS, 410, 2339
Bressert E. et al., 2010, MNRAS, 409, L54
Cartwright A., Whitworth A. P., 2004, MNRAS, 348, 589
Chabrier G., 2005, in Corbelli E., Palla F., Zinnecker H., eds, Astrophysics and Space Science Library Vol. 327, The Initial Mass Function 50 Years Later. Springer, Dordrecht, p. 41
de La Fuente Marcos R., de La Fuente Marcos C., 2009, A&A, 500, L13
de la Fuente Marcos R., de la Fuente Marcos C., 2018, Res. Notes Am. Astron. Soc., 2, 35
de Mink S. E., Sana H., Langer N., Izzard R. G., Schneider F. R. N., 2014, ApJ, 782, 7
de Wit W. J., Testi L., Palla F., Zinnecker H., 2005, A&A, 437, 247
Drew J. E., Herrero A., Mohr-Smith M., Monguió M., Wright N. J., Kupfer T., Napiwotzki R., 2018, MNRAS, 480, 2109
Duchêne G., Lacour S., Moraux E., Goodwin S., Bouvier J., 2018, MNRAS, 478, 1825
Eldridge J. J., Langer N., Tout C. A., 2011, MNRAS, 414, 3501
Fujii M. S., Portegies Zwart S., 2011, Science, 334, 1380
Funato Y., Makino J., Ebisuzaki T., 1992, PASJ, 44, 613
Gaia Collaboration, 2016, A&A, 595, A2
Gaia Collaboration, 2018, A&A, 616, A1
Goodwin S. P., 1997, MNRAS, 284, 785
Goodwin S. P., Bastian N., 2006, MNRAS, 373, 752
Goodwin S. P., Whitworth A. P., 2004, A&A, 413, 929
Gvaramadze V. V., Gualandris A., Portegies Zwart S., 2009, MNRAS, 396, 570
Hintze J. L., Nelson R. D., 1998, Am. Stat., 52, 181
Hoogerwerf R., de Bruijne J. H. J., de Zeeuw P. T., 2001, A&A, 365, 49
Jaehnig K. O., Da Rio N., Tan J. C., 2015, ApJ, 798, 126
Kroupa P., 1995, MNRAS, 277, 1491
Kroupa P., Aarseth S., Hurley J., 2001, MNRAS, 321, 699
Kruijssen J. M. D., 2012, MNRAS, 426, 3008
Lada C. J., Lada E. A., 2003, ARA&A, 41, 57
Lada C. J., Margulis M., Dearborn D., 1984, ApJ, 285, 141
Larson R. B., 1981, MNRAS, 194, 809
Longmore S. N. et al., 2014, in Beuther H., Klessen R. S., Dullemond C. P., Henning T., eds, Protostars and Planets VI. Univ. Arizona Press, Tucson, AZ, p. 291
Lynden-Bell D., 1967, MNRAS, 136, 101
Makino J., Aarseth S. J., 1992, PASJ, 44, 141
Marks M., Kroupa P., 2012, A&A, 543, A8
Maschberger T., 2013, MNRAS, 429, 1725
McMillan S. L. W., Vesperini E., Portegies Zwart S. F., 2007, ApJ, 655, L45
Moeckel N., Bonnell I. A., 2009, MNRAS, 400, 657
Moyano Loyola G. R. I., Hurley J. R., 2013, MNRAS, 434, 2509
Nicholson R. B., Parker R. J., Church R. P., Davies M. B., Fearon N. M., Walton S. R. J., 2019, MNRAS, 485, 4893
Oh S., Kroupa P., 2016, A&A, 590, A107
Parker R. J., 2014, MNRAS, 445, 4037
Parker R. J., Goodwin S. P., 2012, MNRAS, 424, 272
Parker R. J., Quanz S. P., 2012, MNRAS, 419, 2448
Parker R. J., Wright N. J., 2016, MNRAS, 457, 3430
Parker R. J., Wright N. J., Goodwin S. P., Meyer M. R., 2014, MNRAS, 438, 620
Parker R. J., Goodwin S. P., Wright N. J., Meyer M. R., Quanz S. P., 2016, MNRAS, 459, L119
Park S.-M., Goodwin S. P., Kim S. S., 2018, MNRAS, 478, 183
Pietrzynski G., Udalski A., 2000, Acta Astron., 50, 355
Plummer H. C., 1911, MNRAS, 71, 460
Portegies Zwart S. F., Makino J., McMillan S. L. W., Hut P., 1999, A&A, 348, 117
Portegies Zwart S. F., McMillan S. L. W., Hut P., Makino J., 2001, MNRAS, 321, 199
Portegies Zwart S. F., McMillan S. L. W., Gieles M., 2010, ARA&A, 48, 431

Downloaded from https://academic.oup.com/mnras/article-abstract/487/4/4615/5509598 by University of Sheffield user on 20 August 2019

Poveda A., Ruiz J., Allen C., 1967, Bol. Obs. Tonantzintla Tacubaya, 4, 86
Poveda A., Allen C., Hernández-Alcántara A., 2005, ApJ, 627, L61
Priyatikanto R., Kouwenhoven M. B. N., Arifyanto M. I., Wulandari H. R. T., Siregar S., 2016, MNRAS, 457, 1339
Rozhavskii F. G., Kuz'mina V. A., Vasilevskii A. E., 1976, Astrophysics, 12, 204
Salpeter E. E., 1955, ApJ, 121, 161
Shukirgaliyev B., Parmentier G., Just A., Berczik P., 2018, ApJ, 863, 171
Silverman B. W., 1986, Density estimation for statistics and data analysis. Monographs on Statistics and Applied Probability Vol. 26. Chapman and Hall, London
Spera M., Capuzzo-Dolcetta R., 2017, Ap&SS, 362, 233
Stone R. C., 1991, AJ, 102, 333
Tetzlaff N., Neuhäuser R., Hohle M. M., 2011, MNRAS, 410, 190
Tutukov A. V., 1978, A&A, 70, 57
van Albada T. S., 1982, MNRAS, 201, 939
Wang J., Townsley L. K., Feigelson E. D., Broos P. S., Getman K. V., Román-Zúñiga C. G., Lada E., 2008, ApJ, 675, 464
Wang L., Kroupa P., Jerabkova T., 2019, MNRAS, 484, 1843
Ward J. L., Kruijssen J. M. D., 2018, MNRAS, 475, 5659
Wareing C. J., Pittard J. M., Wright N. J., Falle S. A. E. G., 2018, MNRAS, 475, 3598
Weidner C., Bonnell I. A., Moeckel N., 2011, MNRAS, 410, 1861
Winter A. J., Clarke C. J., Rosotti G., Ih J., Facchini S., Haworth T. J., 2018, MNRAS, 478, 2700
Wright N. J., Mamajek E. E., 2018, MNRAS, 476, 381
Wright N. J., Bouy H., Drew J. E., Sarro L. M., Bertin E., Cuilland re J.-C., Barrado D., 2016, MNRAS, 460, 2593
Zhong J., Chen L., Kouwenhoven M. B. N., Li L., Shao Z., Hou J., 2019, A&A, 624, A34
Zinnecker H., Yorke H. W., 2007, ARA&A, 45, 481

This paper has been typeset from a TEX/LATEX file prepared by the author.

Downloaded from https://academic.oup.com/mnras/article-abstract/487/4/4615/5509598 by University of Sheffield user on 20 August 2019

Chapter 7

Conclusions

In Arnold et al. (2017) we discuss the formation of pairs of star clusters, which are known as binary clusters. We use N-body simulations of star forming regions to demonstrate that if a region has spatial substructure, and a virial ratio $\gtrsim 0.5$ then they can divide into multiple (most commonly two) distinct regions. We argue that this mechanism may be how binary clusters form. **As such this work offers a potential explanation as to how approximately 10 % of star clusters (see chapter 1) form.**

Further this model makes an observable prediction that can be tested; in this mode of binary cluster formation the clusters that form the binary move apart from one another. This is in contrast to other models of binary cluster formation outlined in chapter 1 which either do not predict any systematic relative velocity between the two clusters, or predict that they will orbit one another and so their relative motions will be tangential. This provides the opportunity for this model to be either observationally supported or ruled out. This will be discussed further in Section 7.1. We also demonstrate that velocity substructure is necessary in order for binary clusters to form by this mechanism. **This further demonstrates the importance of understanding and analysing dynamical data in order to investigate the past (and potential futures) of star forming regions.**

In Arnold & Goodwin (2019) we present a statistical method for quantifying the velocity structure of star forming regions**, the lack of which has been impeding the field as discussed in chapters 1, 4 and 5.** This method works by calculating the velocity difference (Δv) and distance between (Δr) every possible pair of stars in the region. Pairs are then binned by Δr and the average Δv in each bin is calculated. Finally Δr is plotted against these averaged Δvs. Different definitions

of Δv are used to study different aspects of the region's velocity structure. The features of this method are demonstrated, and it is shown to be robust against incomplete data, large uncertainties in stellar velocities, and the presence of binary stars.

This method can be applied without modification to regions of any size, number of stars, age and morphology. As such it offers an avenue by which the velocity structures of very different star forming regions can be quantitatively compared. This opens the way for more systematic studies of how the dynamics of star forming regions evolve, and what they can tell us about the origins of star forming regions and stars themselves. Also, its output is both quantitative and minimally labour-intensive to obtain, as opposed to many other methods that have been attempted to analyse velocity structure which require subjective visual analysis. As such it has the advantage that it can be applied to very large numbers of regions quickly, which is key in this new era of big data astrophysics (as discussed in chapter 1).

In Arnold et al. (2019); submitted we apply the method presented in Arnold & Goodwin (2019) to observations of the Cygnus OB2 star forming region, which are presented in Wright et al. (2010). The region these observations cover has a size of around 10×10 pc, an age of a few Myr, and a velocity dispersion of ~ 20 km s^{-1}. Evidence of velocity structure on scales smaller than 0.5 pc is found. Given this we argue that bound structures exist on scales < 0.5 pc. We also argue that given the age, size, and velocity dispersion of the region it is likely that most of the stars currently observed in it formed 10s of pc from their present positions. We contend that this is why there is no velocity structure at scales larger than 0.5 pc.

Additionally, no evidence of systematic expansion or collapse is found on any scale. From this we argue that these observations are inconsistent with this region being the expanded remnant of a much denser cluster, and therefore are not compatible with the monolithic model of star formation **Therefore this paper provides further evidence for the ongoing debate about how star forming regions originate, as well as acting as a case study in the analysis of the velocity structure of star forming regions using the VSAT method presented in chapter 4.**

In Schoettler et al. (2019) *N*-body simulations of star forming regions are performed. Stars that become unbound from their regions over the course of the simulation are recorded and their properties assessed. No high mass runaway stars are observed, although some lower mass walk-away stars are. This work was conducted with the assistance of code adapted from that used in

Arnold et al. (2017) to study the formation and properties of binary clusters. **The findings of this paper support ongoing arguments (discussed in section 1) that apparently isolated high mass stars are in fact the most massive members of small, low-mass clusters as opposed to being truly isolated having been ejected at high velocities from more massive star forming regions.**

7.1 Further work

As discussed, if binary clusters form via the division of single star forming regions as predicted in Arnold et al. (2017) then we expect the two clusters that form a binary system to be moving away from each other. A natural extension to this work is to test this prediction by studying the velocity structures of observed binary clusters. **If the relative velocities of clusters that form a binary are found to be systematically away from one another this would provide evidence in support of this model of binary cluster formation.**

Another avenue of future work lies in applying the method presented in Arnold & Goodwin (2019) to investigate and interpret the velocity structures of other star forming regions. **By taking advantage of this method's properties that make it quick to apply, particularly well suited to the quantitative comparison of very different regions, and the enormous data reservoirs offered by Gaia in the future a systematic study of a large number of star forming regions using this method seems natural.** Pursuing this may help in advancing our understanding of the formation and evolution of star forming regions.

Bibliography

Aarseth, S. J. 2003, Gravitational N-Body Simulations (Cambridge University Press), 430

Adamo, A. & Bastian, N. 2018, Astrophysics and Space Science Library, Vol. 424, The Lifecycle of Clusters in Galaxies (Springer), 91

Adams, F. C., Hollenbach, D., Laughlin, G., & Gorti, U. 2004, ApJ, 611, 360

Alfaro, E. J. & Román-Zúñiga, C. G. 2018, MNRAS, 478, L110

Allen, G., Andreoni, I., Bachelet, E., et al. 2019, Deep Learning for Multi-Messenger Astrophysics: A Gateway for Discovery in the Big Data Era

Allison, R. J. 2010, PhD thesis, University of Sheffield, Hicks Building, Hounsfield Rd, Sheffield, UK, S3 7RH

Allison, R. J., Goodwin, S. P., Parker, R. J., et al. 2009b, ApJ, 700, L99

Allison, R. J., Goodwin, S. P., Parker, R. J., Portegies Zwart, S. F., & de Grijs, R. 2010, MNRAS, 407, 1098

Allison, R. J., Goodwin, S. P., Parker, R. J., et al. 2009a, MNRAS, 395, 1449

André, P. 2017, Comptes Rendus Geoscience, 349, 187

André, P., Basu, S., & Inutsuka, S. 2009, The formation and evolution of prestellar cores (Cambridge University Press), 254

André, P., Belloche, A., Motte, F., & Peretto, N. 2007, A&A, 472, 519

Andre, P., Ward-Thompson, D., & Barsony, M. 2000, in Protostars and Planets IV, ed. V. Mannings, A. P. Boss, & S. S. Russell, 59

Arnold, B. & Goodwin, S. P. 2019, MNRAS, 483, 3894

Arnold, B., Goodwin, S. P., Griffiths, D. W., & Parker, R. J. 2017, MNRAS, 471, 2498

Arzoumanian, D., André, P., Didelon, P., et al. 2011, A&A, 529, L6

Ballesteros-Paredes, J., Klessen, R. S., Mac Low, M. M., & Vazquez-Semadeni, E. 2007, in Protostars and Planets V, ed. B. Reipurth, D. Jewitt, & K. Keil, 63

Bally, J., Langer, W. D., Stark, A. A., & Wilson, R. W. 1987, ApJ, 312, L45

Barnes, J. & Hut, P. 1986, Nature, 324, 446

Barnes, J. E. & Hernquist, L. 1996, ApJ, 471, 115

Baron, D. 2019, Machine Learning in Astronomy: a practical overview

Bastian, N., Covey, K. R., & Meyer, M. R. 2010, ARA&A, 48, 339

Bastian, N., Gieles, M., Goodwin, S. P., et al. 2008, MNRAS, 389, 223

Bastian, N. & Lardo, C. 2018, Annual Review of Astronomy and Astrophysics, 56, 83136

Bastian, N., Saglia, R. P., Goudfrooij, P., et al. 2006, A&A, 448, 881

Baumgardt, H. & Kroupa, P. 2007, MNRAS, 380, 1589

Bec, J. & Khanin, K. 2007, PhysRep, 447, 1

Berger, M. J. & Jameson, A. 1985, AIAA, 23, 561

Bhatia, R. K. 1990, PASJ, 42, 757

Bhatia, R. K. & Hatzidimitriou, D. 1988, MNRAS, 230, 215

Bhatia, R. K., Read, M. A.and Hatzidimitriou, D., & Tritton, S. 1991, A&AS, 87, 335

Bica, E., Claria, J. J., Dottori, H., Santos, Jr., J. F. C., & Piatti, A. E. 1996, ApJS, 102, 57

Binney, J. & Tremaine, S. 1987, Galactic dynamics (Princeton University Press)

Blaauw, A. 1961, Bulletin of the Astronomical Institutes of the Netherlands, 15, 265

Blanco-Cuaresma, S., Accomazzi, A., Kurtz, M. J., et al. 2019, Fundamentals of effective cloud management for the new NASA Astrophysics Data System

Blitz, L. 1993, in Protostars and Planets III, ed. E. H. Levy & J. I. Lunine, 125

Bonnell, I. A., Bate, M. R., Clarke, C. J., & Pringle, J. E. 2001, MNRAS, 323, 785

Bonnell, I. A., Smith, R. J., Clark, P. C., & Bate, M. R. 2011, MNRAS, 410, 2339

Brand, J. & Wouterloot, J. G. A. 1995, A&A, 303, 851

Brescia, M., Cavuoti, S., Esposito, F., et al. 2016, arXiv e-prints, arXiv:1603.00720

Bressert, E., Bastian, N., Gutermuth, R., et al. 2010, MNRAS, 409, L54

Brinkmann, N., Banerjee, S., Motwani, B., & Kroupa, P. 2017, A&A, 600, A49

Bromm, V., Coppi, P. S., & Larson, R. B. 2002, ApJ, 564, 23

Buckner, A. S. M., Khorrami, Z., Khalaj, P., et al. 2019, A&A, 622, A184

Buhlmann, P. & van de Geer, S. 2018, Statistics and Probability Letters, 136, 37 , the role of Statistics in the era of big data

Burgers, M. J. 1939, Verhand.Kon. Neder. Akad. Wetenschappen, Afd. Natuurkunde, Eerste Sectie, 17, 1

Burkert, A. & Hartmann, L. 2013, ApJ, 773, 48

Busquet, G., Girart, J. M., Estalella, R., et al. 2019, A&A, 623, L8

Camps-Fariña, A., Beckman, J. E., Font, J., et al. 2016, MNRAS, 461, L87

Cantat-Gaudin, T., Mapelli, M., Balaguer-Núñez, L., et al. 2019, A&A, 621, A115

Cartwright, A. & Whitworth, A. P. 2004, MNRAS, 348, 589

CERN Science Collaboration, F. 2018, Key Facts and Figures- CERN Data Centre

Chabrier, G. 2003, PASP, 115, 763

Chandar, R., Fall, S. M., Whitmore, B. C., & Mulia, A. J. 2017, ApJ, 849, 128

Chen, H., Myers, P. C., Ladd, E. F., & Wood, D. O. S. 1995, ApJ, 445, 377

Chira, R. A., Kainulainen, J., Ibáñez-Mejía, J. C., Henning, Th., & Mac Low, M.-M. 2018, A&A, 610, A62

Collier, S. & Peterson, B. M. 2001, ApJ, 555, 775

Colombo, D., Hughes, A., Schinnerer, E., et al. 2014, ApJ, 784, 3

Connelley, M. S., Reipurth, B., & Tokunaga, A. T. 2008, AJ, 135, 2526

Crutcher, R. M. 1999, ApJ, 520, 706

Da Rio, N., Tan, J. C., Covey, K. R., et al. 2017, ApJ, 845, 105

Dale, J. E., Ercolano, B., & Bonnell, I. A. 2012, MNRAS, 424, 377

Dame, T. M., Hartmann, D., & Thaddeus, P. 2001, ApJ, 547, 792

de Grijs, R., Gilmore, G. F., Johnson, R. A., & Mackey, A. D. 2002, MNRAS, 331, 245

De La Fuente Marcos, R. & de La Fuente Marcos, C. 2009, A&A, 500, L13

De Oliveira, M. R., Dottori, H., & Bica, E. 1998, MNRAS, 295, 921

de Wit, W. J., Testi, L., Palla, F., & Zinnecker, H. 2005, A&A, 437, 247

de Zeeuw, P. T., Brown, A. G. A., de Bruijne, J. H. J., et al. 1997, in ESA Special Publication, Vol. 402, Hipparcos - Venice '97, ed. R. M. Bonnet, E. Høg, P. L. Bernacca, L. Emiliani, A. Blaauw, C. Turon, J. Kovalevsky, L. Lindegren, H. Hassan, M. Bouffard, B. Strim, D. Heger, M. A. C. Perryman, & L. Woltjer, 495–500

Dehnen, W. 1998, AJ, 115, 2384

Dehnen, W. & Read, J. I. 2011, EPJ, 126, 55

Dib, S. 2014, MNRAS, 444, 1957

Dieball, A. & Grebel, E. K. 1998, A&A, 339, 773

Dieball, A., Grebel, E. K., & Theis, C. 2000, A&A, 358, 144

Domínguez, R., Fellhauer, M., Blaña, M., Farias, J. P., & Dabringhausen, J. 2017, MNRAS, 472, 465

Duchene, G. & Kraus, A. 2013, ARA&A, 51, 269

Duchêne, G., Simon, T., Eislöffel, J., & Bouvier, J. 2001, A&A, 379, 147

Efremov, Y. N. & Elmegreen, B. G. 1998, MNRAS, 299, 588

Eggleton, P. P. & Tokovinin, A. A. 2008, MNRAS, 389, 869

Elmegreen, B. G. 2000, ApJ, 530, 277

Elmegreen, B. G. & Scalo, J. 2004, ARAA, 42, 211

Emmanoulopoulos, D., McHardy, I. M., & Uttley, P. 2010, MNRAS, 404, 931

Engargiola, G., Plambeck, R. L., Rosolowsky, E., & Blitz, L. 2003, ApJS, 149, 343

Enoch, M. L., Evans, Neal J., I., Sargent, A. I., & Glenn, J. 2009, ApJ, 692, 973

Evans, Neal J., I. 1999, ARAA, 37, 311

Evans, Neal J., I., Dunham, M. M., Jørgensen, J. K., et al. 2009, ApJS, 181, 321

Fatuzzo, M. & Adams, F. C. 2008, ApJ, 675, 1361

Fűrész, G., Hartmann, L. W., Megeath, S. T., Szentgyorgyi, A. H., & Hamden, E. T. 2008, ApJ, 676, 1109

Fűrész, G., Hartmann, L. W., Szentgyorgyi, A. H., et al. 2006, ApJ, 648, 1090

Fischer, P., Pryor, C., Murray, S., Mateo, M., & Richtler, T. 1998, AJ, 115, 592

Franciosini, E., Sacco, G. G., Jeffries, R. D., et al. 2018, A&A, 616, L12

Fujimoto, M. & Kumai, Y. 1997, AJ, 113, 249

Fukui, Y. & Kawamura, A. 2010, ARAA, 48, 547

Fukui, Y., Kawamura, A., Minamidani, T., et al. 2008, ApJS, 178, 56

Galeano, P. & Peña, D. 2019, TEST, 28, 289

Galli, P. A. B., Bertout, C., Teixeira, R., & Ducourant, C. 2013, A&A, 558, A77

Garofalo, M., Botta, A., & Ventre, G. 2017, in IAU Symposium, Vol. 325, Astroinformatics, ed. M. Brescia, S. G. Djorgovski, E. D. Feigelson, G. Longo, & S. Cavuoti, 345–348

Gavagnin, E., Bleuler, A., Rosdahl, J., & Teyssier, R. 2017, MNRAS, 472, 4155

Gennaro, M., Brandner, W., Stolte, A., & Henning, T. 2011, MNRAS, 412, 2469

Gieles, M. & Portegies Zwart, S. F. 2011, MNRAS, 410, L6

Gingold, R. A. & Monaghan, J. J. 1977, MNRAS, 181, 375

Gómez, G. C. & Vázquez-Semadeni, E. 2014, ApJ, 791, 124

González-Lópezlira, R. A., Pflamm-Altenburg, J., & Kroupa, P. 2012, ApJ, 761, 124

Goodwin, S. P. 2009, APSS, 324, 259

Goodwin, S. P. & Bastian, N. 2006, MNRAS, 373, 752

Goodwin, S. P. & Whitworth, A. P. 2004, A&A, 413, 929

Gouliermis, D. A. 2018, PASP, 130, 072001

Gratton, R. G., Carretta, E., & Bragaglia, A. 2012, The Astronomy and Astrophysics Review, 20

Greene, T. P., Wilking, B. A., Andre, P., Young, E. T., & Lada, C. J. 1994, ApJ, 434, 614

Griffiths, D. 2018, PhD thesis, University of Sheffield, Hicks Building, Hounsfield Rd, Sheffield, UK, S3 7RH

Grudić, M. Y., Hopkins, P. F., Faucher-Giguère, C.-A., et al. 2018, MNRAS, 475, 3511

Gutermuth, R. A., Pipher, J. L., Megeath, S. T., et al. 2011, ApJ, 739, 84

Gvaramadze, V. V., Gualandris, A., & Portegies Zwart, S. 2009, MNRAS, 396, 570

Gvaramadze, V. V., Kniazev, A. Y., Chen, A.-N., & Schnurr, O. 2012, MNRAS, 430, L20

Hacar, A. & Tafalla, M. 2011, A&A, 533, A34

Hansen, C. E., Klein, R. I., McKee, C. F., & Fisher, R. T. 2012, ApJ, 747, 22

Hartmann, L. 2001, AJ, 121, 1030

Hartmann, L. 2002, ApJ, 578, 914

Hartmann, L. 2003, ApJ, 585, 398

Hatzidimitriou, D. & Bhatia, R. K. 1990, A&A, 230, 11

Hennebelle, P. & Falgarone, E. 2012, A&AR, 20, 55

Hénon, M. H. 1971, Ap&SS, 14, 151

Heyer, M. & Dame, T. M. 2015, ARA&A, 53, 583

Heyer, M. H. & Brunt, C. M. 2004, ApJ, 615, L45

Heyer, M. H., Carpenter, J. M., & Snell, R. L. 2001, ApJ, 551, 852

Hilker, M., Richtler, T., & Stein, D. 1995, A&A, 299, L37

Hillenbrand, L. A. 1997, AJ, 113, 1733

Hills, J. G. 1980, ApJ, 235, 986

Hong, S., Jeong, D., Hwang, H. S., et al. 2019, Constraining Cosmology with Big Data Statistics of Cosmological Graphs

Hopkins, A. M. & Beacom, J. F. 2006, ApJ, 651, 142

Hu, J. & Zhang, Y. 2017, Scientometrics, 112, 91

Hubber, D. & Rosotti, G. 2016, GANDALF: Graphical Astrophysics code for N-body Dynamics And Lagrangian Fluids, Astrophysics Source Code Library

Hubber, D. A., Allison, R. J., Smith, R., & Goodwin, S. P. 2013, MNRAS, 430, 1599

Hubber, D. A., Batty, C. P., McLeod, A., & Whitworth, A. P. 2011, A&A, 529, A27

Hut, P. 1993, ApJ, 403, 256

Jeans, J. H. 1902, Philosophical Transactions of the Royal Society of London Series A, 199, 1

Jeffries, R. D. 2012, in EAS Publications Series, Vol. 57, EAS Publications Series, ed. C. Reylé, C. Charbonnel, & M. Schultheis, 45–89

Jeffries, R. D., Jackson, R. J., Cottaar, M., et al. 2014, A&A, 563, A94

Kennicutt, R. C. & Evans, N. J. 2012, ARAA, 50, 531

Kim, C.-G., Kim, W.-T., & Ostriker, E. C. 2011, ApJ, 743, 25

King, R. R., Goodwin, S. P., Parker, R. J., & Patience, J. 2012b, MNRAS, 427, 2636

King, R. R., Parker, R. J., Patience, J., & Goodwin, S. P. 2012a, MNRAS, 421, 2025

Kirk, H. & Myers, P. C. 2011, ApJ, 727, 64

Klessen, R. S., Burkert, A., & Bate, M. R. 1998, ApJL, 501, L205

Kolmogorov, A. 1941, Akademiia Nauk SSSR Doklady, 30, 301

Kontizas, E., Kontizas, M., & Michalitsianos, A. 1993, A&A, 267, 59

Kounkel, M., Covey, K., Suárez, G., et al. 2018, AJ, 156, 84

Kouwenhoven, M. B. N., Brown, A. G. A., Portegies Zwart, S. F., & Kaper, L. 2007, A&A, 474, 77

Kremer, J., Stensbo-Smidt, K., Gieseke, F., Pedersen, K. S., & Igel, C. 2017, IEEE Intelligent Systems, 32, 1622

Kroupa, P. 2001, MNRAS, 322, 231

Kroupa, P. & Petr-Gotzens, M. G. 2011, A&A, 529, A92

Kroupa, P., Weidner, C., Pflamm-Altenburg, J., et al. 2013, The Stellar and Sub-Stellar Initial Mass Function of Simple and Composite Populations, Vol. 5 (UAPress), 115

Kruijssen, J. M. D. 2014, Classical and Quantum Gravity, 31, 244006

Kruijssen, J. M. D., Maschberger, T., Moeckel, N., et al. 2012, MNRAS, 419, 841

Krumholz, M. R. & Matzner, C. D. 2009, ApJ, 703, 1352

Krumholz, M. R. & Tan, J. C. 2007, ApJ, 654, 304

Lada, C. J. & Lada, E. A. 2003, ARA&A, 41, 57

Lada, C. J., Lombardi, M., & Alves, J. F. 2010, ApJ, 724, 687

Lada, C. J. & Wilking, B. A. 1984, ApJ, 287, 610

Lada, E. A., Depoy, D. L., Evans, II, N. J., & Gatley, I. 1991, ApJ, 371, 171

Lamers, H. J. G. L. M., Gieles, M., Bastian, N., et al. 2005, A&A, 441, 117

Landoni, M. 2019, Astronomical Society of the Pacific Conference Series, Vol. 523, Application of Google Cloud Platform in Astrophysics (ASPCS), 373

Larson, R. B. 1969, MNRAS, 145, 271

Larson, R. B. 1981, MNRAS, 194, 809

Larson, R. B. 2003, Reports on Progress in Physics, 66, 1651

Latif, M. A., Omukai, K., Habouzit, M., Schleicher, D. R. G., & Volonteri, M. 2016, ApJ, 823, 40

Lennon, D. J., Evans, C. J., van der Marel, R. P., et al. 2018, A&A, 619, A78

Leon, S., Bergond, G., & Vallenari, A. 1999, A&A, 344, 450

Leroy, A., Bolatto, A., Walter, F., & Blitz, L. 2006, ApJ, 643, 825

Lindegren, L., Hernández, J., Bombrun, A., et al. 2018, A&A, 616, A2

Lochner, M., McEwen, J. D., Peiris, H. V., Lahav, O., & Winter, M. K. 2016, APjS, 225, 31

Lomax, O., Bates, M. L., & Whitworth, A. P. 2018, MNRAS, 480, 371

LSST Science Collaboration, I. 2009, LSST Science Book, Version 2.0

Maio, U., Khochfar, S., Johnson, J. L., & Ciardi, B. 2011, MNRAS, 414, 1145

Maschberger, T. 2013, MNRAS, 429, 1725

Maschberger, T. & Clarke, C. J. 2011, MNRAS, 416, 541

Massey, P., Levine, S. E., Neugent, K. F., et al. 2018, AJ, 156, 265

Matheron, G. 1963, Economic Geology, 58, 1246

McKee, C. F. & Ostriker, E. C. 2007, ARAA, 45, 565

McMillan, S. L. W., Vesperini, E., & Portegies Zwart, S. F. 2007, ApJL, 655, L45

Messa, M., Adamo, A., Calzetti, D., et al. 2018, MNRAS, 477, 1683

Mickaelian, A. M. 2016, Baltic Astronomy, 25, 75

Minniti, D., Rejkuba, M., Funes, J. G., & Kennicutt, Jr., R. C. 2004, ApJ, 612, 215

Mizuno, N., Rubio, M., Mizuno, A., et al. 2001, PASJ, 53, L45

Moeckel, N. & Bate, M. R. 2010, MNRAS, 404, 721

Motte, F., Bontemps, S., & Louvet, F. 2018, ARAA, 56, 41

Mucciarelli, A., Origlia, L., Ferraro, F. R., Bellazzini, M., & Lanzoni, B. 2012, ApJ, 746, L19

Murray, S. D. & Lin, D. N. C. 1996, ApJ, 467, 728

Nicholson, R. B. & Parker, R. J. 2017, MNRAS, 464, 4318

Nicholson, R. B., Parker, R. J., Church, R. P., et al. 2019, MNRAS, 485, 4893

Nutter, D., Kirk, J. M., Stamatellos, D., & Ward-Thompson, D. 2008, Monthly Notices of the Royal Astronomical Society, 384, 755

Offner, S. S. R., Clark, P. C., Hennebelle, P., et al. 2014, in Protostars and Planets VI, ed. H. Beuther, R. S. Klessen, C. P. Dullemond, & T. Henning, 53

Offner, S. S. R., Hansen, C. E., & Krumholz, M. R. 2009, ApJ, 704, L124

Olczak, C., Spurzem, R., & Henning, T. 2011, A&A, 532, A119

Padoan, P., Bally, J., Billawala, Y., Juvela, M., & Nordlund, Å. 1999, ApJ, 525, 318

Padoan, P., Jimenez, R., Juvela, M., & Nordlund, Å. 2004, ApJ, 604, L49

Palla, F. 2005, in IAU Symposium, Vol. 227, Massive Star Birth: A Crossroads of Astrophysics, ed. R. Cesaroni, M. Felli, E. Churchwell, & M. Walmsley, 196–205

Palma, T., Gramajo, L. V., Clariá, J. J., et al. 2016, A&A, 586, A41

Palmeirim, P., André, P., Kirk, J., et al. 2013, A&A, 550, A38

Pang, X., Grebel, E. K., Allison, R. J., et al. 2013, ApJ, 764, 73

Parker, R. J. & Goodwin, S. P. 2007, MNRAS, 380, 1271

Parker, R. J. & Goodwin, S. P. 2012, MNRAS, 424, 272

Parker, R. J., Wright, N. J., Goodwin, S. P., & Meyer, M. R. 2014, MNRAS, 438, 620

Perret, V., Renaud, F., Epinat, B., et al. 2014, A&A, 562, A1

Pfalzner, S. & Kaczmarek, T. 2013, A&A, 555, A135

Pfalzner, S. & Olczak, C. 2007, A&A, 475, 875

Pflamm-Altenburg, J., González-Lópezlira, R. A., & Kroupa, P. 2013, MNRAS, 435, 2604

Pietrzynski, G. & Udalski, A. 2000, Acta Astron., 50, 355

Piskunov, A. E., Just, A., Kharchenko, N. V., et al. 2018, A&A, 614, A22

Plummer, H. C. 1911, MNRAS, 71, 460

Plunkett, A. L., Fernández-López, M., Arce, H. G., et al. 2018, A&A, 615, A9

Portegies Zwart, S. F., McMillan, S. L. W., Hut, P., & Makino, J. 2001, MNRAS, 321, 199

Portegies Zwart, S. F. & Rusli, S. P. 2007, MNRAS, 374, 931

Porter, D. H., Pouquet, A., & Woodward, P. R. 1992, Phys. Rev. Lett., 68, 3156

Porter, D. H., Pouquet, A., & Woodward, P. R. 1994, Physics of Fluids, 6, 2133

Priyatikanto, R., Kouwenhoven, M. B. N., Arifyanto, M. I., Wulandari, H. R. T., & Siregar, S. 2016, MNRAS, 457, 1339

Raghavan, D., McAlister, H. A., Henry, T. J., et al. 2010, ApJS, 190, 1

Raskutti, S., Ostriker, E. C., & Skinner, M. A. 2016, ApJ, 829, 130

Ravanbakhsh, S., Lanusse, F., Mandelbaum, R., Schneider, J., & Poczos, B. 2016, arXiv e-prints, arXiv:1609.05796

Reipurth, B., Clarke, C. J., Boss, A. P., et al. 2014, in Protostars and Planets VI, ed. H. Beuther, R. S. Klessen, C. P. Dullemond, & T. Henning, 267

Reiter, M. & Parker, R. J. 2019, MNRAS, 486, 4354

Rodríguez, M. J., Baume, G., & Feinstein, C. 2019, A&A, 626, A35

Rosolowsky, E. & Blitz, L. 2005, ApJ, 623, 826

Rosolowsky, E., Engargiola, G., Plambeck, R., & Blitz, L. 2001, in American Astronomical Society Meeting Abstracts, Vol. 199, 117.02

Rosolowsky, E. W., Pineda, J. E., Foster, J. B., et al. 2008, ApJS, 175, 509

Rozhavskii, F. G., Kuz'mina, V. A., & Vasilevskii, A. E. 1976, Astrophysics, 12, 204

Ryon, J. E., Bastian, N., Adamo, A., et al. 2015, MNRAS, 452, 525

Salpeter, E. E. 1955, ApJ, 121, 161

Sana, H., de Koter, A., de Mink, S. E., et al. 2013, A&A, 550, A107

Sarbadhicary, S. K., Chomiuk, L., Badenes, C., et al. 2019, ApJ, 872, 191

Scalo, J. & Elmegreen, B. G. 2004, ARAA, 42, 275

Schneider, R., Ferrara, A., Salvaterra, R., Omukai, K., & Bromm, V. 2003, Nature, 422, 869

Schoettler, C., Parker, R. J., Arnold, B., et al. 2019, MNRAS

Seitenzahl, I. R., Ghavamian, P., Laming, J. M., & Vogt, F. P. A. 2019, PRL, 123, 041101

Simon, M., Ghez, A. M., Leinert, C., et al. 1995, ApJ, 443, 625

Simonetti, J. H., Cordes, J. M., & Heeschen, D. S. 1985, ApJ, 296, 46

Soker, N. 2019, Supernovae Ia in 2019 (review): a rising demand for spherical explosions

Solomon, P. M., Rivolo, A. R., Barrett, J., & Yahil, A. 1987, ApJ, 319, 730

Stephens, I. W., Gouliermis, D., Looney, L. W., et al. 2017, ApJ, 834, 94

Stewart, K. R., Bullock, J. S., Barton, E. J., & Wechsler, R. H. 2009, ApJ, 702, 1005

Sugimoto, D. & Makino, J. 1989, PASJ, 41, 1117

Taghizadeh-Popp, M., Kim, J. W., Lemson, G., et al. 2020, SciServer: a Science Platform for Astronomy and Beyond

Tagliaferri, R., Longo, G., Milano, L., & Marengo, M. 2003, Neural Networks, 16, 297

Teixeira, P. S., Lada, C. J., Young, E. T., et al. 2006, ApJL, 636, L45

Tobin, J. J., Hartmann, L., Fűrész, G., Hsu, W.-H., & Mateo, M. 2015, AJ, 149, 119

Tutukov, A. V. 1978, A&A, 70, 57

Vallenari, A., Bettoni, D., & Chiosi, C. 1998, A&A, 331, 506

Vázquez-Semadeni, E., Ballesteros-Paredes, J., & Rodríguez, L. F. 1997, ApJ, 474, 292

Vázquez-Semadeni, E., González-Samaniego, A., & Colín, P. 2017, MNRAS, 467, 1313

Ward-Thompson, D., Motte, F., & Andre, P. 1999, MNRAS, 305, 143

Wright, N. J., Bouy, H., Drew, J. E., et al. 2016, MNRAS, 460, 2593

Wright, N. J., Drake, J. J., Drew, J. E., & Vink, J. S. 2010, ApJ, 713, 871

Wright, N. J. & Mamajek, E. E. 2018, MNRAS, 476, 381

Wright, N. J., Parker, R. J., Goodwin, S. P., & Drake, J. J. 2014, MNRAS, 438, 639

Xing, L. F. 2010, ApJ, 723, 1542

Yoshida, N., Omukai, K., & Hernquist, L. 2008, Science, 321, 669

Yue, Y. & Li, D. 2019, Big Scientific Data Management. BigSDM 2018. Lecture Notes in Computer Science, 11473, 6

Zamora-Avilés, M., Ballesteros-Paredes, J., & Hartmann, L. W. 2017, MNRAS, 472, 647

Zinnecker, H. & Yorke, H. W. 2007, ARA&A, 45, 481

Zuckerman, B. & Evans, II, N. J. 1974, ApJ, 192, L149